University of Trento
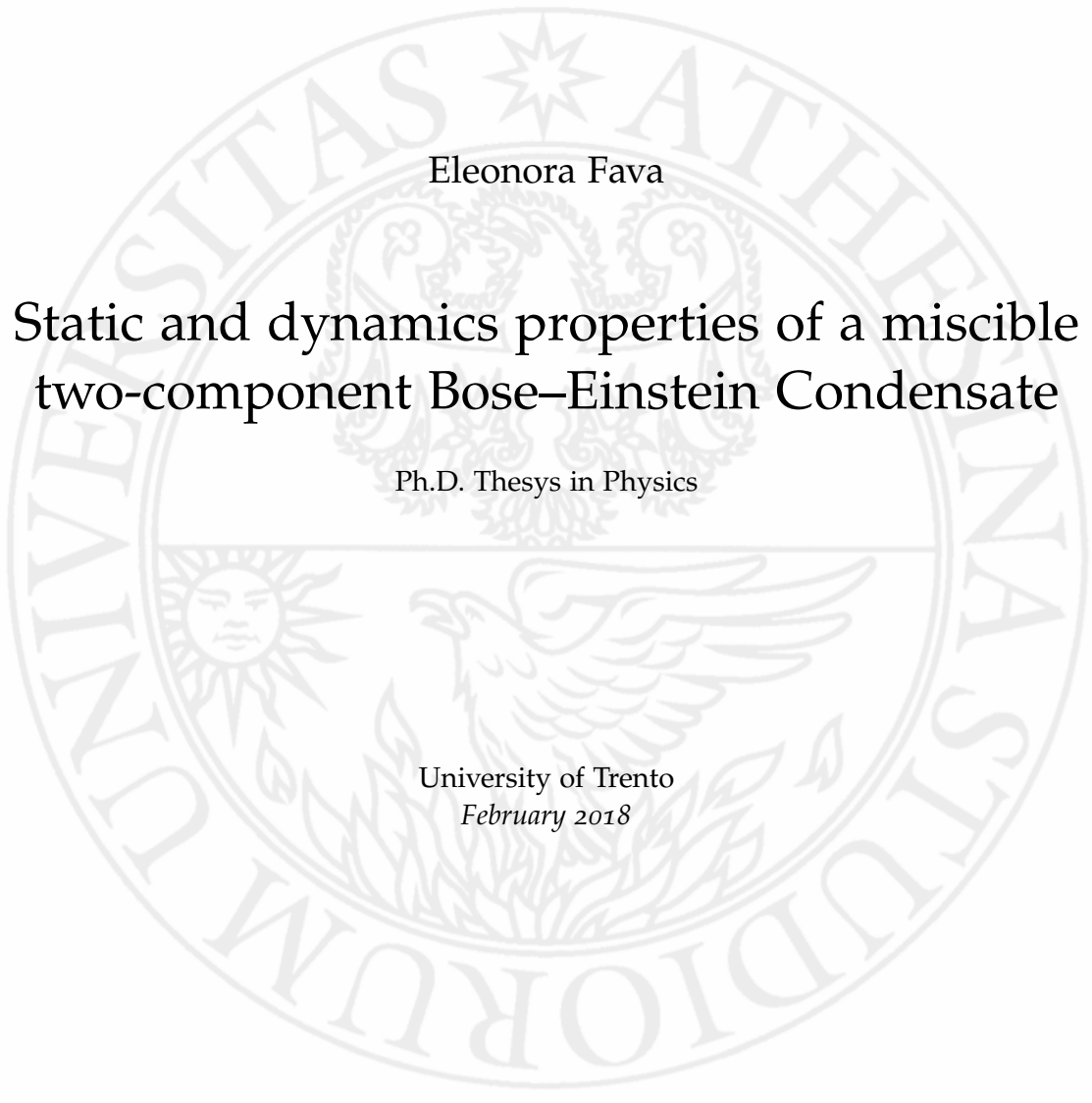## Department of Physics

Eleonora Fava

for the degree of

Doctor of Philosophy – Dottore di Ricerca

Static and dynamics properties of a miscible two-component Bose–Einstein Condensate

Supervisor: Gabriele Ferrari

Co-Supervisor: Giacomo Lamporesi

February 2018

Eleonora Fava

Static and dynamics properties of a miscible two-component Bose–Einstein Condensate

Ph.D. Thesys in Physics

University of Trento
February 2018

CONTENTS

"Si sta
come di primavera
sul banco ottico
gli AOM"

— G.C.

INTRODUCTION

Since the first realization of Bose–Einstein condensation [1, 2], the ultra-cold gases established as a powerful platform of research both theoretically and experimentally. One of the main reasons which makes BECs a successful topic of research is their flexibility for creating systems whose Hamiltonian can be engineered almost at will. Thus, by preparing the proper experiment, it is possible to simulate and investigate a large variety of many-body configurations related to several research fields in physics, from condensed matter to high-energy physics to cosmology. [3]. For instance, BECs can be used to simulate spin-orbit coupling (SOC) in solid state matter physics [4], vorticity in quantum and classic fluid-dynamics [5], Hawking's radiation [6], the universe expansion [7], Mott-insulators [8] or high-T_c superconductivity [9].

In my thesis work, I will mainly focus on the study of spin properties in binary Bose-Bose mixtures trapped in harmonic optical potentials. This topic is intrinsically related to spintronic, which is a rising field of research focused on the influence of electron (and nuclear) spin on the electrical conduction. Spin properties can be exploited in alternative or in addition to charge and orbital degrees of freedom. Spin relaxation and spin transport in metals and semiconductors are of high interest not only for their fundamental implications, but also for their possible application in (spin)electronic technology. Nowadays, some devices based on the use of spin properties are already employed in industry, like giant-magnetoresistive (GMR) layers structures [10]. These devices are used as memory-storage cells or read head and consist of alternate layers of ferromagnetic and non-magnetic metals, which are able to change their resistance depending on the magnetization on the magnetic layers. However, they represent only a first step in the development of spintronics, since our understanding of many-body spin dynamics is still incomplete. In fact, the study of spin transport in solid-state physics is complex since in these systems spin is not a conserved quantity and different relaxation mechanisms can occur.

In this framework, the investigation of systems where spin is a conserved quantity can represent a starting point to deepen in the field. For example, degenerate binary mixtures can be investigated to study the role of interactions between different spin particles that, at finite temperature, can lead to a relaxation of the spin current via spin drag [11], as well as the condition to spin superfluidity [12].

Another relevant field of research, which is very popular nowadays, concerns new phases of matter. Among all the fascinating new kinds of systems which have been predicted in the last decades, supersolids are particularly relevant in the field of Bose–Einstein condensation. This new phase of matter, was predicted for the first time by Thouless and independently by Andreev and Lifshitz in 1969 [13, 14]. A supersolid consists in a material where the properties of superfluidity (intended as off-diagonal long-range order) and solidity (intended as density long-range order) can simultaneously exist [15].

The link between supersolidity and BEC lies on the possibility to engineer a quantum system, for instance by means of the spin-orbit coupling, in which diagonal and off-diagonal long range order coexist in the so-called stripe phase [16] and the experimental observation of the supersolid phase [17, 18] will permit to address several fundamental questions.

Technically, the realization of SOC-BEC in the stripe phase requires the manipulation of degenerate binary mixtures under precise control of environmental magnetic fields in conditions that are difficult to meet in most experimental apparatus. More specifically, the need to manipulate quantum binary mixtures requires a deep knowledge of the system properties, even in absence of coherent coupling ($\Omega = 0$) between the two states, while to control the magnetic field with high precision, shielding tools are required. Both these topics are related to my research work, which aims to lay the foundation for experimental studies in resonantly-coupled spinor BECs, such as spin-orbit coupled BECs.

At this initial stage, the simplest collective oscillation, *i.e.*, the spin-dipole (SD) oscillation and the static SD polarizability are studied to test the miscibility properties of the system and its response to external perturbation of the trapping potentials, both in the static and in the dynamic case in order to characterize the response of the system at $\Omega = 0$. In addition to its link with the realization of more complex binary systems, my research reveals interesting features concerning the spin properties of the $|F = 1, m_F = \pm 1\rangle$ binary mixture of sodium atoms. In fact, since this system is miscible and fully spin symmetric, it is possible to investigate its spin properties when a small displacement of the trap minima is applied, *i.e.*, it is possible to investigate the linear regime, where interactions among atoms play a crucial role. Differently from other mixtures already investigated [19, 20, 21, 22, 23, 24, 25, 26, 27, 28, 29, 30, 31, 32, 33, 34, 35, 36, 37], the spin-dipole oscillation frequency ω_{SD} and the static SD polarizability $\mathcal{P}$ are directly studied. While the SD oscillation shows interesting relations with the giant dipole resonance of nuclear physics [38], the investigation of this system at finite temperature permitted to prove the superfluid nature of spin currents in the case of a collisional regime. In fact, the observation of undamped oscillations at zero temperature is consistent with superfluidity, but is not a proof of it, since undamped oscillations can be the result of mean-field interactions (as the propagation of spin-zero-sound in a normal Fermi liquid [39]). The observation of undamped spin oscillations in the collisional regime can be instead regarded as a direct proof of spin superfluidity since, in the presence of collisions, the spin current of the normal component is not conserved due to spin drag and only in the superfluid phase one can observe the propagation of spin sound.

For what concerns the control of magnetic fields, I developed a specific design of a four-layer cylindrical magnetic shield which should guarantee a homogeneity and stability of the environmental magnetic field experienced by our atomic sample, so that a coherent coupling between different internal states on the second timescale can be applied. To define the best shield design its efficiency was numerically simulated with a FEM software. The magnetic shield was recently delivered and it will be installed on the experiment soon.

Thanks to the implementation of magnetic shielding and the use of a new experimental sequence to reach quantum degeneracy, it will be possible to study mixtures in the presence of a coherent coupling between the two states on timescale long compared to those of the many-body dynamics (Fis$\hbar$ project). Such systems show properties having analogies with the formation of stripe phases or with the formation of domain walls (as proposed by [40]), which are related to quark confinement in quantum chromodynamics (QCD) .

In conclusion, my work represents only the starting point of a wider research that will be developed in the next years and that will lead to a deeper understanding of several systems and phenomena related to superfluidity and spinor physics.
The thesis is divided into five chapters, each of them dedicated to a specific topic.

- The first chapter is devoted to the theoretical description of harmonically trapped binary mixtures of Bose-Einstein condensates both at zero and finite temperature. In particular, the conditions to have a miscible mixture are described, as well as the buoyancy phenomenon, which affects most of the binary mixtures studied so far. In this chapter the theoretical estimates of the spin-dipole oscillation frequency ω_{SD} and polarizability $\mathcal{P}$, in the limit of linear regime, are given and the conditions at which these quantities can be experimentally measured are discussed.

- In the second chapter the experimental apparatus used to perform the experiment is described in detail, ranging from the vacuum apparatus to the experimental control system.

- In the third chapter all the experimental techniques used to create the binary mixture are presented. Here, particular attention is given to the sequence that allows to create and study the condensed binary system, both in the limit of low and finite temperature.

- In the fourth chapter I report on the main results concerning the static and dynamic spin properties of our binary mixture of BECs, which are studied both at zero and finite temperature. In particular, in the finite temperature case, two interacting regimes are investigated, namely collisionless and collisional. For both temperature conditions, a direct comparison of experimental data with numerical integrated Gross–Pitaevskii equation (GPE) simulations is shown.

- The fifth chapter is devoted to the design of the magnetic shield. A selection of simulations, performed in order to find the best shield design, are reported in this chapter. Here, our geometric and experimental constraints are illustrated in detail and the expected theoretical performances of the final shielding configuration are discussed.

1 | THEORY

Contents

This chapter is devoted to the theoretical description of quantum-degenerate binary mixtures both at zero and at finite temperature. After a brief reminder on the case of a weakly interacting BEC in a harmonic trap, the coupled Gross–Pitaevskii equations used to describe binary ultracold mixtures at zero temperature are derived. This theoretical approach, which holds at $T = 0$, is then extended to the case of finite temperature using a mean-field description based on the Hartree–Fock approximation.

In addition, the miscibility conditions for a binary BEC mixture are also introduced, showing that the sodium system used for this work is an excellent candidate to study static and dynamic properties in the linear regime that were never previously studied.

1.1 WEAKLY INTERACTING TRAPPED BECS AT ZERO TEMPERATURE

The theoretical description of our system should take both interactions and the confining potential into account. Even if the mean-field theory developed by Bogoliubov in 1947 [41] is able to describe the role of interactions among particles, it is not suitable to describe the role of external potentials. Since most experiments with ultracold atoms are performed in traps (magnetic or optical), it is important to properly describe these non-uniform systems.

The generalization of the Bogoliubov theory to the case of non-uniform and time-dependent configurations can be obtained assuming that, to the lowest approximation, the field operator $\hat{\Psi}$ can be replaced by the classical field $\Psi(\vec{r}, t)$, called the order parameter [42]. This approximation holds at very low temperature and for a large number of particles. In addition, since for dilute

cold gases only binary collisions are relevant at low energy, the interaction among particles can be described by a contact potential

$$V(\vec{r}' - \vec{r}) = g\delta(\vec{r}' - \vec{r}),$$ (1.1)

where the coupling constant g is directly related to the s-wave scattering length a trough the relation

$$g = \frac{4\pi\hbar^2 a}{m},$$ (1.2)

$\hbar$ is the Planck constant and m is the particles mass. These assumptions lead to the Gross–Pitaevskii equation (GPE) [42]

$$i\hbar\frac{\partial}{\partial t}\Psi(\vec{r}, t) = \left(-\frac{\hbar^2\nabla^2}{2m} + V_{ext}(\vec{r}) + g|\Psi(\vec{r}, t)|^2\right)\Psi(\vec{r}, t),$$ (1.3)

where V_{ext} is the external potential used to trap the sample.

For a gas confined in a harmonic trap, the external potential at a given position $\vec{r}$, can be expressed as

$$V_{ext}(\vec{r}) = V_{ext}(x, y, z) = \frac{1}{2}m\omega_x^2 x^2 + \frac{1}{2}m\omega_y^2 y^2 + \frac{1}{2}m\omega_z^2 z^2,$$ (1.4)

where $\omega_{x,y,z}$ are the trapping frequencies. The size of the atomic cloud along each direction i is fixed by the harmonic oscillator length

$$a_{ho_i} = \sqrt{\hbar/m\omega_i}.$$ (1.5)

The characteristic length of the system is thus given by $a_{ho} = \sqrt{\hbar/m\bar{\omega}}$, where $\bar{\omega} = (\omega_x\omega_y\omega_z)^{1/3}$ is the geometrical average of the trapping frequencies. The ground state of Eq.1.3 is obtained, within the formalism of mean field, by writing the wave function as $\Psi(\vec{r}, t) = \phi(\vec{r})e^{-i\mu t/\hbar}$

$$\mu\phi(\vec{r}) = \left(-\frac{\hbar^2\nabla^2}{2m} + V_{ext}(\vec{r}) + g\phi^2(\vec{r})\right)\phi(\vec{r})$$ (1.6)

Thomas–Fermi limit   When the energy contribution due to interactions is large compared to the kinetic energy of the system, the so-called Thomas–Fermi approximation is applicable. In this limit the kinetic energy (also called the quantum-pressure) is neglected and the Gross–Pitaevskii equation (Eq.1.6) reduces to

$$\mu\phi(\vec{r}) = \left(V_{ext}(\vec{r}) + g\phi^2(\vec{r})\right)\phi(\vec{r}),$$ (1.7)

from which the density profile of the trapped BEC can be extracted

$$n(\vec{r}) = \phi^2(\vec{r}) = \frac{\mu - V_{ext}(\vec{r})}{g}.$$ (1.8)

From Eq.1.8 some of the quantities used in the next chapters are obtained, such as the chemical potential and the Thomas–Fermi radii which are

$$\mu = \frac{\hbar\bar{\omega}}{2}\left(15\frac{Na}{a_{ho}}\right)^{2/5}$$ (1.9)

and

$$R_i = \sqrt{\frac{2\mu}{m\omega_i}}, \tag{1.10}$$

respectively. Other important quantities which will be used later in the thesis, are the healing length ξ and the critical temperature T_C. The former can be interpreted as the recovery length of the condensate, *i.e.*, the distance necessary to restore the local equilibrium value of the density n from 0 and is defined as

$$\xi = \sqrt{\frac{1}{8\pi na}}. \tag{1.11}$$

The critical temperature T_C corresponds to the temperature below which the condensation occurs. Since interactions in the estimate of T_C generally give a small correction, the critical temperature is computed using the formula valid for trapped non-interacting systems

$$T_C = \frac{\hbar\bar{\omega}}{k_B}\left(\frac{N}{\zeta(3)}\right)^{1/3}, \tag{1.12}$$

where k_B is the Boltzmann constant and ζ is the Riemann zeta function.

1.2 QUANTUM MIXTURE AT ZERO TEMPERATURE

The advent of optical traps for quantum gases [43] has opened an interesting scientific scenario, both experimentally and theoretically. In fact, the possibility to trap atom independently from their internal state paved the way for the realization of more complex systems that can be engineered with great flexibility. In the last twenty years, several spinor systems, *i.e.*, systems in which atoms occupy each level of the given hyperfine manifold, were realized using both rubidium [44, 45, 46] and sodium [47, 48, 49, 50] atoms in the $F = 1$ ground state. In addition, several theoretical works and reviews are reported in literature [51, 52, 53, 54, 55], also concerning spin-2 systems [56, 57].
Of particular interest for this thesis work are binary mixtures, which are widely investigated due to the large variety of systems that can be created [58, 59, 60, 61, 62, 63, 64, 65, 66]. In fact, it is possible to obtain experimentally binary mixture using different atomic species (like K-Rb[23, 24], Yb-Li [36], Yb-Cs [35], Rb-Cs [30] or Na-K [28]) or using two isotopes of the same atom (like ^{6}Li-^{7}Li in [67, 29, 31] or ^{4}He-^{6}He in [68]). Another class of mixtures which attracts large interest corresponds to mixtures obtained using two internal states of the same atomic species. These states can be two Zeeman levels of the same hyperfine level (like in rubidium [21, 22, 32], in sodium [69, 33] or in potassium [37]) or can belong to two hyperfine states (like for the case of ^{87}Rb in [19, 20, 25, 26, 27, 34]).
All these systems present different features and are suitable to study different phenomena, among which dynamics, instabilities or interaction effects. For example, of particular interest, are the works realized using the

$|2,1\rangle + |1,-1\rangle$ of rubidium [25, 20, 34]. This mixture, being at the miscible-immiscible threshold (see Subs.1.2.1), presents a non-trivial dynamics which can lead to the formation of ring excitations (in absence of Rabi coupling between the two spin components).

Other works related to my research, concern the study of dynamics on both sides of the miscible-immiscible phase transition by means of Feshback resonance in $|2,-1\rangle + |1,1\rangle$ mixture of rubidium atoms.

However, all these works focus on dynamics properties of system which are not fully miscible (see next subsections), while, in my research, dynamic and static spin properties [70] of a completely miscible mixture are investigated. In the following a theoretical description of binary mixture is reported, giving particular attention to the concept of miscibility.

Binary interacting mixtures   In the case of a single component BEC, interactions are well described by a single parameter, *i.e.*, the coupling constant g. In a binary mixture, it is necessary to introduce three parameters to describe all the interactions occurring in the system. Labeling the two condensates as 1 and 2, these parameters are g_{11}, g_{22} and g_{12} which are the two intra-component coupling constants and the inter-component coupling constant, respectively.

The first theoretical description of a binary mixture was presented in 1996 [71] and it is obtained generalizing the GP equation for the two condensates, where each component is described by its own wave function. Proceeding in this way the energy of the mixture can be written as

$$E = \int d\vec{r} \left[\frac{\hbar^2}{2m_1}|\nabla\Psi_1|^2 + \frac{\hbar^2}{2m_2}|\nabla\Psi_2|^2 + V_{1,ext}|\Psi_1|^2 + V_{2,ext}|\Psi_2|^2 \right.$$
$$\left. + \frac{1}{2}g_{11}|\Psi_1|^4 + \frac{1}{2}g_{22}|\Psi_2|^4 + g_{12}|\Psi_1|^2|\Psi_2|^2, \right. \tag{1.13}$$

where Ψ_1, Ψ_2 are the wave functions of the condensates, m_1, m_2 their relative masses and $V_{1,ext}, V_{2,ext}$ are the trapping potentials experienced by each component. The coupling constants $g_{11} = 4\pi\hbar^2 a_{11}/m_1$ and $g_{22} = 4\pi\hbar^2 a_{22}/m_2$ are fixed by the s-wave scattering lengths a_{11}, a_{22} which characterize the interaction between pairs of atoms of the same condensate, while $g_{12} = 2\pi\hbar^2 a_{12}/m_r$ counts for interactions between atoms of different species, being $1/m_r = 1/m_1 + 1/m_2$ the reduced mass. In order to guarantee the stability of the system, g_{11} and g_{22} are assumed to be positive, while g_{12} can be either positive or negative [42].

From the variational principle it is possible to obtain the coupled Gross–Pitaevskii equations which describe the two components of the system

$$i\hbar\frac{\partial}{\partial t}\Psi_1 = \left(-\frac{\hbar^2\nabla^2}{2m_1} + V_{1,ext}(\vec{r}) + g_{11}|\Psi_1|^2 + g_{12}|\Psi_2|^2 \right)\Psi_1 \tag{1.14}$$

$$i\hbar\frac{\partial}{\partial t}\Psi_2 = \left(-\frac{\hbar^2\nabla^2}{2m_2} + V_{2,ext}(\vec{r}) + g_{22}|\Psi_2|^2 + g_{12}|\Psi_1|^2 \right)\Psi_2 \tag{1.15}$$

and from which the ground state of the mixture can be found.

Uniform system   For simplicity we start by considering the equilibrium regime in a homogeneous system. In this framework the system can be either in a uniform

or in a phase separated configuration. In the uniform case the interaction energy takes the form

$$E_{unif} = \frac{g_{11}}{2}\frac{N_1^2}{V} + \frac{g_{22}}{2}\frac{N_2^2}{V} + g_{12}\frac{N_1 N_2}{V}, \tag{1.16}$$

while in the separated configuration it takes the form

$$E_{sep} = \frac{g_{11}}{2}\frac{N_1^2}{V_1} + \frac{g_{22}}{2}\frac{N_2^2}{V_2}, \tag{1.17}$$

where V_1 and V_2 are the volumes occupied by the two separated components and $V = V_1 + V_2$ is the total volume.

The mechanical equilibrium between the two separated phases is given by the condition

$$\frac{\partial E_{sep}}{\partial V_1} = \frac{\partial E_{sep}}{\partial V_2}, \tag{1.18}$$

which implies the relationship

$$g_{11}\left(\frac{N_1}{V_1}\right)^2 = g_{22}\left(\frac{N_2}{V_2}\right)^2. \tag{1.19}$$

By substituting Eq.1.19 in Eq.1.17, one finds

$$E_{sep} = \frac{g_{11}}{2}\frac{N_1^2}{V} + \frac{g_{22}}{2}\frac{N_2^2}{V} + \sqrt{g_{11}g_{22}}\frac{N_1 N_2}{V}. \tag{1.20}$$

The condition to avoid phase separation is $E_{sep} > E_{unif}$ which, comparing Eq.1.20 and Eq.1.16, leads to the relation $g_{12} < \sqrt{g_{11}g_{22}}$. This condition can be generalized, in the case of attractive interactions between the two spin components, by considering that the uniform phase is stable against energetic instabilities[1] if

$$|g_{12}| < \sqrt{g_{11}g_{22}}. \tag{1.21}$$

When this condition is satisfied the system is said to be miscible, while when the system is in the phase separated configuration, it is said to be immiscible. In Fig.1.1 an example of both miscible and immiscible systems are reported for the case of atomic sodium.. The miscible system correspond to the mixture $|F = 1, m_F = \pm 1\rangle$ (right image of Fig.1.1), while the immiscibility is visible in the spinor configuration, where all three levels of sodium ground state $F = 1$ are present (left image of Fig.1.1). In the spinor, the phase separation is due to the presence of $|F = 1, m_F = 0\rangle$, which is immiscible with both $|F = 1, m_F = 1\rangle$ and $|F = 1, m_F = -1\rangle$. *Trapped system*

In the trapped configuration the equilibrium density profiles can be obtained in the Thomas–Fermi limit (described in Sec.1.1) where, under the miscibility condition, one finds that Eqs.1.14,1.15 become

$$\mu_1 - V_{1,ext}(\vec{r}) - g_{11}n_1(\vec{r}) - g_{12}n_2(\vec{r}) = 0 \tag{1.22}$$

$$\mu_2 - V_{2,ext}(\vec{r}) - g_{22}n_2(\vec{r}) - g_{12}n_1(\vec{r}) = 0. \tag{1.23}$$

---

1 Actually, if $|g_{12}| > \sqrt{g_{11}g_{22}}$, quantum fluctuations prevents the collapse of the system, leading to the creation of quantum droplets [72, 73, 37].
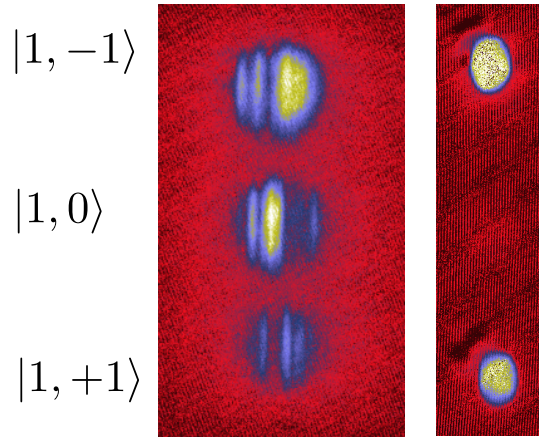
$|1, -1\rangle$

$|1, 0\rangle$

$|1, +1\rangle$

Figure 1.1: Comparison between a phase separated spinor (left) and miscible mixture(right). The phase separated system is composed of the three Zeeman sublevels of the ground state of sodium, while the miscible system is composed of the two zeeman sublevels $|F = 1, m_F = 1\rangle$ and $|F = 1, m_F = -1\rangle$. The phase separation in the spinor configuration is due to the presence of $|F = 1, m_F = 0\rangle$, which is immiscible either with $|F = 1, m_F = 1\rangle$ and $|F = 1, m_F = -1\rangle$. Both the pictures were taken after TOF in a Stern–Gerlach configuration in order to spatially separate the different spin components.

These equations hold, provided $n_1(\vec{r})$ and $n_2(\vec{r})$ are finite or set to zero and, in the region of non-vanishing densities, they can be rewritten as

$$n_1(\vec{r}) = \frac{1}{g_{11}(1 - \Delta)} \left(\mu_1 - \frac{g_{12}}{g_{11}} \mu_2 - V_{1,eff}(\vec{r}) \right) \tag{1.24}$$

$$n_2(\vec{r}) = \frac{1}{g_{22}(1 - \Delta)} \left(\mu_2 - \frac{g_{12}}{g_{22}} \mu_1 - V_{2,eff}(\vec{r}) \right) \tag{1.25}$$

where $\Delta = g_{12}^2 / g_{11} g_{22} < 1$ and

$$V_{1,eff}(\vec{r}) = V_{1,ext}(\vec{r}) - \frac{g_{12}}{g_{22}} V_{2,ext}(\vec{r}) \tag{1.26}$$

$$V_{2,eff}(\vec{r}) = V_{2,ext}(\vec{r}) - \frac{g_{12}}{g_{11}} V_{1,ext}(\vec{r}) \tag{1.27}$$

are the effective potentials felt by the two components.

A relevant feature emerging from the equations reported above is that the Thomas–Fermi radii of the two components are in general not equal. This feature is related to an interesting phenomenon known as buoyancy which is the topic of the next section. It is important to note that, when dealing with quantum mixtures, the TF approximation can be considered valid when the TF radii are much larger than the spin healing length

$$\xi_s = \hbar / \sqrt{2mn(\sqrt{g_{11} g_{22}} - g_{12})}. \tag{1.28}$$

1.2.1 The buoyancy phenomenon

A fundamental issue, when dealing with quantum binary mixtures, is the miscibility of the system. In fact, as mentioned in the previous section, the mixture can assume a miscible configuration as well as a phase separated

one where the two components tend to stay apart one from the other, occupying different volumes, depending on the interaction properties of the system.

As matter of fact, even when the system is in the miscible configuration, the density distributions of the two components can rearrange themselves in a non-obvious way. This phenomenon is related to the intra-component coupling constants and appears only when g_{11} and g_{22} are not equal and when atoms are confined in a non-uniform potential.

Let us suppose, for example, that $g_{22} > g_{11}$ and $N_1 = N_2$ and let us consider the peak density distributions of the single component in the Thomas–Fermi approximation

$$n_i(0) = \frac{\mu_i}{g_{ii}}. \tag{1.29}$$

Since $\mu \propto g^{2/5}$ it is simple to verify that

$$\frac{n_2(0)}{n_1(0)} \propto \left(\frac{g_{11}}{g_{22}}\right)^{3/5} < 1, \tag{1.30}$$

thus $n_2(0) < n_1(0)$. This inequality underlines the fact that, even without taking the inter-component interactions into account, the two components have different density distributions and Thomas–Fermi radii.

In addition, the interaction term between the two components proportional to $g_{12}n_1n_2$ is not negligible and its effect is to increase the internal energy of the system. Thus, to minimize the total energy, the energetic contribution given by the interaction between atoms of different components should be reduced.

In order to weaken this interaction energy the system has the only possibility to change the two density distributions in order to reduce the overlap area between the two components. Thus, using the same example as before, the denser component 1 will tend to shrink even more increasing its peak density and reducing its TF radius, while component 2 will tend to decrease its peak density. In addition, the inverted-parabola profile will be modified in order to further reduce the density in the overlap area and, consequently, increase n outside the spatial region occupied by component 1. A sketch of this rearrangement mechanism is given in Fig.4.2. This phenomenon goes by the name of buoyancy since the overall effect is that one component "floats" on the other, being the two density distributions related one to the other. The buoyancy issue is a fundamental one because, even if strictly speaking the system is miscible, the density distribution profiles are modified by interactions. This phenomenon can lead to a non-harmonic dynamics of the system and instabilities, which are generally difficult to describe. In addition, it prevents the direct measurements of spin properties like static spin-dipole polarizability $\mathcal{P}$ or spin-dipole oscillation frequency ω_{SD}, which are visible when the trap minima (hence density distributions) are slightly displaced one respect to the other from their common rest position (see next subsections).

Another issue concerning quantum binary mixtures is the critical velocity. *Critical velocity*
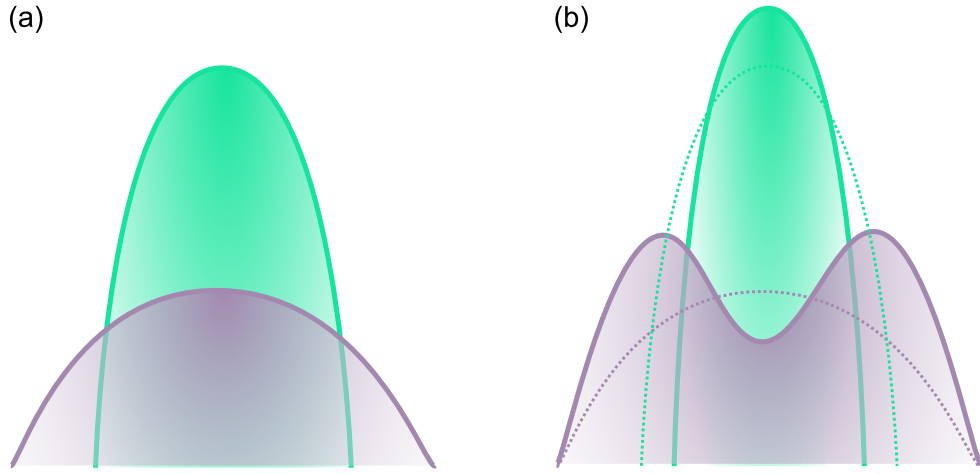
Figure 1.2: (a) Sketch of the density distribution arrangement in the case of a miscible mixture where $g_{11} \neq g_{22}$ and $g_{12} = 0$. The effect of having different intracoupling constants is to create two density distributions with different TF radii. (b) Comparison between the density distributions arrangement in the case of a miscible mixture with $g_{11} \neq g_{22}$ with (solid line) and without (dotted line) intercomponent interaction. Due to inter-component interaction the system tends to reduce the overlap are of the two atomic cloud by shrinking the density distribution of component 1 and by modified the inverted-parabola profile of component 2.

In a uniform binary mixture, the frequency of the Bogoliubov modes is

$$\omega_{d,s} = \sqrt{\frac{\hbar^2 k^2}{2m} \left(\frac{\hbar^2 k^2}{2m} + 2m c_{d,s} \right)} \tag{1.31}$$

where, assuming that $m_1 = m_2$, $n_1 = n_2 = n/2$ and $g_{11} = g_{22} = g$, the density (d) and spin (s) sound velocities are given by [42]

$$c_{d,s}^2 = \frac{n}{2m} \left(g \pm g_{12} \right). \tag{1.32}$$

The $+$ sign corresponds to density oscillation where the two fluids move in phase, while the $-$ sign is associated to out-of-phase spin oscillation. An interesting question concerns the stability of the system when the two fluids can move at velocities v_1 and v_2 and the sound velocity, which corresponds to the leading term in the Bogoliubov dispersion relation at small $\vec{k}$, is

$$c_{d,s} = \sqrt{c_0^2 + \frac{1}{4}v^2 \pm \sqrt{c_0^2 v^2 + c_0^4 g_{12}^2 / g^2}} \pm V, \tag{1.33}$$

where $c_0^2 = gn/2m$, $v = v_1 - v_2$, $V = (v_1 + v_2)/2$ and v_1, v_2 and $\vec{k}$ are assumed to lie on the same axis. Here, the condition for having stability is more complex than the single component case, where the Landau criterion [42] holds. In fact, the term $\pm V$ provides the instability associated to the Landau criterion if c becomes negative (energetic instability), while v plays a role in the dynamic instability. If $c_s < |v|/2 < c_d$ (where $c_{d,s}$ are given by Eq.1.32), the solution of Eq.1.33 is imaginary and the system shows a dynamic instability. Similarly, if $v > c_d$, c is real but the system develops dynamic instability beyond the phonon regime.

1.2.2 Collective oscillations

Generalizing the hydrodynamic formalism developed for a single BEC [74], it is possible to study collective oscillations of mixtures of BECs trapped in harmonic potentials. In particular, in the simplest symmetric case of $N_1 = N_2$ and $g_{11} = g_{22} = g$, the equation of the density oscillation remains equal to the case of a single component BEC

$$\frac{\partial^2}{\partial t^2}\delta n = \nabla \cdot \left[c^2(\vec{r})\nabla\delta n\right] \tag{1.34}$$

where $\delta n(\vec{r}, t) = n - n(\vec{r})$ is the change of the density profile with respect to the equilibrium profile and $mc^2(\vec{r}) = gn(\vec{r})$.

Instead, the equation for the spin density fluctuations for mixtures of BECs is different from the one describing the case of a single component BEC, reading as

$$m\frac{\partial^2}{\partial t^2}\delta s(\vec{r}) = (g - g_{12})\nabla \cdot \left[n(\vec{r})\nabla\delta s(\vec{r})\right] \tag{1.35}$$

where $\delta s(\vec{r}) = \delta n_1(\vec{r}) - \delta n_2(\vec{r})$ [42].

Since the equilibrium density profile is not modified and keeps the form $n(\vec{r}) = (\mu - V_{ext}(\vec{r}))/g$, all discretized collective frequencies holding for a single component BEC are still valid for a symmetric mixture simply introducing a normalization factor $\sqrt{(g - g_{12})/g}$.

Of particular interest is the spin-dipole (SD) oscillation, in which the two spin clouds move one with respect to the other with opposite phase. In the case of small oscillation amplitude with respect to the size of the condensates (linear regime), the relative motion is essentially "internal" since the edges of the density distributions do not move (as seen from GPE simulations). *Spin-dipole oscillation*

For the case of symmetric mixtures, the frequency of the spin-dipole oscillation [42, 70] can be expressed as

$$\omega_{SD} = \sqrt{\frac{g - g_{12}}{g + g_{12}}}\omega_{ho}. \tag{1.36}$$

The spin-dipole oscillation frequency is the simplest collective oscillation which is supported by the system and it can give information on the spin dynamics, as well as on the thermodynamics of the system. This frequency is predicted to be sensitive to the vicinity of the miscible-immiscible phase transition [70, 60].

So far, a direct measurement of this frequency was missing since the phenomena of phase-separation or buoyancy between the two spin components prevent observing this oscillation in the linear regime. Nevertheless, we measured it in Trento using a completely miscible mixture of sodium atoms (see Sec.1.3 and Ch.4).

1.2.3 Static polarizability

Another relevant quantity which is sensitive to the vicinity to the miscible-immiscible phase transition and that characterizes the thermodynamic behavior of the system is the static spin-dipole polarizability $\mathcal{P}$. It describes

the ability of the system to adapt to a relative displacement of the trapping potential minima for the two components and it is defined as

$$\mathcal{P} = \frac{x_1 - x_2}{2x_0} \tag{1.37}$$

where $x_1 - x_2$ is the distance between the centers of mass of the density distributions of the two spin components and $2x_0$ is the total distance between trap minima. This quantity exhibits a divergent behavior at the transition between the miscible and immiscible phases where important spin fluctuations can occur [61, 64].

The static SD polarizability is directly linked to the SD oscillation presented in the previous section. This relation emerges when the SD oscillation frequency is computed using the sum rule approach, which applies for small displacements of the trap minima with respect to the sample size. In this framework, it is possible to introduce the energy weighted $m_1(S_D)$ and the inverse energy weighted moment $m_{-1}(S_D)$ of the spin-dipole dynamic structure factor $S_{\text{SD}}(\omega)$ which reads as

$$S_{\text{SD}}(\omega) = Q^{-1} \sum_{m,n} e^{-E_n/k_B T} |\langle n|S_D|m\rangle|^2 \delta(\hbar\omega - \hbar\omega_{nm}) \tag{1.38}$$

where $S_D = \sum_k x_k \sigma_z^k$ is the spin dipole operator, $\omega_{nm} = (E_n - E_m)/\hbar$ are the Bohr frequencies and $Q = \sum_m e^{-E_m/k_B T}$ is the partition function. The energy weighted moment [42] is model independent and it is given by

$$m_1(S_D) = N\hbar^2/2m. \tag{1.39}$$

The inverse energy weighted moment is given by

$$m_{-1}(S_D) = \frac{N\mathcal{P}}{2m\omega_x^2}, \tag{1.40}$$

where $\mathcal{P}$ is fixed by the ratio between the induced spin displacement of the atomic clouds and the separation $2x_0$ of the two harmonic traps [70].
The estimate of ω_{SD} is provided by the ratio

$$\hbar\omega_{\text{SD}} = \sqrt{\frac{m_1(S_D)}{m_{-1}(S_D)}}, \tag{1.41}$$

hence, using Eqs.1.41, 1.39 and 1.40, the linear SD polarizability $\mathcal{P}$ can be computed at $T = 0$ from the value of ω_{SD} using the relation

$$\omega_{SD} = \frac{\omega_x}{\sqrt{\mathcal{P}}}. \tag{1.42}$$

1.2.4 Out-of-equilibrium mixture

An additional issue, which is independent of the interaction properties of the mixture, concerns the stability of the sample just after its splitting into two components which, as explained in the following, leads to an out-of-equilibrium configuration.

Let us consider a polarized sample at finite temperature T with a total number of atoms N. Typically, a fraction of the atoms is condensed (N_0/N), while the remaining (N_T/N) belong to the thermal cloud, such that

$$N = N_0 + N_T. \tag{1.43}$$

The splitting of the sample into two systems having $N/2$ atoms each, conserves the total number of particles N but not the temperature T. In fact, one can describe the system before the splitting and after in the new equilibrium configuration (labeled as ') as

$$\begin{cases} N = N_0 + N_T \\ N = 2N_0' + 2N_T'. \end{cases}$$

The number of condensed atoms (N_0') and the number of thermal atoms (N_T') in each sample after the splitting, can be estimated by considering that the main energetic contribution is given by the internal energy of the thermal distribution in the trapping potential, which is equal to

$$U = 3N_T k_B T. \tag{1.44}$$

Considering that for an ideal Bose gas in harmonic confinement $N_T \equiv N - N_0 = \xi(3)\left(\frac{k_B T}{\hbar \bar{\omega}}\right)^3$, where $\xi(n)$ is the Riemann ξ function and imposing energy conservation across the splitting procedure, one finds that the temperature of the systems reduces since

$$T' \sim 0.85T \tag{1.45}$$

From the new value of the temperature T' one can also estimate the new value of N_T' and N_0', which are

$$N_T' = 0.6N_T \quad \text{and} \quad N_0' = \frac{N_0}{2} - \frac{N_T}{10}. \tag{1.46}$$

This proves that, even if the absolute temperature of the system is lower, the two BEC distributions have less than half the initial number of condensed atoms. In fact some of the condensed atoms will be converted into thermal particles in order to conserve the energy of the system.

1.3 SODIUM PROPERTIES

In the previous section I have described systems made of two components, showing that binary mixtures can be either miscible or immiscible. While in the immiscible regime the two components tend to stay apart from one other, in the miscible one they tend to occupy the same volume. In practice, this is not always true. Because of buoyancy, in fact, the two condensates tend to rearrange their density distributions, preventing the possibility to study the dynamics of the system in the linear regime.
Of particular interest in this thesis are the experimental works realized using

atoms of the same atomic species occupying two different internal states. So far, most works were realized using rubidium atoms [19, 20, 75, 26, 27, 32]. Even if rubidium presents the great advantage of having accessible Feshbach resonances [76] for several mixture combination, the mixtures created to date present miscibility constrains since they can be either immiscible or affected by buoyancy.

An example of mixture extremely close to the phase transition and affected by buoyancy is reported in Fig.1.3, which corresponds to the case of a $|F = 1, m_F = -1\rangle$ and $|F = 2, m_F = 1\rangle$ Rb mixture.
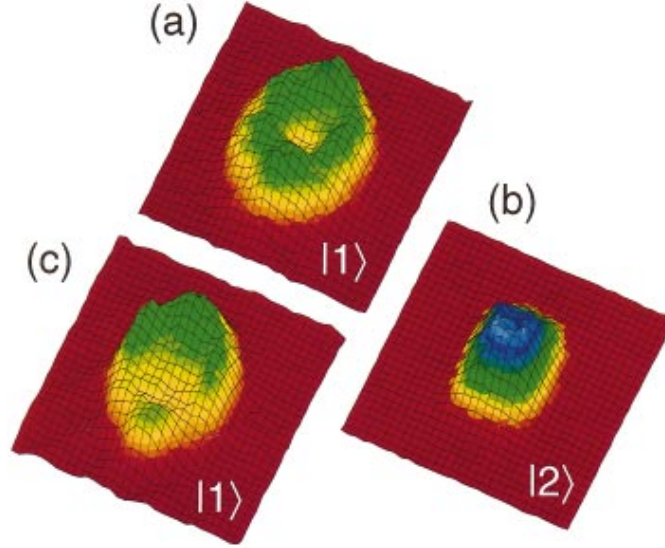

Figure 1.3: Experimental density profiles of the $|2,1\rangle + |1,-1\rangle$ rubidium mixture taken from [20]. The $|1\rangle$ component corresponds to the $|2,1\rangle$ state, while $|2\rangle$ corresponds to the $|1,-1\rangle$ state. The density profile of $|1\rangle$ (a) is larger and presents a crater in the region occupied by the $|2\rangle$ atoms (b). (c) Density distribution of $|1\rangle$ after introducing a non-zero relative sag.

From Fig.1.3 one can observe that component $|1\rangle$ has a larger distribution with respect to component $|2\rangle$, since $g_{11} > g_{22}$. In addition, it is visible that component $|2\rangle$ tends to minimize its volume, while the density distribution of $|1\rangle$ shows a depletion where the two components overlap. Thus, it is clear that these systems are not suitable to study static and dynamic properties in the linear regime, being not miscible in a strict sense.

Completely miscible sodium mixture   In this scenario, the sodium mixture $|F = 1, m_F = \pm 1\rangle$ is the ideal platform to study both static and dynamic properties in the linear regime, since it is completely miscible and symmetric [77]. In fact, it does satisfy the miscibility condition $|g_{12}| < \sqrt{g_{11}g_{22}}$, $N_1 = N_2$ and, since at low magnetic fields $g_{11} = g_{22} = g$, it is also not subject to buoyancy.

The values of the s-wave scattering lengths for the ground states of sodium (taken from [78]) are

$$a_{11} = a_{22} = 54.54(20)a_0 \qquad \text{and} \qquad a_{12} = 50.78(40)a_0 \qquad (1.47)$$

where a_0 is the Bohr radius.

Since $g_{12} \sim g$ the system is close to the miscible-immiscible phase transition, where the role played by interactions becomes crucial and is responsible

for the enhancement of the static SD polarizability with respect to the non-interacting system. Also the value of the SD oscillation frequency is sensitive to interactions, being five time smaller than the trap frequency.

Thus, the vicinity to the miscible-immiscibile phase transition is important since it permits to observe sizable interaction effects. However, when the system is extremely close to the phase transition (like in [20]) it is difficult to precisely control and study the system since it is deeply sensitive to other effects, such as asymmetries in the trapping potential [79]. In our case, $(g - g_{12})/g \simeq 7\%$ and the system can be consider stable, even if it is close enough to the miscible-immiscible transition to ensure sizable interaction effects.

1.4 WEAKLY INTERACTING TRAPPED BEC AT FINITE TEMPERATURE

At $T \neq 0$, the condensate density is modified because of thermal depletion and interactions with the thermal component should be taken into account.

The simplest theory describing the thermodynamic behavior of a trapped interacting Bose gas at finite temperature is based on the Hartree–Fock (HF) approximation [80, 81]. This theory assumes that, at equilibrium, the system can be described as a gas of statistically independent single-particle excitations, whose average occupation number of the i states is $n_i = \langle \hat{a}_i^\dagger \hat{a}_i \rangle$, being $\hat{a}^\dagger$ and $\hat{a}$ the single-particle creation and annihilation operator.

Hartree–Fock approximation

The energy of the system can be calculated by keeping only terms with an even number of creation/annihilation operators and setting

$$\langle \hat{a}_i^\dagger \hat{a}_k \rangle = n_i \delta_{ik} \tag{1.48}$$

$$\langle \hat{a}_i^\dagger \hat{a}_j^\dagger \hat{a}_k \hat{a}_l \rangle = n_i n_j (\delta_{ik}\delta_{jl} + \delta_{il}\delta_{jk}) \tag{1.49}$$

The thermal and condensed components can be separated by associating the role of the thermal part to the excited states $i \neq 0$ and the role of BEC to the lowest energy $i = 0$ state. Proceeding in this way the total energy of the system can be written as

$$E = \int d\vec{r} \left[\frac{\hbar^2}{2m} N_0 |\nabla \varphi_0|^2 + \sum_{i \neq 0} \frac{\hbar^2}{2m} n_i |\nabla \varphi_i|^2 + V_{ext}(\vec{r})(n_0(\vec{r}) + n_T(\vec{r})) \right.$$
$$\left. + \frac{g}{2} n_0^2(\vec{r}) + 2g n_0(\vec{r}) n_T(\vec{r}) + g n_T^2(\vec{r}) \right] \tag{1.50}$$

where the density of the condensate and thermal parts are

$$n_0(\vec{r}) = N_0 |\varphi_0(\vec{r})|^2 = |\Psi_0|^2 \qquad \text{and} \qquad n_T(\vec{r}) = \sum_{i \neq 0} n_i |\varphi_i(\vec{r})|^2,$$

respectively and $\varphi_i(\vec{r})$ are single particle wave functions normalized to unity. The average occupation number n_i can be found by minimizing the energy at fixed entropy and N, yielding to the Schrödinger-like equation

$$\frac{\delta E}{\delta \varphi_i^*} = n_i \epsilon_i \varphi_i \tag{1.51}$$

where ϵ_i is the energy of the i single-particle level. From Eq.1.51, when the chemical potential approaches the energy ϵ_0, one finds

$$\left(-\frac{\hbar^2 \nabla^2}{2m} + V_{ext}(\vec{r}) + g[n_0(\vec{r}) + 2n_T(\vec{r})]\right)\Psi_0 = \mu\Psi_0 \tag{1.52}$$

for the BEC part and

$$\left(-\frac{\hbar^2 \nabla^2}{2m} + V_{ext}(\vec{r}) + 2gn(\vec{r})\right)\varphi_i(\vec{r}) = \epsilon_i\varphi_i(\vec{r}) \tag{1.53}$$

for the excited single-particle states, where $n(\vec{r})$ is the total density of the system.

With respect to the GPE 1.6, Eq.1.52 takes into account the interaction with the thermal component being given by $2gn_T$, where the factor 2 comes from the exchange term in the calculation of E.

1.5 QUANTUM MIXTURE AT FINITE TEMPERATURE

The HF theory presented in the previous section is able to describe the thermodynamic behavior of the single component system in the presence of a thermal fraction. As seen in Sec.1.2, when dealing with a multi-component systems, the role of inter-species interaction should be taken into account as well. To do so, one has to replace the coupling constant g of the single component system, with the three coupling constants g_{11}, g_{22} and g_{12} characterizing interactions in a binary mixture.

In this framework Eq.1.52 can be rewritten, for each of the two component, as

$$\mu\Psi_1 = \left[-\frac{\hbar^2}{2m}\nabla^2 + V_1 + g_{11}(n_1^0 + 2n_1^T) + g_{12}(n_2^0 + n_2^T)\right]\Psi_1 \tag{1.54}$$

$$\mu\Psi_2 = \left[-\frac{\hbar^2}{2m}\nabla^2 + V_2 + g_{22}(n_2^0 + 2n_2^T) + g_{12}(n_1^0 + n_1^T)\right]\Psi_2 \tag{1.55}$$

where $g_{11,22} = 4\pi\hbar^2 a_{11,22}/m$ and $g_{12} = 2\pi\hbar^2 a_{12}/m$. The condensate densities are given by $n_{1,2}^0 = |\Psi_{1,2}|^2$ where we have assumed $N_1 = N_2$. The densities of the thermal distributions are described by the semi-classical equation

$$n_{1,2}^T(\vec{r}) = \frac{1}{(2\pi\hbar)^3}\int d\vec{p} f_{1,2}(\vec{p},\vec{r},t) , \tag{1.56}$$

where the Wigner distribution function of the thermal atoms [82] is given by

$$f_{1,2}(\vec{p},\vec{r},t) = \{e^{\beta[\vec{p}^2/2m + U_{1,2}^T - \mu_{1,2}]} - 1\}^{-1} \tag{1.57}$$

and the effective potentials for the thermal fluids are

$$U_1^T = V_1 + 2g(n_1^0 + n_1^T) + g_{12}(n_2^0 + n_2^T) \tag{1.58}$$

$$U_2^T = V_2 + 2g(n_2^T + n_2^T) + g_{12}(n_1^0 + n_1^T). \tag{1.59}$$

Considering the Bose function

$$g_{3/2}(z) = \frac{2}{\sqrt{\pi}} \int_0^\infty dx \frac{\sqrt{x}}{z^{-1}e^x - 1},$$ (1.60)

Eq.(1.56) can be simplified to

$$n_{1,2}^T = g_{3/2}(z_{1,2})/\lambda_T^3$$ (1.61)

where $\lambda_T = \sqrt{2\pi\hbar^2/(mk_BT)}$ is the de Broglie wavelength and

$$z_{1,2} = \exp[(\mu - U_{1,2}^T)/k_BT]$$ (1.62)

is the local fugacity of the spin components 1 and 2.

The equations reported above can be solved to find the ground state density distributions of the condensate and thermal atoms in the presence of the displacement $2x_0$ between the harmonic traps, obtaining thus the polarizability of the system as a function of x_0 and temperature. In this framework, the displaced potentials reads

SD polarizability at finite T

$$V_1 = V_{ho}(x - x_0, y, z) \quad \text{and} \quad V_2 = V_{ho}(x + x_0, y, z)$$ (1.63)

and, for the case of symmetric systems, $\mu_1 = \mu_2 = \mu$.

The BEC spin density, which corresponds to the relative distance between the two condensed component, can be found at low temperature by applying the Thomas-Fermi approximation and neglecting the interaction between the condensate and the thermal component as well as thermal-thermal interactions in the Gross-Pitaevskii equations (1.54,1.55). This yields to

$$S^0 = n_1^0 - n_2^0 = -x_0 \frac{g + g_{12}}{g - g_{12}} \frac{\partial n^0}{\partial x},$$ (1.64)

while for the thermal part one finds

$$S_{in}^T = n_1^T - n_2^T = -\frac{1}{k_BT\lambda_T^3} z \frac{\partial g_{3/2}(z)}{\partial z} \frac{2g}{g - g_{12}} m\omega_x^2 x_0$$

in the inside region where the thermal part interacts with the condensate. In addition, without any external perturbations, one has

$$\frac{\partial n^T}{\partial x} = \frac{1}{k_BT\lambda_T^3} z \frac{\partial g_{3/2}(z)}{\partial z} \frac{2g}{g + g_{12}} m\omega_x^2 x_0,$$

so that

$$S_{in}^T = n_1^T - n_2^T = -x_0 \frac{g + g_{12}}{g - g_{12}} \frac{\partial n^T}{\partial x},$$ (1.65)

In a similar way the spin density of the outermost thermal component can be derived finding that

$$S_{out}^T = n_1^T - n_2^T = -x_0 \frac{\partial n^T}{\partial x}.$$ (1.66)

The polarizability of the condensed ($\mathcal{P}^0$) and thermal ($\mathcal{P}^T$) part are found by integrating their spin density

$$\mathcal{P}^0 = \int x S^0 d\vec{r} / N_0 \qquad (1.67)$$

and

$$\mathcal{P}^T = \int x S^T d\vec{r} / N_T. \qquad (1.68)$$

From Eqs.1.64,1.65 and 1.66 two main aspects emerge. One is the distinction between the thermal atoms occupying the region where the BEC is present from the atoms occupying the region outside the BEC distribution. The second aspect regards the presence of the term $(g + g_{12})/(g - g_{12})$ both in the spin density of the condensed and thermal internal part. Both these arguments underline the importance of the inter-component interaction, which causes an enhancement of the polarizbility of the system.

However, increasing the temperature it is no longer possible to ignore the presence of the thermal component, and the behavior of the SD polarizability as a function of temperature can be computed by solving in a consistent way the coupled Hartree-Fock equations for the condensate and for the thermal part. From the theoretical simulations, it turned out that the role of the interaction with the internal thermal component causes a further increase of the static SD polarizability of the condensate, as shown in Fig.1.4.
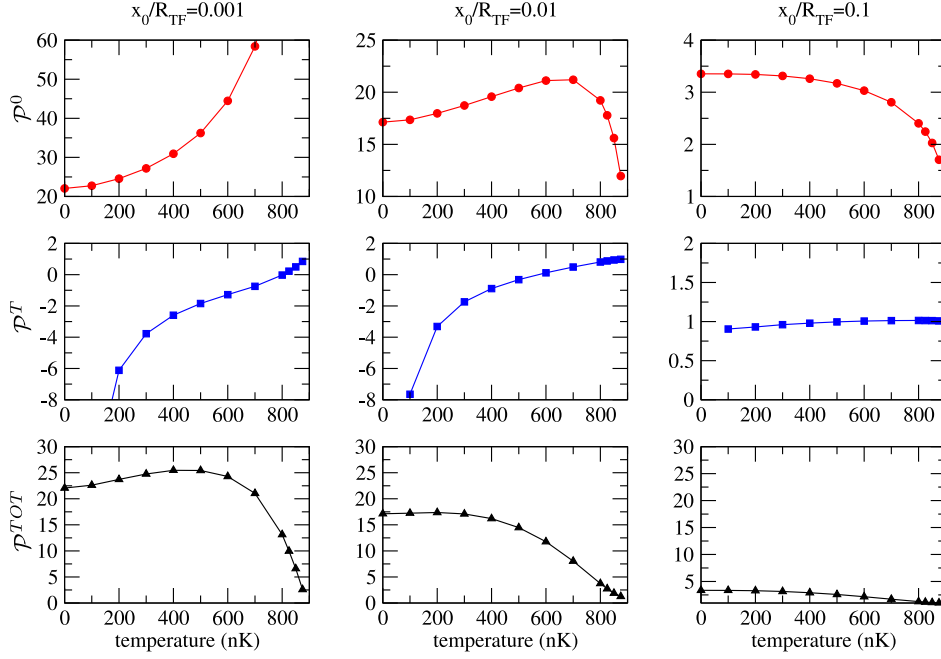
Figure 1.4: Computed SD polarizability of the condensed $\mathcal{P}^0$ (upper row), thermal $\mathcal{P}^T$ (middle row) and total $\mathcal{P}^{TOT}$ (bottom row) atoms as a function of temperature in the case of $N_1 = N_2 = 10^5$ and $(\omega_x, \omega_y, \omega_z)=2\pi(44.5,1400,1400)$Hz. In the left column are reported the results obtained for $x_0/R_x = 0.1\%$, in the central column the results obtained for $x_0/R_x = 1\%$ and in the right column are the results obtained for $x_0/R_x = 10\%$. The critical temperature of the system computed for a non-interacting system is 930 nK. The $(g + g_{12})/(g - g_{12})$ which affects the polarizability of both BEC and thermal cloud is relevant only in the linear regime $x_0\mathcal{P} \ll R_{TF}$, which corresponds to the first column of the figure. Increasing the displacement of the trap minima, interactions between spin components become less important leading to polarizability contributions close to 1 (third column).

In the same figure the behavior of the polarizability associated to the thermal cloud and the total polarizability, which is computed as

$$\mathcal{P}^{TOT} = \frac{N_0\mathcal{P}^0 + N_T\mathcal{P}^T}{N}, \tag{1.69}$$

are shown for different value of x_0.

From the simulations, it emerges that both the condensed and the thermal polarizability are modified by their mutual interaction, while the total polarizability remains, in first approximation, equal to the one expected for the $T = 0$ case.

Additional comments on the SD polarizability and its physical meaning are reported in Chapter 4, where the main results of my research work are discussed.

2 | EXPERIMENTAL APPARATUS

Contents

Experiments with ultracold gases require well controlled experimental conditions where many physical parameters must be precisely varied in a reliable way. To fulfill these requirements a control over many instruments is typically needed. In this chapter I will present a detailed description of the experimental apparatus. First the atomic source and the vacuum apparatus are described. Then the laser systems used to produce visible and infrared radiation are described. The following section is devoted to the description of the magnetic trap used to create the BEC and, more in general, all the coils and their use is also illustrated. After the magnetic trap the dipole trap is presented in detail. The electronic control system is also described, making it clear how we control all the different steps of the experimental sequence. Finally the description of the imaging setup is reported in the last section, where the fitting procedures are also explained.

2.1   ATOMIC SOURCE AND VACUUM APPARATUS

Atomic source

Since the first observations of the Bose–Einstein condensate with rubidium and sodium atoms [1, 2], the interest in this kind of systems has considerably grown, leading to the development of new efficient atomic sources. Atomic sources based on laser cooling can be divided into two main classes.

- A first class exploits dissipative light forces and inhomogeneous magnetic fields to slow down a thermal flux of atoms which are coming from an oven. An usual implementation of this type of sources is the Zeeman slower (ZS), a stage where fast atoms are slowed down by means of a counter-propagating laser beam and a specific configuration of the magnetic field [83]. The slowed atoms can then be trapped and cooled in magneto-optical traps (MOTs) [84].

- The second class of atomic sources uses atomic vapors directly loaded and cooled in a MOT: these setups present a simple design, but they provide satisfying performances only for medium and heavy atoms like potassium, rubidium and cesium [85, 86, 87].

Working with light alkali species (such as sodium or lithium) can lead, in case of a highly efficient Zeeman-Slower (ZS) stage, to experiments with a higher number of atoms [88] with respect to experiments performed with heavier atoms. Anyway, even if these systems are suitable to capture a large number of atoms, they present some nontrivial drawbacks. Firstly, the ZS stage can be affected by losses due to the atomic beam divergence. Secondly the experimental apparatus is necessarily larger and more complex to operate.

In 2009 a new type of atomic source based on a 2D MOT stage was developed for lithium [89], leading to more compact experiments without affecting the total number of captured atoms.

The system used in our experiment [90] extended this approach to sodium atoms, combining a 2D MOT with a compact ZS stage.

Our atomic source is based on an oven filled with metallic sodium which is heated up to 250 °C (more than 150 °C above the melting temperature) allowing atoms to evaporate in the vacuum system. The atomic cloud produced by the evaporation is moving upward generating a flux that permits to transversely (*y-z* plane) load the 2D MOT. In addition, using a laser beam pointing opposite to the flux direction, it is possible to implement a ZS, which enhances the flux by more than an order of magnitude.

The magnetic fields required to operate the 2D MOT and the ZS are obtained by means of four sets of permanent magnets located close to the 2D-MOT plane (see Fig.2.1).

Finally, a resonant-light beam aligned along the axial unconfined direction *x*, labeled as push beam, is used to push the atoms towards the final science chamber located ∼30 cm away from the 2D MOT creating a collimated atomic beam with a flux of more than 4×10^9 atoms per second.

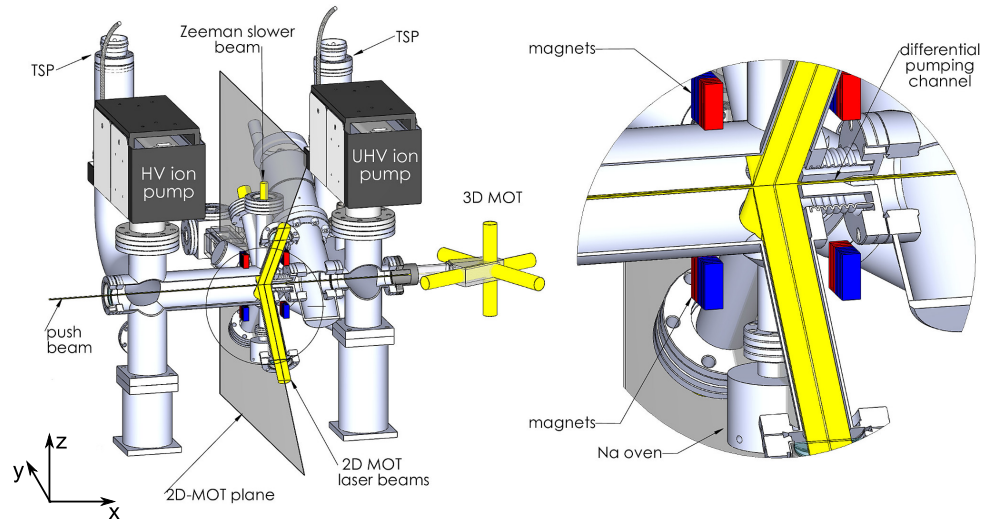Beams and magnets positions are illustrated in Fig.2.1.

Figure 2.1: Scheme of the vacuum apparatus showing the position of the pumps, the light beam directions and the location of the permanent magnets. On the right a magnified detail of the 2D-MOT plane is reported.

Vacuum system

The vacuum apparatus hosting the experiment is divided in two main parts: the high-vacuum (HV) chamber where the oven, the 2D-MOT and

the ZS are located and the ultra-high-vacuum (UHV) chamber where a pressure lower than 1×10^{-10} mbar is reached and the experiment is carried out. These two parts are joined together via a differential pumping channel that provides a differential pressure up to 10^3.

The pumping system is composed of two ion pumps *VARIAN STARCELL* (nominal pumping speed of 55 ls^{-1}) and two *VARIAN TITANIUM SUBLI-MATION PUMPS* (TSP). Each of the two parts composing the vacuum apparatus hosts one ion ad one sublimation pump as reported in Fig.2.1.

It is important to note that all the metallic part composing the vacuum apparatus are manufactured using *AISI 316* stainless steel. This allows for baking, to reduce outgassing and limit the magnetization of the material induced by external electromagnets. It also guarantees, in first approximation, a negligible magnetic permeability of the system.

The UHV part of the vacuum apparatus ends with the science chamber where the experiment is performed (see Fig.2.1). The science cell presents a polyhedron shape with 5 mm thick windows. The size of the cell is about 80 mm × 60 mm × 35 mm.

Science chamber

The particular design of the cell is needed in order to avoid the overlap among the 3D-MOT beams and the axis of the flange which connects the UHV cell to the atomic source. Since the BECs production requires the use of magnetic fields controlled with high precision, the science chamber must satisfy some fundamental constrain. It has to be non-magnetic and highly resistive (to prevent eddy currents), it must guarantee a small hydrogen outgassing (to ensure high quality vacuum) and must allow large optical accessibility to the atomic sample. For all these reasons the science chamber is manufactured using annealed (with molecular bonding) quartz and the four largest surfaces are anti-reflection coated on the outer side (R$\sim$ 0.5% on the spectral range $500 \div 1100$ nm). A picture of the quartz cell is reported in Fig.2.2.

As discussed in chapter 5, an additional experimental setup was recently

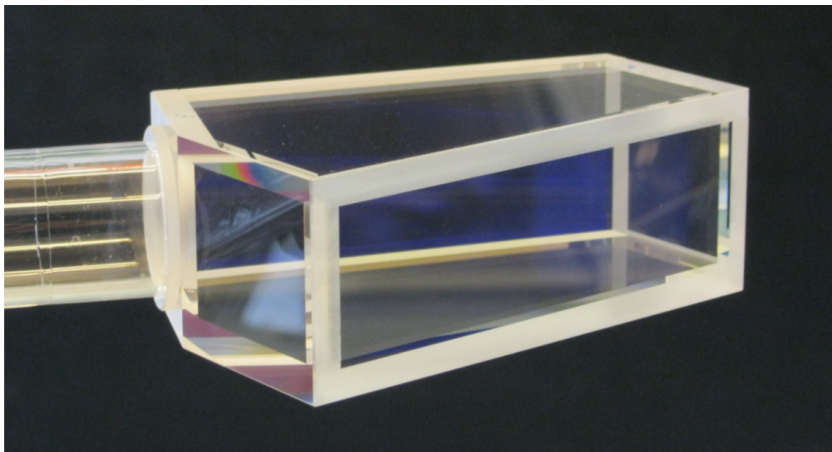**Figure 2.2:** Quartz science chamber used to host the laser cooled and to trap the sodium atoms.

The new experimental apparatus

built in order to perform novel classes of experiments with ultra-cold atoms. This new setup distinguishes from the first one mainly in the science chamber. The UHV cell in the new setup cell is a quartz octagonal shaped cell

which is sustained by a quartz tube of 12.5 mm radius and 65 mm length (see Fig.2.3). This tube is connected to the vacuum apparatus trough a glass-to-metal junction and a CF35 flange. One of the eight flat parts in the horizontal plane of the cell is welded to the tube used to support the cell itself, while the remaining seven faces have a 19 mm diameter window each. In addition two extra 58.4 mm diameter windows are located at the top and at the bottom of the UHV cell. The seven small windows are 4.8 mm thick, whereas the two largest windows are 7.8 mm thick. Since the BEC is created at the center of the quartz cell in a region of almost 1 cm^3 all the windows have a broadband anti-reflection treatment both on the inner and outer side in order to supress fringes resulting from spurious reflection of the laser beam. Considering all the windows as an integral part of the quartz cell this can be approximated with a cylinder of 45 mm height and 75 mm diameter. A picture of the new science chamber is reported in Fig.2.3. The octagonal design of the new science chamber guarantees that all the incoming beams cross the quartz cell at $\sim 90°$ in order to exploit the maximal efficiency of the coating treatment of the eight windows. For more details on the octagonal quartz cell see chapter 5.
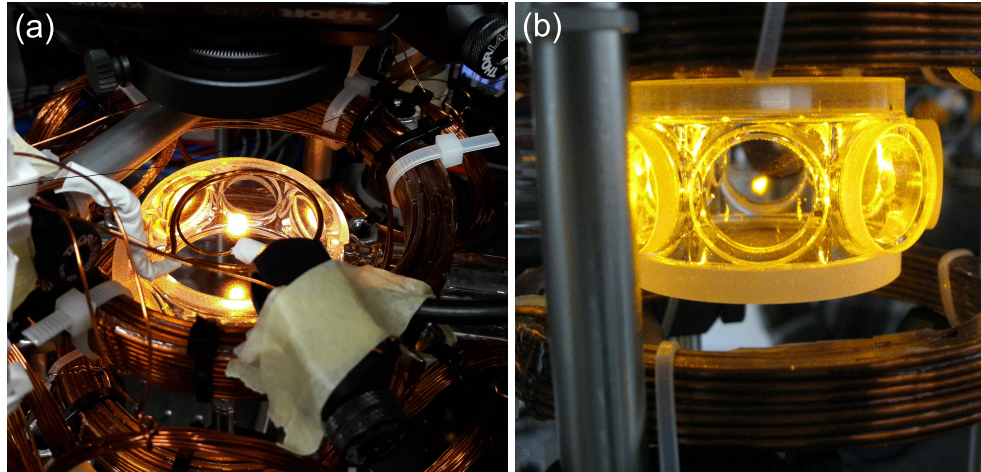

Figure 2.3: (a) Picture of the octagonal quartz science chamber from above. (b) Picture of the octagonal quartz cell hosting the atomic sodium cloud in 3D-MOT configuration.

2.2 LASER SYSTEM

Cooling transition

Laser cooling is a fundamental step to reach quantum degeneracy in all experiments with ultra-cold atoms. Atoms close to room temperature can be cooled down to some tens of μK thanks to the combination of dissipative light forces which acquire a space dependence due to magnetic fields. To reach these temperatures, the cooling laser light must satisfy some properties in terms of spectral linewidth, polarization and stable frequency detuning from the atomic resonance.

We use sodium which is an alkali atom and its main electronic properties are determined by its valence electron. The nuclear spin of sodium is I=$\frac{3}{2}$

[91] therefore its fine-structure ground state splits in two levels labeled as $F = 1$ and $F = 2$ (see A). The most convenient closed cooling transition is $3^2S_{1/2} : F = 2 \leftrightarrow 3^2P_{3/2} : F' = 3$, which corresponds to an optical wavelength of 589.16 nm in vacuum. Here it is important to note that, since there is a non-negligible probability that some atoms are excited to the $F' = 2$ state via off-resonance excitation, a repumper light is also necessary. This is achieved tuning the laser light to frequency resonant with the transition $3^2S_{1/2} : F = 1 \leftrightarrow 3^2P_{3/2} : F' = 2$ that prevents optical pumping in the dark ground state $F = 1$ during the cooling stage.

Master source

Even if the laser-cooling radiation is not directly accessible with diode laser, the recent development in the field of quantum dot laser technology permits to reach a region of the spectrum in the near-infrared (1100-1200 nm). Thus, using a frequency doubling process, it is possible to use solid state laser systems also for sodium. The master source used to generate the near-infrared light is wavelength stabilized on an extended cavity mounted in the Littrow configuration [92]. The active medium used is a diode based on InAs quantum dots (*INNOLUME GC-1178-TO-200*), exhibiting gain between 1140 to 1200 nm. The wavelength discrimination is obtained using a holographic grating with 1200 lines per mm. The length of the cavity is about 15 mm, giving a free-spectral-range of the cavity is ∼10 GHz. The orientation of the grating can be changed in order to tune the output wavelength. In addition, a fine tuning of the wavelength can be obtained thanks to a voltage applied to a piezoelectric crystal fixed to the grating holder.

The temperature of the diode is stabilized using a controller (TEC) driving a Peltier-cell, while the stabilization of the master frequency is obtained via frequency modulated saturated absorption spectroscopy performed on a sodium vapor cell using resonant light. The dispersive signal obtained taking the derivative of the spectroscopy signal acts as an error signal of a feedback loop controller which applies a voltage to the piezoelectric crystal of the master cavity.

Near-infrared light amplification

The master laser light is then amplified with a Raman fiber amplifier (*MPB RFA-P-8-1178-SF*) which is pumped with an Ytterbium fiber laser. The input laser light is ∼ 15 mW and the output light, which maintains the same optical properties, can reach up to 8 W (usually the output power is set to 6.5 W). Further details on the Raman amplification system can be found in [93].

Duplication cavity

The amplified infrared light is then frequency doubled by means of a lithium triborate LiB_3O_5 non-linear crystal which is placed in a resonant cavity. The non-linear crystal is placed in a bow-tie cavity of 300 mm length and a finesse of about 150. The temperature of the crystal is controlled by a TEC and is set to approximately $45°C$. The duplication cavity, which can produce about 3.5 W of yellow light at 589 nm, couples to a single transverse and longitudinal mode and is stabilized in length by means of Hänsch and Couillaud locking [94]. The yellow light from the duplication cavity is then distributed into several beams, each independently controlled in intensity and frequency by means of acousto-optic modulators (AOMs) and electro-optic modulators (EOMs). These devices are located along the path of each beam as indicated in Fig.2.4. For more details on the operative function of the saturated absorption spectroscopy as well as of the AOMs and EOMs see [95, 96, 97].
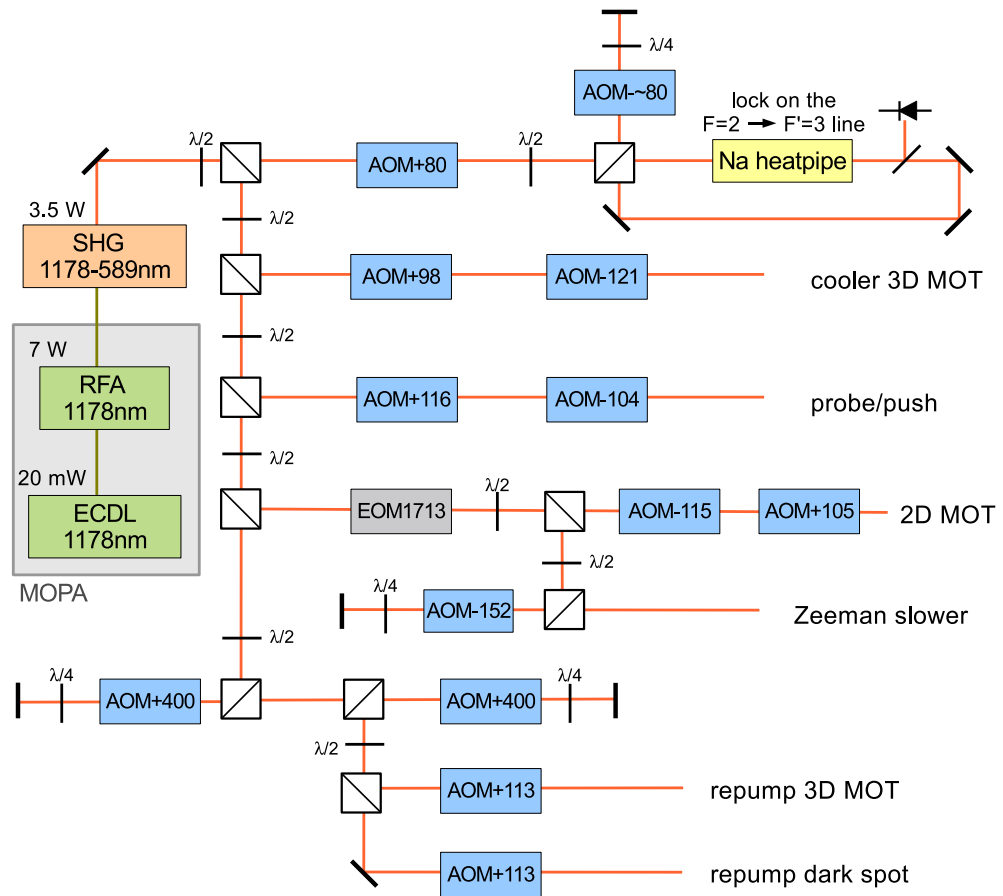
Figure 2.4: Schematic sketch of the optical setup used to produce the light at 589 nm needed to laser cool sodium atoms. The lenses used to collimate and to focus the beams are not drawn. The 3.5 W of light coming out from the duplication cavity is divided into different beams thanks to the *polarizing beam-splitter* (PBS) cubes located on the optical table. These beams can be tuned in frequency using AOMs and EOMs as indicated in the figure.

Each beam is coupled into an optical fiber (*SCHÄFTER & KIRCHHOFF PMC-630-4.5-NA011-3-APC-900-P*) which brings the light from the laser table to the one devoted to the experiment. Each light arm is also equipped with a digitally controlled mechanical shutter (sec.2.5) located in front of the fiber input. By acting on these shutters it is possible to completely block the yellow light traveling through the fibers up to the experimental table. The typical response time of these devices is $\sim$ 100 ms.

Optical dipole potentials   Optical dipole potentials [98], which are obtained from far-detuned laser light, are used to trap the atoms as well as to change their dynamics. The conservative dipole potential exerted on the atoms can be either attractive (red-detuned light) or repulsive (blue-detuned frequency). The reason of conservativity relies on the low scattering cross-section at sufficiently large detunings, which reduces the heating in the system. Optical potentials can be modeled essentially at will, varying their intensity and geometry.

To obtain the laser radiation needed to create optical potentials, a commercial Nd:YAG laser in MOPA configuration (*INNOLIGHT MEPHISTO MOPA*) is used, providing up to 42 W of light at 1064 nm. This light presents a single longitudinal mode with a spectral linewidth of $\sim$ 1 kHz. This infrared

light can be directly used to generate attractive optical potentials, being red-detuned with respect to the D_2 atomic transition of sodium.

In addition it is possible to generate repulsive potential since a PP-SLT[1] non-linear crystal is placed along the infrared light path. In this case, sending an infrared beam of about 30 W trough the crystal produces more than 6 W of green light at a wavelength of 532 nm. Note that for the work described in this thesis, the green light at 532 nm has never been used.

2.3 MAGNETIC FIELDS

To reach quantum degeneracy, the use of magnetic fields is required in order to manipulate the neutral atoms. In fact, several magnetic configurations are used during the experimental procedure, for example during the laser cooling stages or to create conservative traps [99].

2D-MOT and Zeeman Slower

The very first stages of the experimental sequence (2D-MOT and ZS) require a relatively simple magnetic configuration that is obtained using 4 stacks of 9 neodymium permanent magnets (*ECLIPSE N750-RB*). These magnets are placed around the HV chamber in order to obtained a quasi-2D quadrupole. The magnetic field is zero along the unconfined x axis and its modulus varies linearly along the transverse directions. Far from the 2D-MOT region the magnetic field reaches its maximum, then it decays with the distance. The tails of this vanishing magnetic field are exploited to realize the compact ZS [90].

Driven magnetic electromagnets

Once that all the atoms are transferred from the HV region to the quartz cell, the experimental procedure requires a more dynamic control of the magnetic field. This control is achieved thanks to an electric circuit (Fig.2.5) which controls a set of several coils. These coils are used to generate the magnetic field configurations needed during the experiment. In our experimental procedure three main configurations are required:

- MAGNETO-OPTICAL TRAP   The experimental sequence starts with a dark spot 3D-MOT [100], which is obtained using a quadrupole magnetic field, three orthogonal pairs of counter-propagating laser cooling beams and a single "hollow" repumping beam. This beam, which is imaged on the atomic cloud, is created by means of an 8 mm black dot placed along the beam's path. The black dot absorbs the light and only the outer profile of the beam is able to pass, so that an hollow Gaussian beam is created.
  Before transferring all the atoms to the magnetic trap, a sub-Doppler stage is necessary. This is performed via optical molasses in absence of magnetic fields [101] which leads to almost 3×10^9 atoms at 50 μK.

- MAGNETIC TRAP   Once that the atoms were sub-Doppler cooled, they are transferred to a Ioffe–Pitchard conservative magnetic trap (MT) [102]. A confining cigar-shaped potential is then created thanks to the non-vanishing magnetic field.

- MAGNETIC LEVITATION   Since the atomic cloud experiences gravity, a procedure to levitate the atoms is often required. In fact this is

---

1 Periodically Polled Stoichiometric Lithium Tantalate

crucial to observe atomic expansion or dynamics and to obtain information about the atom numbers. The atoms' levitation is obtained via a magnetic field gradient of about 8 Gcm^{-1} which is applied along the z direction. In this way the atomic cloud can expand in time-of-flight (TOF) without falling.

Ioffe-Pitchard trap

The Ioffe–Pitchard trap used in the experiment is based on a static magnetic field (presenting a cylindrical symmetry) with a non-zero magnetic field minimum which prevents from Majorana [103] losses. Along the axial direction the magnetic field is quadratic with a bias term $B_x = B_0 + B'' x^2/2$. To satisfy the Maxwell's equation, the magnetic field in the harmonic approximation must be:

$$\vec{B}(x,y,z) = B_0 \begin{bmatrix} 0 \\ 0 \\ 1 \end{bmatrix} + B' \begin{bmatrix} x \\ -y \\ 0 \end{bmatrix} + \frac{B''}{2} \begin{bmatrix} -xz \\ -yz \\ x^2 - \frac{x^2+y^2}{2} \end{bmatrix}. \tag{2.1}$$

The trapping potential depends only on the modulus of $\vec{B}$ and the interaction of the atoms with the external magnetic field is given by

$$U_{|F,m_F\rangle}(\vec{r}) = \mu_B g_F m_F |\vec{B}(\vec{r})|, \tag{2.2}$$

where μ_B is the Bohr magneton, $|F,m_F\rangle$ defines the internal Zeeman state of the atoms and g_F is the Landè factor. Considering low-field-seeking states[2] and low-temperature regime ($\mu B_0 > k_B T$), the trapping potential can be approximated to:

$$U_{|F,m_F\rangle} \approx \mu_B g_F m_F B_0 + \frac{1}{2} m \omega_\perp^2 \left(y^2 + z^2 \right) + \frac{1}{2} m \omega_x^2 x^2. \tag{2.3}$$

Here the radial trap frequencies and the axial one are respectively $\omega_\perp = \sqrt{(\mu_{\text{at}}/m)\left(\frac{B'^2}{B_0} - \frac{B''}{2}\right)}$ and $\omega_x = \sqrt{(\mu_{\text{at}}/m)B''}$ where μ_{at} is equal to $\mu_B|g_F m_F|$. It is now important to note that for a higher temperature regime the atoms experience a linear confinement along the radial direction that is exploited for evaporative cooling (see sec.3.1).

The value of $\mu_B g_F m_F B_0$ sets the bottom of the trap and can be changed to

Electrical circuit and coils

modify the radial confinement and hence the aspect ratio $\omega_\perp/\omega_x$.

In the experiment the magnetic field minimum of the 3D-MOT and of the MT are located in the same spatial point so that it is possible to switch from one configuration to the other without moving the atoms. Generally this is not possible since gravity affects the trapping potential displacing its minimum by the so-called gravitational sag $\Delta z = g/\omega_z^2$ (see Sec.4.2).

The different magnetic configurations described above are obtained using the electrical circuit illustrated in Fig.2.5.

This circuit exploits electro-mechanical relays switches and insulated-gate bipolar transistors (*SEMIKRON SKM400GAL12E4*). These IGBTs are mainly

---

2 If $U_{|F,m_F\rangle}(\vec{r}) > 0$ atoms are attracted to the minimum of the potential, if $U_{|F,m_F\rangle}(\vec{r}) < 0$ atoms are attracted to the maximum of the potential.
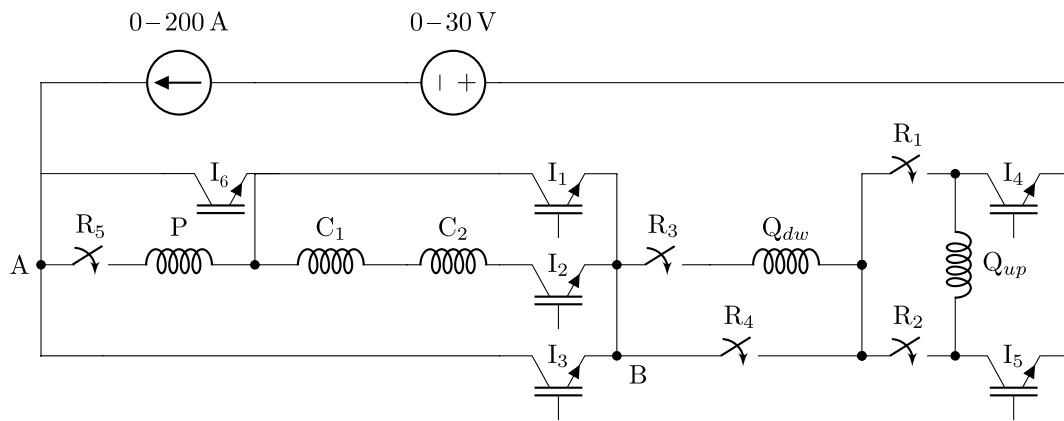
Figure 2.5: Scheme of the electric circuit used to generate the magnetic fields needed to perform all the configurations during the experimental sequence.

used as fast switches, being their response time faster than the relays' one (1 μs against 10 ms). These devices, however, can also be used as variable resistors, if driven with an analog voltage. The continuous current flow in the circuit is driven by two power supplies (*DELTA ELEKTRONIKA SM30-200*) which can be programmed to provide up to 200 A with a maximum rms-ripple noise of ~20 mA.
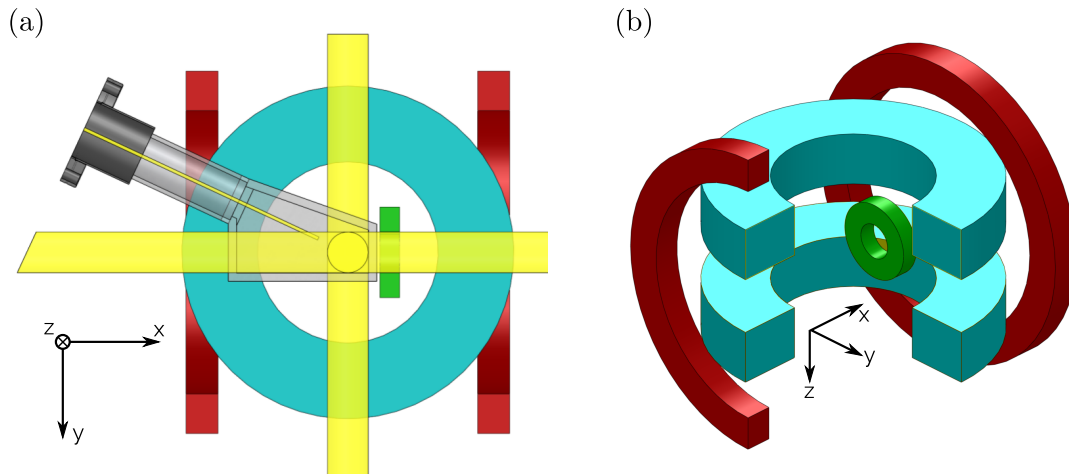

Figure 2.6: (a) Top view of the main coils used in the experiment. The quadrupole coils are drawn in azure, the pinch coil in green and the compensations coils in red. In addition the push and the MOT beams are drawn in yellow. (b) 3D-view of the main coils constituting the magnetic circuit of the experiment.

The coils constituting the high-current electrical circuit are shown in Fig.2.6. In the following, the role of all these coils is explained in detail.

- The quadrupole field used for the dark-spot 3D-MOT, as well as for the MT trap is obtained using a pair of twin coils (azure coils in Fig.2.6) in anti-Helmholtz[3] configuration. Each quadrupole coil is composed of 72 windings around an internal radius of 5.5 cm and are located at ±2 cm along the vertical direction (where zero is the center of the MT). The

---

[3] The distance between the center of the two coils is equal to their radius and the current flowing is the same but has opposite direction.

	B_0 [G]	B' [$G\ cm^{-1}$]	B'' [$G\ cm^{-2}$]	I_{tot} [A]
I_{ht}	3.8	12	118	200
I_t	1.9	106	59	100
I_s	0.9	53	29.5	50

Table 2.1: Trap parameters for the three regimes.

magnetic gradient per units of current produced by the coils in Ioffe–Pitchard configuration is $B'/I = 1.06\,\mathrm{G/cmA}$, while the magnetic field curvature is given by $B''/I = 0.59\,\mathrm{G/cm^2A}$.
The atoms' levitation is obtained by flowing the current in the lower coil only.

- The pinch coil (green coil of Fig.2.6) is activated in the magnetic trap configuration to create a non-zero magnetic field minimum. It is composed of 12 winding around an internal radius of 1.3 cm and is 2 cm displaced from the center of the trap along the x direction. This coil is able to produce, at maximum current, a magnetic field $B_0 \sim 180\,\mathrm{G}$ and a magnetic gradient of the order of $150\,\mathrm{G/cm}$.

- An additional pair of twin coils, labeled as compensation coils (red coils in Fig.2.6), are used to compensate the bias field B_0 produced by the pinch coil. In this way a more tight radial confinement can be reached. These coils, which produce an almost static magnetic field, are composed of 16 wingdings around an internal radius of 8.7 cm and are placed at ± 7.5 cm along the axial direction.

All these coils are water cooled through high pressure temperature stabilized water flowing in the hollow core of the copper wire constituting them.

In addition, other five pairs of smaller coils are present. These are labeled as shim or fine-tuning coils. The shim coils are three independent coils in Helmholtz[4] configuration. These coils have their axes oriented along the three orthogonal direction x,y and z. The current flowing in these coils, which is manually set using three dedicated power supplies (*DELTA ELEK-TRONIKA ES 015-10*), is tuned to have an isotropic expansion phase during the optical molasses.

The fine-tuning coils are oriented along the x and y directions and they are set in quasi anti-Helmholtz and Helmholtz configuration respectively. The coils along $\hat{y}$ are used to fix a quantization axis during the TOF imaging, while the ones along $\hat{x}$ are used to generate a magnetic gradient along the axial direction. A sketch of the complete configuration of all the coils used in the experiment is represented in Fig.2.7.

The magnetic trap usually operates within three regimes, whose parameters are reported in Table 2.1. The three regimes are:

- High Temperature Regime I_{ht}: this is the loading configuration and it is used only for the first stage of the evaporative cooling, being the sample in a thermal regime at a temperature of a few μK;

---

4 The distance between the center of the two coils is equal to their radius and the current flowing is the same.
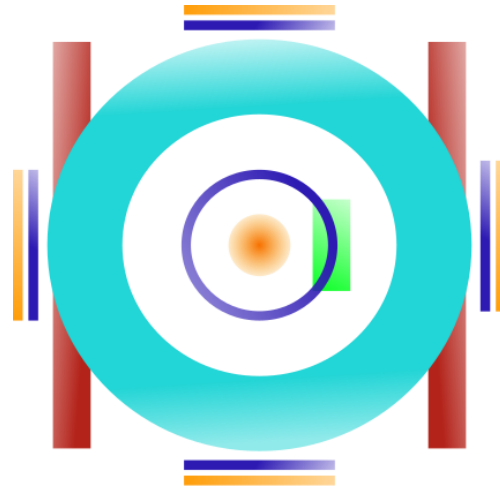
Figure 2.7: Top view of all the coils used to reach the quantum degeneracy. The quadrupole coils are drawn in azure, the pinch coil in green, the compensations coils in red, the shim coils in blue and the fine-tuning ones in orange.

- Tight Confinement I_t: here the quantum degeneracy is reached with a tightly-confined BEC and the temperature is reduced in order to avoid three-body collisions;

- Shallow Confinement I_s: here the quantum degeneracy is reached with a shallow confinement which permits to work with lower value of the magnetic field.

In sec.3.1 a more detailed description of the magnetic trap sequence is reported. For more details on the magnetic trap realization and properties see [104].

Even if not strictly related to the electrical circuit, it is fundamental to mention that the experiment is equipped with different antennas which are used to irradiate radio-frequency (RF) or μ-wave signals on the atoms. All these antennas are placed in proximity of the UHV chamber and are driven with DDSs (RF) or μ-wave generators (*MARCONI 2024*). Depending on the quantization axis and on the shape of the antenna, which can be both circular and hook-shaped, the irradiated wave can induce with a fairly good approximation π-transition or $\sigma^{\pm}$-transition.   *Antennas*

2.4 OPTICAL–DIPOLE TRAP

In order to create a mixture of different internal hyperfine and Zeeman states of sodium atoms, one must be able to trap atoms independently from their magnetic configuration. In this way it is possible to manipulate the ultra-cold atomic cloud, transferring the whole or part of the sample from one state to another. The magnetic trap is clearly not suitable to create such a systems, while the optical-dipole trap is the appropriate platform to create a multi-component BEC. The techniques used to create the specific mixture used for the work reported in this thesis are described in detail in 3.3. As already discussed in sec.2.2, the optical trap is obtained using far-detuned laser light. This light is generated by a Nd:YAG MOPA laser source deliver-

ing radiation at 1064 nm, to which I will refer as infrared (IR light). Since in some experiments it is necessary to create repulsive potentials, the IR light passes trough a non-linear crystal able to generate light at 532 nm (labeled as green light). The infrared and green lights are splitted by a cold mirror[5] and the green light is then blocked with a damper. The infrared light is then divided into two different beams, each of them passing trough a AOM and then sent into an photonic crystal high-power optical fibers (*NKT-PHOTONICS LMA-PM-10*). In Fig.2.8 a sketch of the initial paths of the two infrared beams is shown.
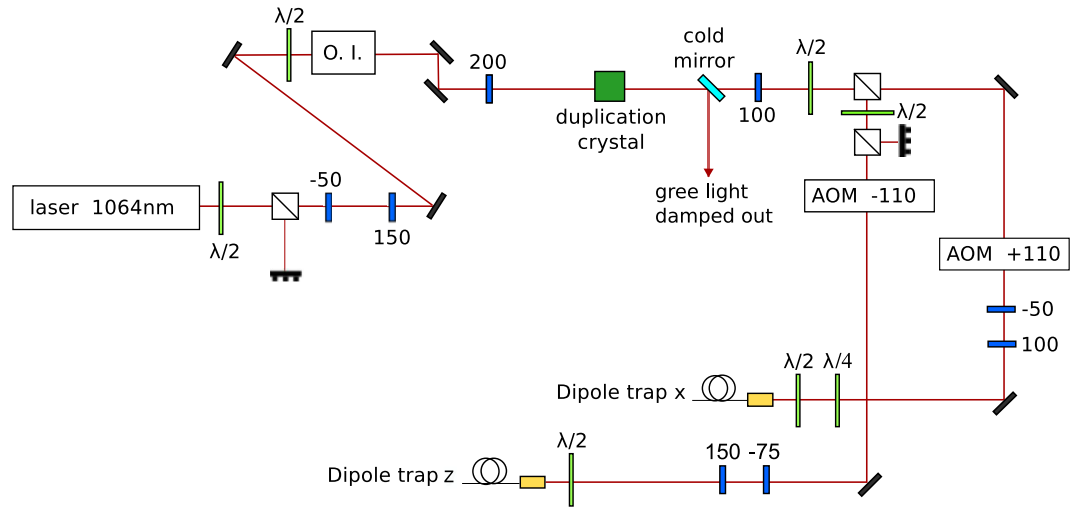

Figure 2.8: Scheme of the IR beam from the laser source up to the fiber input.

Once that the IR beams are sent to the fiber they travel along different paths, both reaching the atoms. One beam propagates along $\hat{x}$, while the other along $\hat{z}$ and they overlap on the atomic sample at the center. It is important to mention that two different geometries (crossed-dipole and single-beam) of the optical trap were used in order to perform the experiment on the spin-dipole oscillation and polarizability at ∼zero and finite temperature. For simplicity here I will only report the description of the two geometries, without specifying for which project a specific configuration was used. The motivation of the choices leading to the different configurations as well as all the parameters which characterize the optical traps will be reported in the chapter devoted to the discussion of the main results.

Crossed-dipole trap   The crossed dipole geometry is characterized by the presence of both the IR beams which cross each other almost orthogonally. The horizontal beam is initially collimated by means of a 50 mm focal length lens and is then focused on the atoms via a 400 mm focal length lens. The waist w_0 can be estimated knowing the mode field diameter (MFD) of the fiber and the lenses along the beam's path. The estimated waist of the horizontal beam is equal to ∼ 50 μm. The Rayleigh range z_R associated to this beam can be calculated using the formula $z_R = \pi w_0^2 / \lambda$ [105] that, in this case, corresponds to $z_R = 7$ mm.

The vertical beam is collimated by means of to a 30 mm focal length lens, being then focused on the atomic cloud via a 500 mm focal length lens. The

---

5 A dichroic mirror filter which transmits infrared light while reflecting visible light.

waist of the vertical beam is estimated to be ~ 100 μm ($z_R = 30$ mm). A sketched of the crossed-dipole configuration is reported in Fig.2.9.
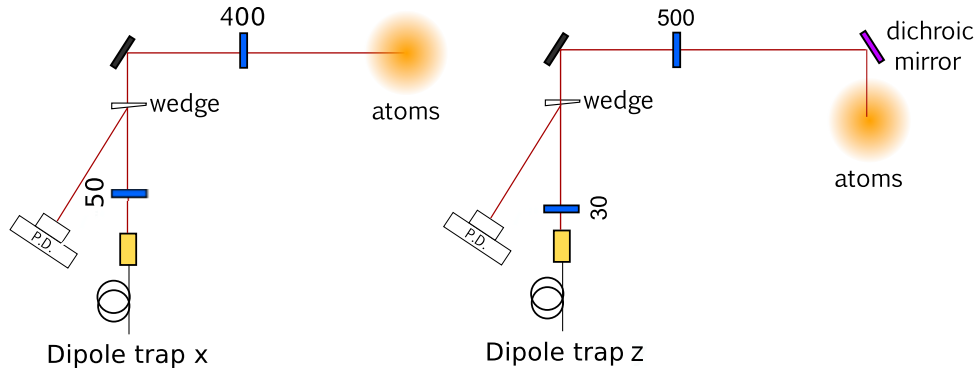

Figure 2.9: Scheme of the IR beams out-coming the fibers for the cross-dipole trap configuration. The x beam is collimated with a 50 mm focal length lens and it reaches the horizontal atoms plane thanks to a series of mirrors tilted at 45° along the three main directions. Lastly it is focused on the sodium cloud by a 400 mm focal length lens. The z beam is collimated with a 30 mm focal length lens and it reaches the vertical atoms plane thanks to several couples of mirrors tilted at 45° along the Cartesian axes to finally be focused on the sodium cloud by a 500 mm focal length lens.

Single-beam trap

The single-beam trap geometry was realized using only the horizontal beam, whose configuration was changed with respect to the one used for the crossed-dipole trap, in order to guarantee an effective harmonic trapping also at temperature of the order of a few μK. In particular the IR beam was tightly focused in order to reach a deep trapping potential. To tighten the waist of the beam a series of two telescopes was realized. Firstly the diverging IR beam out-coming the fiber is collimated by a 50 mm focal length lens, then it passes trough a -100 and a 175 mm focal length lenses. These particular focal lengths were chosen in order to minimize the waist of the beam on the atoms, taking into account for the constrains of the optical setup. Finally the beam is focused on the atomic cloud thanks to a 200 mm focal length lens obtaining a waist of ~ 10 μm ($z_R = 295$ μm). Due to the small waist of the IR beam the 200 mm lens was placed on a micro-metrical translational slit which permits to overlap the beam's waist and the MT center with high precision and reliability. A sketched of the single-beam configuration is reported in Fig.2.10.

Laser power stabilization and control

To guarantee the reliability of the experiment performed in the optical dipole trap, the power of the IR light must be stabilized. Thus a feedback loop, as the sketched in Fig.2.11, was used to stabilize the laser power at the output of the fibers.

The feedback loop is composed by

- an AOM which is the actuator of the power control;

- a photodiode which sends a fraction of the light to the stabilization system;

- a proportional–integral–derivative controller (PID);
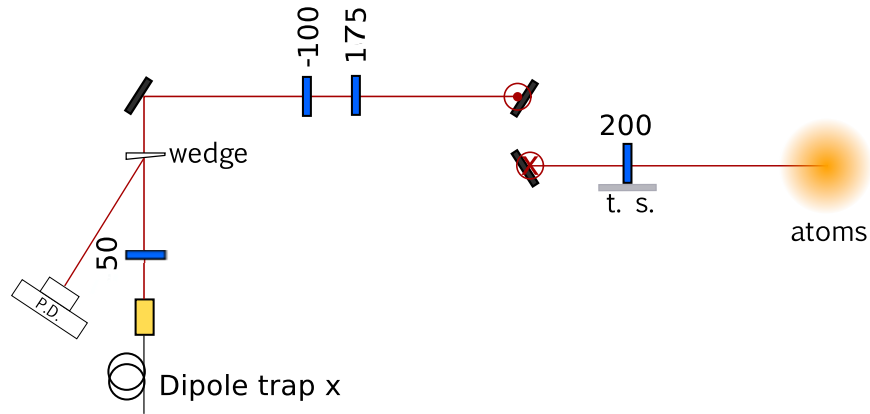
- a DAC to impose the setpoint;

Figure 2.10: Scheme of the IR beams out-coming the fibers for the single-beam trap configuration. The *x* beam is collimated with a 50 mm focal length lens and it reaches the horizontal atoms plane thanks to a series of mirrors tilted at 45° along the Cartesian axes. Lastly it is focused on the sodium cloud by a 200 mm focal length lens mounted on a micro-metric translational slit. Along the beam path two extra lenses were placed in order to obtain a smaller waist on the atoms. The focal lengths of these lenses are -100 mm and 175 mm respectively.
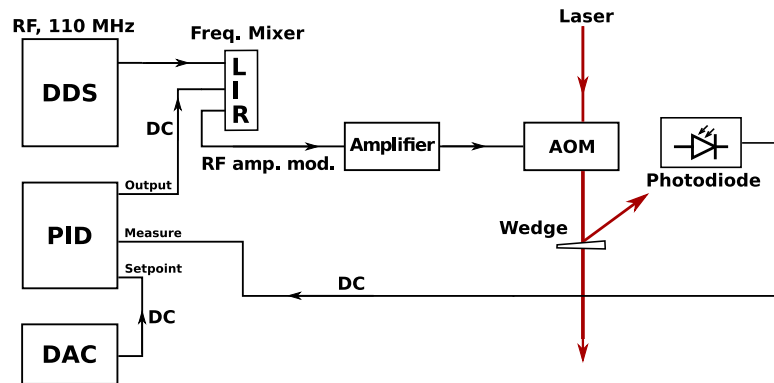

Figure 2.11: Sketch of the feedback loop built to guarantee a reliable control of the power of the IR beams used to optically trap the atoms.

- a DDS, a frequency mixer and an amplifier which are used to generate the RF signal to drive the AOM.

The power control of the IR light is performed acting on the AOMs located before the fiber input, as illustrated in Fig.2.11. Acting on the RF signal sent to the AOM of each IR arm it is possible, in fact, to tune the power of the diffracted light which is coupled to the fiber. A portion of this diffracted light is collected by a photo-diode thanks to a wedge (*Thorlabs PS810*) reflecting about 0.25 % of the incident light. This signal is sent to a PID controller whose setpoint is externally controlled via the experiment computer. The output of the PID is then sent to a radio-frequency mixer (*Mini Circuits ZWL-1-1+*) where it is combined with a RF signal produced by a DDS. The resulting signal is then sent to an amplifier (*Mini Circuits ZHL-1-2WX-S*) delivering a maximum output 30 dBm. This amplified signal, whose intensity is set by the PID, is sent to the AOM in order to continuously stabilize the power of its diffracted light. It is important to note that this power control

system can work efficiently only if operating below the saturation threshold of the amplifier. For this reason the output of the DDS was attenuated in order to prevent entering the saturated regime.

The PID control and stabilization was performed using a proportional and integrated circuit. The time and gain constants were chosen via *Ziegler-Nichols closed loop method* [106].

2.5 ELECTRONIC AND CONTROL SYSTEM

Instrumental control

To carry out experiments with the apparatus described in the previous sections, a precise control on many instruments is necessary. The experimental sequence to produce BECs, starting from laser cooling to final imaging, must be executed with a timing precision better than 1 μs. The sequence must be repeated with great reliability.

To reach this precision, most of the laboratory instruments are controlled with a unified digital control system. This system is based on a field programmable gate array (*FPGA*) which was firstly developed by Marco Prevedelli.

The central FPGA (*XILINX SPARTAN XC3S250E*) receives the temporal list of instructions to execute from a control software, through a parallel custom bus (*USB*) connection. Each instruction included in the list has a target slave board, which is unequivocally identified by its address. The instructions are written on a 24-bit bus with a time-resolution of 100 ns and with a maximal instruction rate of 2.5 MHz.

To perform the experimental sequence almost 50 digital lines, 30 RF and 15 analog sources are needed. All these signals are provided by three different kinds of slave boards.

The boards

- *DIGITAL BOARDS* Each digital board can provide 16 independent Transistor–Transistor Logic (TTL) channels. These TTLs are mainly used to set the configuration of the magnetic field during all the steps of the experimental sequence, since they are used to open or close the IGBTs and the relay switches of the electric circuit. In addition the TTLs are used to trigger the imaging acquisition sequence, as well as other actions of the experimental list and to activate the mechanical shutters for the optical beams.

- *ANALOG BOARDS* These boards contain two 16-bit digital-to-analog (DAC) converter. The output voltage can be referred to ground or remain floating. These boards are mainly used to control the power supplies which provide the current to the electric circuit. DACs can also be used in cases when a continuous control of the IGBTs is required.

- *RF BOARDS* The programmable RF signals are generated using Direct-Digital-Synthesizer (DDS) chips (*ANALOG DEVICES AD9958*) based on a 10-bit DAC. Each RF board can provide two different output channels. Each of these channels has an independent setting for frequency, amplitude and phase. The frequency can range from 200 kHz to 140 MHz with a 32-bit resolution, while the amplitude can reach a maximal power of +13 dBm. A microcontroller (*PIC18F2550*) reads the required parameters from a LookUp Table (LUT) and programs them

on the DDS. The RF signal is then amplified and sent to the AOMs or to other components. (see sec.3.1).

It is important to note that, increasing the length of the bus which connects all the boards, can produce problems in the reliability of the experimental procedure. This is mainly due to communication problems among all the electronic parts of the system, since a long bus can lead to noise pick-up and to increasing capacity of the bus. To overcome this issue the control system was divided in two parts, each of them equipped with an independent FPGA and a bus located in different areas of the laboratory. In this way the cable connection is shorter, guaranteeing the reliable transmission of all the signals.

This separation of the control system introduces a time jitter of many tens of ms between the two parts controlled by independent FPGAs when triggerd via the USB port. This can be a major problem in atomic physics experiments, where μs resolution is required. This problem was solved using a single triggering signal for both the FPGA able to trigger their startup only when the USB communication is entirely completed. This solution, performed with a *ARDUINO*, guarantees a synchronization at the level of 100 ns even in this distributed control configuration. More recently this solution was enhanced in order to have both the FPGAs triggered in phase with the 50 Hz of the electricity network. This precaution helps to suppress noise sources arising from 50 Hz power grid.

The software used to control the experimental sequence and devices was recently written in *PYTHON 2.7* and it offers the possibility to perform automatic iterations of parametrized procedures over different experimental variables. For more details on the software consult [107].

2.6 IMAGING SYSTEM

To probe the properties of the investigated system an imaging apparatus is fundamental. Among all the imaging techniques that can be used [99], the absorption imaging is the one implemented in our laboratories.

This technique is based on the absorption of resonant light by the sample that, in case of inhomogeneous system, is well described by the generalized Lambert-Beer's law:

$$I(y,z) = I_0(y,z)e^{-\mathcal{O}(y,z)}. \tag{2.4}$$

Here I and I_0 represent the transmitted and incident light respectively, while $\mathcal{O}$ is the optical density integrated along the axial imaging direction

$$\mathcal{O}(y,z) = \sigma \int n(x,y,z)dx, \tag{2.5}$$

where $n(x,y,z)$ is the density distribution of the sample and σ is the absorption cross-section. The integral 2.5 is known as column density.

The absorption cross-section in the case of a two-level system is given by [108]:

$$\sigma = \sigma_0 \frac{1}{1 + \frac{4\delta^2}{\Gamma^2} + \frac{I}{I_{sat}}}, \tag{2.6}$$

where δ is the detuning with respect to the two-level resonance, σ_0 is the on-resonance cross-section, Γ is the natural line width (FWHM) of the D_2 transition, I_{sat} is the saturation intensity of the transition and I is the intensity of the incident light. The two-level approximation is valid only for σ-polarized light on the $|F = 2, m_F = 2\rangle \rightarrow |F' = 3, m_F = 3\rangle$ transition. Given the saturation intensity for the cooling closed transition, that is equal to 6.26 mWcm^{-2}, σ_0 can be written as $3\lambda^2/2\pi$. Moreover, considering that during the imaging $I \ll I_{sat}$ the total absorption cross section can be rewritten as:

$$\sigma = \frac{3\lambda^2}{2\pi} \frac{1}{1 + \frac{4\delta^2}{\Gamma^2}}. \tag{2.7}$$

It is thus possible to measure the optical, hence spatial, density by means of the experimental measurement of the transmitted intensity profile using the relation:

$$\mathcal{O}(y,z) = -\log \frac{I(y,z)}{I_0(y,z)}. \tag{2.8}$$

The optical density of a trapped gas is obtained by integration along the imaging direction of the spatial density distribution of the atomic cloud that, in the case of a thermal gas in an anisotropic harmonic potential, is given by:

Optical density of a thermal gas

$$n(x,y,z) = \frac{N}{(2\pi)^{3/2}\sigma_x\sigma_y\sigma_z}e^{-\frac{(x-x_0)^2}{2\sigma_x^2} - \frac{(y-y_0)^2}{2\sigma_y^2} - \frac{(z-z_0)^2}{2\sigma_z^2}}. \tag{2.9}$$

In equation 2.9, (x_0, y_0, z_0) indicates the position of the minimum of the trapping potential, $\sigma_{x,y,z}$ are the widths of the Gaussian along the three main directions and N is the total number of atoms. The integration along the imaging direction only gives a constant contribution equals to $\sqrt{2\pi}\sigma_x$ leading to the expression:

$$\mathcal{O}(y,z) = \frac{3\lambda^2}{2\pi} \frac{1}{(1 + \frac{4\delta^2}{\Gamma^2})} \frac{N}{2\pi\sigma_y\sigma_z}e^{-\frac{(y-y_0)^2}{2\sigma_y^2} - \frac{(z-z_0)^2}{2\sigma_z^2}} \tag{2.10}$$

for the optical density.
The experimental 2D profile of the optical density can be fitted obtaining information about the sample.

When the optical depth exceeds 2-3, it is helpful to detune the probing light in order to reduce the optical density of the imaged cloud below the saturation threshold so that information about the total number of atoms can be extracted.
A relevant feature concerning the thermal cloud is the possibility to obtain information on the temperature of the sample as well as on its size. In particular the temperature estimation was used to perform the measurement of the spin-dipole oscillation and polarizability at finite temperature (see 3.5). Information about the temperature can be extrapolated looking in time-of-flight at the free expansion of the sample. In this case the evolution of the

cloud, which can still be fitted by a Gaussian profile, is governed by the relation:

$$\sigma_{x,y,x}^2(t_{exp}) = \sigma_{0\,x,y,x}^2 + \frac{k_B T}{m} t_{exp}^2,$$ (2.11)

where $\sqrt{\frac{k_B T}{m}}$ is the thermal velocity. Taking images at different expansion time and plotting the quadratic size of the cloud as a function of t_{exp}^2 it is thus possible to extrapolate the temperature of the sample via a linear fit.

Fit of the BEC   In the extremely low temperature regime $T \sim 0$ the fitting function to obtain information about the Bose–Einstein condensate is different. In this case the in-situ kinetic energy of the particles can be neglected, being much lower than the interaction energy. In such a limit, labeled as the Thomas–Fermi approximation, the in-situ spatial distribution in a harmonic trap can be ascribed to an inverted parabola. Integrating the inverted parabola profile along the imaging direction and multiplying it by the absorption cross-section we obtain the optical density of a BEC:

$$\mathcal{O}_{TF}(y,z) = \frac{\sigma_0 5N}{2\pi \mathcal{R}_y \mathcal{R}_z} \left[max \left(1 - \frac{y^2}{\mathcal{R}_y^2} - \frac{z^2}{\mathcal{R}_z^2}, 0 \right) \right]^{3/2}$$ (2.12)

The optical density 2.12 can be fitted on the experimental data to determine the number of atoms N and the Thomas–Fermi radii.

Bimodal distribution   When a partially condensed sample is created ($0 < T < T_c$), the correct fitting function for time-of-flight (TOF) imaging is bimodal to take into account both the thermal fraction (fitted by a Gaussian) and the condensate (fitted by an inverted parabola).

Fitting software   The software used to fit the experimental images is written by G.Thalhammer using Python language and it bases on Levenberg–Marquardt non-linear least-squares algorithm. The data processing is quite fast, taking only a few seconds to fit a 300 pixel×300 pixel data matrix. This software already included many different fitting functions and was recently upgraded to adapt to our needs (see Subs.4.2.3).

Imaging setup   The imaging setup is composed of three different paths of the probing light so that the atomic cloud can be imaged from the three main axial directions x,y and z. At the end of each probing light arms a CCD camera is placed. The beam is split in three and propagate along independent paths thanks to a series of polarizing beam-splitter cubes. The beams used to image the cloud from $\hat{x}$ is focused on the camera using an achromatic doublet with a focal length equals to 150 mm, while the imaging along $\hat{z}$ is performed focusing the beam on the camera by means of a singlet spherical lens with a focal length equals to 100 mm. The probe beam used to image the BEC from the y direction is focused on the camera using a telescope with magnification ~ 1.3, being composed by an achromatic 75 mm and a spherical 100 mm lens. In front of all the cameras a dichroic mirror is placed in order to prevent any damage due to the IR light of the optical trap.

The camera used to image the atoms is a *Stingray F-201*, whose CCD sensor is 1624 pixel × 1234 pixel with a pixel size of 4.4 μm ×4.4 μm. Thus the effective chip size is $\sim$ 7.1 mm × 5.4 mm and the dynamic range of the analog-to-digital converter (ADC) is 14 bit. A FireWire IEEE 1394b-800 Mbits^{-1} serial

port connects the camera to a computer, while the camera trigger is driven by a TTL signal controlled by the experiment computer. The data aquired by the camera are converted in a RAW file through a LabView interface.

The imaging sequence is composed of four images each of them having an integration time of 200 μs.

Imaging procedure

- The first image is used to record the shadow produced on the probe beam by the atomic sample giving the quantity I(x,y) of Eq.2.4. 50 μs after the beginning of the integration time the probe beam is switched on and for 100 μs. In addition to the probe beam the repumper one is also present during the acquisition so that atoms in F=1 ground-state are optically pumped to the bright F=2 one. The repumper is turned on 50 μs before the beginning of the acquisition and it is switched off at the end of it.

- 100 ms after the acquisition of the first image, once that all atoms are gone, the second image is taken in the same light condition as the first one (repumper light included).

- The third and fourth images are taken to set the background signal, being indeed taken without any resonant light. The background signal is subtracted to the previous images to have again in terms of signal-to-noise ratio.

The optical density of Eq.2.4 is obtained from

$$\mathcal{O}(y,z) = -\log\left(\frac{I_1(y,z) - I_3(y,z)}{I_2(y,z) - I_4(y,z)}\right), \tag{2.13}$$

so that all the relevant information about the atomic cloud can be extracted.

3

EXPERIMENTAL METHODS

Contents

Mixtures of ultracold atoms offer rich opportunities to study novel physical phenomena from an experimental and theoretical point of view. Thanks to the variety of atomic species and the additional degrees of freedom related to the hyperfine structure, several mixtures can be crated. In this chapter I will describe the procedures used to create and to manipulate the specific mixture I studied during my PhD. In particular I will present all the steps to reach the quantum degeneracy are described, the optical trap loading and all the steps necessary to obtain and manipulate a binary mixture.

3.1 FROM LASER COOLING TO BEC

Usually, BECs are obtained in conservative traps (like magnetic or far-off resonant trap) where evaporative cooling can be performed. This is because in magneto-optical traps, the lowest achievable temperature is limited by photon re-absorption. However, the loading in conservative traps requires a pre-cooling stage.
In our experiment, BEC is created in a 4 mK deep magnetic trap and, after its creation, it could be transfer to a dipole-optical trap.
The sample is pre-cooled by means of a DS-MOT and an optical molasses stages, which permit to reach temperature of about 40 μK. The need to reach temperature lower than the magnetic trap depth is because the transfer from the MOT to the MT could heat the sample.

The first step of the pre-cooling stage consists in a dark-spot magneto-optical-trap (DS-MOT) which is loaded directly from the 2D-MOT [90] stage described in 2.1. The DS-MOT is based on the use of spatially selective re-pumping light which does not act on the atoms at the center of the MOT cloud. In this way it is possible to reach a higher density than in the case

Dark-Spot MOT

of standard MOT because the re-absorption of scattered photons is reduced [100].

The DS-MOT consists of six beams which counter-propagate in pairs along three orthogonal directions. Each beam has a diameter of 2.5 cm and has circular polarization with the proper helicity for magneto-optical-trapping [84]. The repumper light passes trough a glass plate which has an 8 mm diameter black spot at its center. The shadow of this circle is imaged on the atomic cloud plane. In this way the trapped atoms are efficiently repumped with the exception of the ones occupying the central region which remain in the dark state $|F = 1\rangle$.

In addition to the optical beams, a magnetic 3D-quadrupole field with vertical axis is present and, along its axis, the gradient is $\sim$12 G/cm. The zero of the magnetic field is centered in the region where the three counter-propagating beams intersect. The coils used to generate this field are the same used for the magnetic trap configuration, as described in section 2.3.

The DS-MOT loading procedure can last from few seconds up to 20 s (or more) depending on the total desired number of atoms in the BEC and on the loading conditions. In ordinary working condition the phase-space-density (PSD)[1] obtained at the end of the DS-MOT stage is of the order of 10^{-6}.

Optical molasses   After the DS-MOT stage an all-optical cooling sequence is performed [109]. This optical molasses phase lasts 5 ms, during which both the frequency and the intensity of the cooling and the repumping light are changed in order to minimize the temperature without losses. During this stage the quadrupole field is switched off and all the environmental residual magnetic fields are compensated using the shim coils[2]. At the end of the molasses stage the phase-space-density was estimated to be $\sim 10^{-5}$.

Gray molasses   During my PhD a gray molasses cooling stage was implemented for the first time for sodium atoms [110]. This stage relies on D_1 light of sodium (see A), which is blue detuned with respect to the $|F = 2\rangle \rightarrow |F' = 2\rangle$ transition. This radiation is independently produced and frequency stabilized. The use of D_1 light permits to suppress off-resonance excitations on the blue side of the hyperfine manifold of interest. The cooling of atomic sodium in gray molasses proved to be suitable to reduce the temperature by a factor of four from about 40 to $10\,\mu$K. The highest value of the PSD obtained by means of the gray molasses is 10^{-4}, which corresponds to a tenfold increase with respect to the standard red-detuned optical molasses. This enhancement of the PSD will play a key role in the cooling procedure of Fis$\hbar$ (see Introduction). Even though the efficiency of the gray molasses sequence was proved, it turned out that the implementation of this stage during the experimental sequence is not applicable. As a matter of fact, the loading from the gray molasses in ordinary magnetic IP trap as it is done routinely, presents a poor mode-matching, canceling out the benefits produced by the gray molasses. In addition the loading procedure requires to operate the IGBTs in the linear regime at high current, exposing the magnetic trap circuit to frequent failures.

---

1 The central PSD of the sample is PSD = $n_P \lambda_T^3$ where n_P is the spatial in-situ density at the center of the Gaussian distribution, while λ_T is the de Broglie wavelength.

2 Actually the magnetic fields used to compensate the residual environmental ones are turned on during the whole experimental sequence

At the end of the pre-cooling stage all the atoms are loaded into the Ioffe– *Magnetic trapping*
Pritchard magnetic trap. The magnetic field configuration required for this
stage is turned on abruptly at maximum strength (I_{ht} regime described in
Sec.2.3). Since the mode-matching between the atomic cloud and the trap is
not optimal, the sample heats up. To improve the mode-matching the load-
ing into the magnetic trap should be performed in presence of a high bias
field. Nevertheless this would increase the gravitational sag, making a dis-
placement of the trap necessary to match the MOT center. Fortunately, the
high stability of the trap permits to obtain an efficient long evaporation so
that matched loading of the trap is not strictly required.

As anticipated before, the use of conservative traps permits to reach the *RF-induced evaporation*
quantum degeneracy by means of RF evaporation. The radio-frequency in-
duced evaporation [111] is the most efficient cooling procedure at this stage.
This cooling mechanism relies on the removal of atoms of higher energy
from the the thermal distribution. More in detail, the whole process can
be interpreted as an iteration of two steps: the removal of atoms from the
tails of the thermal distribution and the consequent re-thermalization of
the remaining atoms. Since the removed atoms carry out an energy larger
than the mean energy, the atomic cloud thermalizes at a lower tempera-
ture. The removal process is performed using radio-frequency transition
which promotes atoms from a trapped state to an untrapped one. In par-
ticular, the trappable state is $|F = 1, m_F = -1\rangle$, while the untrappable one is
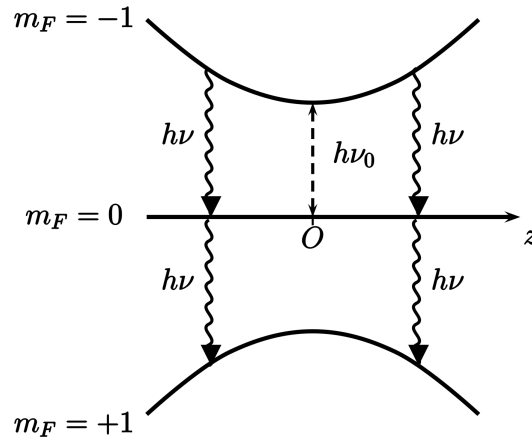$|F = 1, m_F = 1\rangle$.

Figure 3.1: Sketch of the radio-frequency induced evaporation taken from [112].
Atoms in $|1, -1\rangle$ having an energy larger than $h(\nu - \nu_0)$ couple to the RF radiation
and are ejected by the magnetic trap.

Following the scheme of Fig.3.1, the two Zeeman states $|F = 1, m_F = -1\rangle$
and $|F = 1, m_F = 0\rangle$ are RF coupled where the magnetic potential is equal to
the RF photon energy $h\nu$, which fixes the evaporation threshold. Thus, the
spin-flip mechanism is induced only for atoms having an energy larger than
$h(\nu - \nu_0)$, where $h\nu_0$ corresponds to the trap bottom. Ramping down the fre-
quency of the RF radiation, it is possible to force the evaporation threshold
down to the quantum degeneracy regime.

Since during the evaporation the density of the sample increases, at some
point three-body recombination will start to limit the evaporation efficiency

[99]. To avoid this loss mechanism, a decompression of the trap from I_{ht} through the regime I_t or I_s (see Sec.2.3) is necessary. In this way the confinement of the atoms becomes shallower, hence the density of the sample is reduced. During and after the decompression, which lasts 600 ms, the evaporation keeps transferring atoms to the untrapped state.

Overall the evaporation ramp lasts about 26 s and creates an ultracold degenerate gas of 3 millions atoms, within a relatively short duty cycle.

3.2 OPTICAL TRAP LOADING

Once the BEC was created in the magnetic trap using the procedure described in the previous section, the sample is transfer in the dipole optical trap (see Fig.3.2). Right after the end of the RF evaporation ramp, the dipole optical trap is turned on in two seconds. The sample is thus transfer from the MT trap to the DT one, since the former has a much lower trapping potential energy. After the dipole trap was completely turned on, the magnetic trap is switched off by decreasing the current flowing in the coils to zero. This procedure can last up to two seconds.
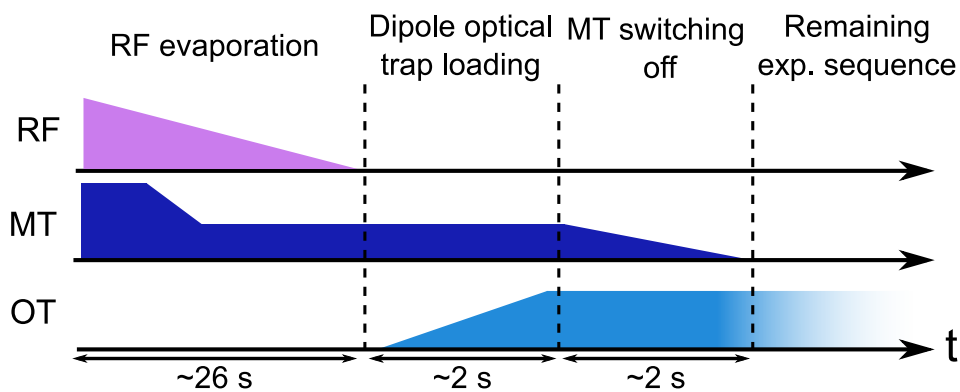

Figure 3.2: Scheme of the experimental procedure used transfer the sample from the magnetic to the dipole optical trap. All the steps are shown as columns, whose duration is reported at their bottom. From top to bottom each row correspond to RF radiation used to perform the evaporation cooling, the magnetic field of the MT and the intensity of the dipole optical trap.

To have an efficient transfer to the optical dipole trap, the two traps must align perfectly. The aligning procedures used to reach this precision are described below. Firstly I will report on the procedure used to align the crossed-dipole trap, then I will describe the method used to align the single-beam optical trap.

The first step, which is common for both procedures, is to take a reference picture of the BEC in the magnetic trap, making sure to have the BEC as small as possible. The reference picture of BEC position in the magnetic trap is usually taken along the x and the z direction using resonant light.

Crossed-dipole trap alignment Once the reference position is identified, the horizontal beam of the optical trap is aligned proceeding as follows: firstly the power of the dipole x beam is set to zero using the power control circuit described in sec.2.4. Actually, even if the power is set to zero, a small leak of few mW of IR light is

present. This light leak is imaged on the horizontal camera. The position of the horizontal IR beam is steered on the atomic sample position. Once that the horizontal beam is aligned on the atoms, a similar procedure is used to align the vertical beam. A subsequent fine adjustment of the dipole trap position is performed directly looking at the number of atoms loaded in the optical.

A similar alignment procedure was used for the case of a single-beam optical trap. To avoid sloshing of atoms, the waist of the horizontal beam should perfectly match the minima of the MT. Thus, once that the magnetic and optical traps overlap, the fine alignment procedure requires to minimize the size of the in-situ optical trap. Referring to the IR power leak just mentioned it is important to notice that it can be suppressed installing a second RF mixer on the circuit described in Sec.3.5 in order to effectively switch off the dipole trap.

Single-beam trap alignment

3.3 MIXTURE CREATION

As already pointed out in this thesis the great variety of atomic species and hyperfine/Zeeman states offer the opportunity to create many mixtures all having different properties. One of the most important distinctive property is the miscibility of the mixture (see Sec.1.2), which is related to interaction effect among particles. As already explained in Sec.1.2, our sodium mixture is particular suitable to investigate both spin dynamics and static spin properties of the system, which are difficult to study in other systems. In the following the steps necessary to create this mixture are explained in detail. Firstly it is important to remind that we create the single-component BEC in the magnetic trap, as described in Sec.3.1. Thus, at the beginning, all the atoms occupying the magnetically trappable $|F = 1, m_F = -1\rangle$ state. From the magnetic trap, the BEC is loaded in the far-detuned optical dipole trap using the procedure described in the previous section. The polarization of the sample is maintained during the transfer. Once that all the atoms were efficiently transferred to the dipole trap, we create the mixture $|F = 1, m_F = \pm1\rangle$ with two steps:

- a Landau-Zener (LZ) transfer which permits to efficiently transfer all the atoms from $|F = 1, m_F = -1\rangle$ to $|F = 1, m_F = 0\rangle$;

- a $\pi/2$ Rabi pulse which creates a balanced superposition of $|F = 1, m_F = -1\rangle$ and $|F = 1, m_F = +1\rangle$ Zeeman sublevels.

A pair of atoms $|1, +1\rangle$ and $|1, -1\rangle$ can relax in two $|1, 0\rangle$ atoms dissipating energy. To prevent this phenomenon, we increase the energy of $|1, 0\rangle$ via blue-detuned μ-wave dressing with $|2, 0\rangle$ in order to energetically forbid the relaxation process.

All these steps are the same for both the crossed-dipole and the single-beam configurations which were used to study the properties of the mixture.

In general, it is possible to obtain a binary mixture also by exploiting a two-photon process based on optical or RF transition. Raman coupling [113] require radiation in the visible part of the spectra and are particularly suitable to split and accelerate condensates, as well as to induce spin-orbit
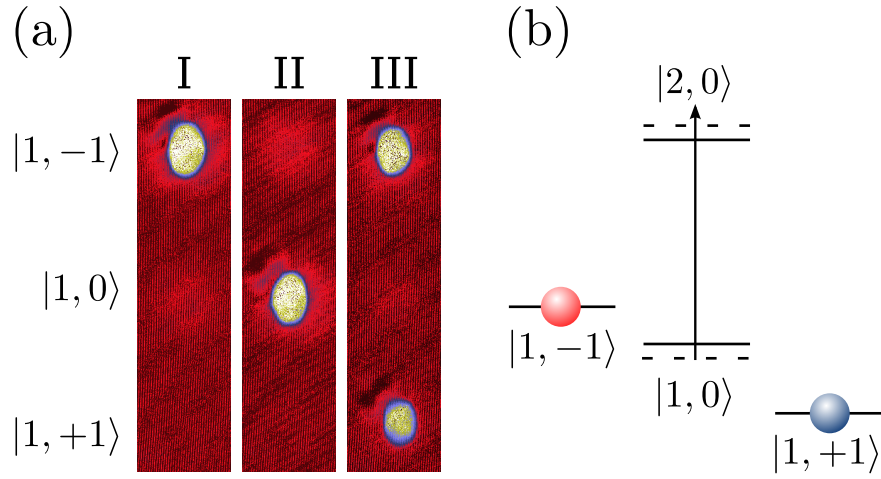
Figure 3.3: (a) Optical density distribution occupying the three Zeeman state at different stage of the experimental procedure. From the left (I) the polarized sample in $|F = 1, m_F = -1\rangle$, (II) the transfer in $|F = 1, m_F = 0\rangle$ due to LZ transition and the mixture created after the Rabi pulse. (b) Sketch of the dressing of the $|F = 1, m_F = 0\rangle$ state.

coupling among the different spin components of the mixture [4]. However, they present the disadvantage of being rather difficult to implement since an additional laser beam path is required. RF two-photon transition is a similar technique which can be used to transfer atoms in different Zeeman (in case of RF signal) or hyperfine (in case of μ-wave) states [20]. This procedure is particularly helpful when it is not possible to change the magnetic field in order to perform a Landau-Zener transfer.

3.3.1 Landau–Zener transfer

LZ mechanism

The first stage to reach a stable miscible mixture of sodium atoms in $|F = 1\rangle$ consists in a Landau-Zener transfer [114], which permits to transfer essentially all atoms from $|F = 1, m_F = -1\rangle$ to $|F = 1, m_F = 0\rangle$.
This transfer works when dealing with a two-level system which depends on an external parameter q and, for a given value of q, the two levels of the system have the same energy, *i.e.*, they cross each other being thus degenerate. This degeneracy can be broken if a coupling between the two levels is added as outlined in Fig.3.4

In our case the q parameter corresponds to the magnetic field $\vec{B}$, which is externally applied using the electro magnets described in sec. 2.3. The value at which the two levels cross is $|\vec{B}| = 0$. At low magnetic field, the Zeeman splitting is the same for both $|F = 1, m_F = -1\rangle$ and $|F = 1, m_F = +1\rangle$ with respect to $|F = 1, m_F = 0\rangle$. Thus, to obtain an effective two-level system the quadratic Zeeman effect [95] must be exploited in order to prevent population transfer in $|1, +1\rangle$.

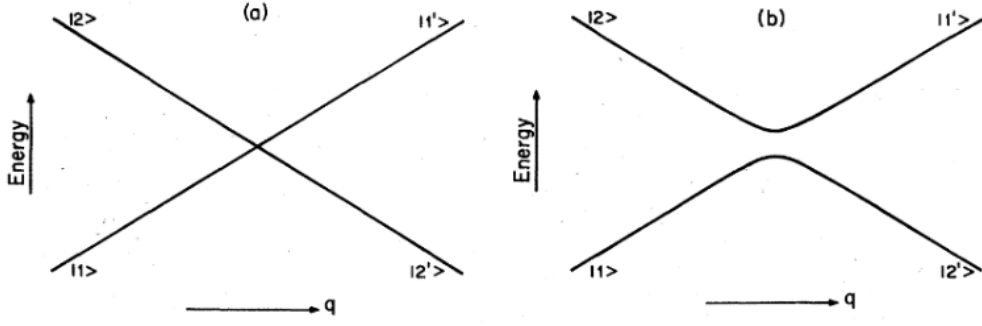*Frequency choice*   When dealing with the ground-state of the D transition, the energy splitting

Figure 3.4: Two-level energies as a function of the parameter q. Unperturbed energies scheme (a) and perturbed system (b) which presents an avoided crossing. Image taken from [114].

among the Zeeman levels in presence of an intermediate magnetic field is given by the Breit–Rabi formula [115, 91]:

$$E_{m_F} = -\frac{\Delta E_{hf}}{2(2I+1)} + g_i \mu_B m B \pm \frac{\Delta E_{hf}}{2}\sqrt{1 + \frac{4mx}{2I+1} + x^2} \tag{3.1}$$

where $x = (g_J - g_I)\mu_B B / \Delta E_{hf}$, ΔE_{hf} is the hyperfine splitting, $m = m_I \pm m_J = m_I \pm 1/2$ (where the $\pm$ sign is the same as in Eq.3.1), I is the nuclear spin, μ_B is the Bohr magneton, g_J and g_I are the electronic and nuclear Landé g-factors respectively.

Usually the magnetic field used is of a few G so that the splitting among energetic levels is well described by the linear Zeeman effect, corresponding to the limit of $x \ll 1$ in Eq.3.1. To take into account higher corrections we have to expand the formula up to the second order in x that, neglecting then g_I with respect to g_J, gives a contribution proportional to

$$E_{qZ} \propto \frac{-\Delta E_{hf}}{2}\left(\frac{mx}{2} + \frac{x^2}{2}\right) + \frac{-\Delta E_{hf}}{16}m^2 x^2. \tag{3.2}$$

A reasonable value of the magnetic field $\vec{B}$ which enables us to obtain an effective two-level system is $|\vec{B}| \sim 100$ G giving a splitting between the two spin states $|F = 1, m_F = -1\rangle$ and $|F = 1, m_F = 0\rangle$ equal to $\sim$65 MHz [3].

Applying a sufficiently strong magnetic field, thus, it is possible to energetically shift the $|F = 1, m_F = -1\rangle$ level by a quantity higher than the one associates with $|F = 1, m_F = +1\rangle$ state. Eventually, at $|\vec{B}| \sim 100$ G, $\Delta E_{0\to-1} \sim 65$ MHz, while $\Delta E_{0\to+1} \sim 60$ MHz. In this way, the system composed by $|F = 1, m_F = -1, 0\rangle$ can be dealt as an effective two-level system. The coupling between the two levels is given by a radio-frequency signal irradiated on the atoms thanks to a circular antenna placed above the quartz cell. The frequency value is chosen to be equal to the difference in energy between the two levels at a specific value of the magnetic field.

The probability to transfer all the atoms from the level $|F = 1, m_F = -1\rangle$ (level $|1\rangle$ of Fig.3.4) to the level $|F = 1, m_F = 0\rangle$ (level $|0\rangle$ of Fig.3.4) is given by:

$$P_{10} = 1 - exp\left(-2\pi\frac{\hbar|\Omega_{10}|^2}{dE/dt}\right) \tag{3.3}$$

---

[3] Sometimes the energy splitting is indicated in frequency unit, meaning that $\Delta E/h = \Delta\nu$

where Ω_{10} is the Rabi coupling between the two states, $dE/dt=dE/d\vec{B}\cdot d\vec{B}/dt$ is the slew rate and $\hbar$ is the Planck constant. Since we are interested in maximizing this probability, we want $\hbar|\Omega_{10}|^2$ to be large compared to dE/dt or, equivalently, we want that dE/dt is slow compared to the Rabi timescale. In this case the avoided crossing is said to be traversed adiabatically.

LZ sequence   The Landau–Zener procedure starts with the setting of the coil circuit in order to guarantee a homogeneous magnetic field along $\hat{x}$. Once the circuit is ready, the magnetic field is turned to about 100 G (which correspond to a current of 108 A). The final value of $\vec{B}$ is reached in 250 ms in the case of the crossed-dipole geometry and in 2 s in the case of the single-beam geometry. In this way, $t \ll 2\pi/\omega_x$, being ω_x the slowest timescales of the system. The value of $\vec{B}$ is kept fixed for a few ms, while a near-to-resonance radio-frequency signal at 65 MHz is turned on. This signal is generated using a DDS and it is irradiated on the atoms using the circular antenna already used for the evaporative cooling. At high field the quantization axis is aligned along $\hat{x}$ and, considering that the antenna in the near field irradiates an orthogonal wave aligned along $\hat{z}$, the RF magnetic field can be ideally decomposed in the sum of a σ^+ and σ^- polarization components. Since, at this stage, all the atoms are collected in $|1,-1\rangle$ only the σ^+ component interacts. When the RF signal is on, the magnetic field is increased by about 1 G (current at 109 A) in 25 ms, in order to cross the resonance condition and to have an adiabatic transition to the $|F=1, m_F=0\rangle$ state, being the Rabi frequency of the order of $\sim 10^4$. The timing of this ramp is the same for both the trap configurations since the Rabi frequency does not depend on the trapping configuration. Once the transfer is done, the RF signal is turned off and the magnetic field is switched off using the same timing of the starting ramp. A scheme of the timing sequence of the Landau–Zener transfer is reported in Fig.3.5.

Finally it is important to mention that, to prevent any depolarization mechanism during the tuning off and on of the magnetic field (especially when the value of the current was set close to zero) and additional weak magnetic field of a few G was applied along the y direction.

Spin-cleaning   The efficiency of this transfer was proven to be high, ranging from 100% and 70% depending on the working conditions. Nevertheless, even if the transfer has a good efficiency, it is possible to have a small residual population in the $|m_F = -1\rangle$ spin state. In such situations, it is possible to apply a sufficiently strong magnetic gradient along the axial direction (using the pinch coil) able to wipe out the undesired residual population. This gradient applies a force on the atoms as explained in sec.3.6.
Since, at the first order, the $|F=1, m_F=0\rangle$ state is not sensitive to magnetic field, this magnetic gradient will affect only the $|F=1, m_F=\pm1\rangle$ states. We refer to this procedure as spin cleaning and, even if we have implemented it, we rarely had the necessity to use it.

3.3.2 Rabi coupling

The second step to create the mixture $|F=1, m_F=\pm1\rangle$ is the $\pi/2$ Rabi pulse. It consists in the transfer of half of the population occupying the
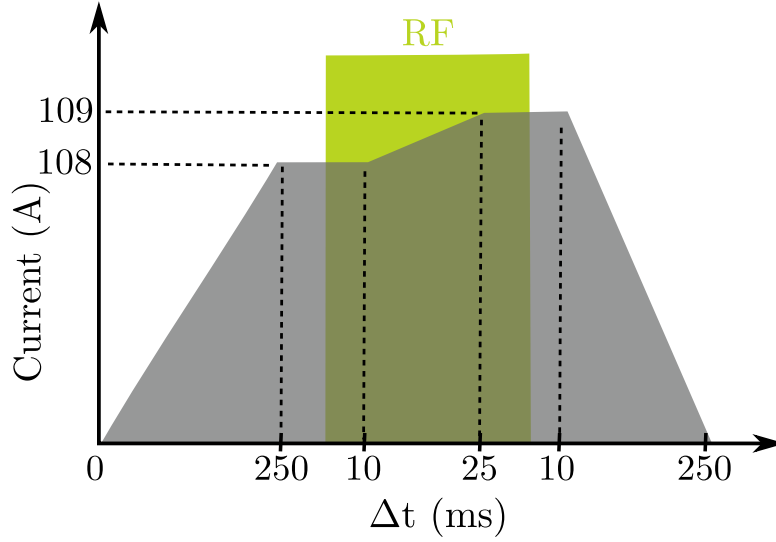
Figure 3.5: Timing scheme of the Landau–Zener transition used during the experimental sequence in the crossed-dipole trap. The timing used in the case of the single-beam trap configuration only differs for the steeper ramps of the magnetic field, which last 2 s. In gray the value of the current applied to generate a homogeneous magnetic field is drawn, while in green is indicated the intensity of the radio-frequency signal used to couple the two spin states.

$|F = 1, m_F = 0\rangle$ Zeeman state to $|F = 1, m_F = +1\rangle$ and the other half to $|F = 1, m_F = -1\rangle$l. To do this it is necessary to realize a symmetric separation between the two extreme Zeeman states. This condition can be restored introducing a magnetic field $|\vec{B}|$ small enough to neglect the quadratic Zeeman effect. Referring to the quadratic Zeeman contribution formula 3.2, a good approximation for a negligible quadratic term is an energy of the order of 100 Hz. We use a magnetic field of about 0.5 G, which permits to neglect the quadratic Zeeman effect. This field is produced using the fine-tuning coils aligned along the x direction only after that the magnetic field was carefully compensated along all three directions (see Sec. 3.4). Proceeding in this way we are sure that the quantization axis experienced by atoms is along $\hat{x}$.

At this stage we apply a Rabi pulse with a RF signal to transfer the atoms from $|F = 1, m_F = 0\rangle$ to $|F = 1, m_F = \pm 1\rangle$. The resonance condition is at 400 kHz. Similar to 3.3.1, the radiation is produced by a circular antenna aligned along $\hat{y}$ which creates σ^+ and σ^- polarized fields wuth equal intensity.

The time evolution of the level populations when the symmetric system is on resonance and the initial state is $|F = 1, m_F = 0\rangle$ is given by:

$$P_0 = \frac{1}{2}(1 + cos2\Omega t) \quad P_1 = \frac{1}{4}(1 - cos2\Omega t) \quad P_{-1} = \frac{1}{4}(1 - cos2\Omega t) \quad (3.4)$$

where Ω is the Rabi frequency defined as

$$\Omega = \frac{\langle m_F = 0|\mu \cdot B|m_F \pm 1\rangle}{\hbar} \quad (3.5)$$

and μ is the magnetic dipole operator. Since we are interested in the creation of an equally popolutated mixture, we need to apply a $\pi/2$-pulse.

Eq.3.4 is obtained considering a three-level system, that in our case is the spin-1 system where the splitting among the three internal states is the same, being given by linear Zeeman effect. If at t=0 a radio-frequency signal aligned along a direction i orthogonal to the quantization axis is applied, the radiation field couples to the spin operator $\hat{S}_i$. In the rotating-wave approximation, after a time t, the initial spinor wavefunction $|\Psi\rangle$ will be rotated by an angle $\theta = \Omega t$ along the i-direction so that

$$|\Psi'\rangle = e^{-i\theta\hat{S}_i}|\Psi\rangle \tag{3.6}$$

where the rotation operator is given by

$$e^{-i\theta\hat{S}_i} = \begin{pmatrix} \frac{1-cos\theta}{2} & \frac{sin\theta}{\sqrt{2}} & \frac{1-cos\theta}{2} \\ -\frac{sin\theta}{\sqrt{2}} & cos\theta & \frac{sin\theta}{\sqrt{2}} \\ \frac{1-cos\theta}{2} & -\frac{sin\theta}{\sqrt{2}} & \frac{1-cos\theta}{2} \end{pmatrix}. \tag{3.7}$$

If the initial condition of the system is such that all the atoms occupy the $m_F = 0$ sublevel, after an evolution time t, the system has evolved in accordance with Eq.3.4.

The $\pi/2$-pulse corresponds to a pulse of 14 μs (Fig.3.6), which corresponds to a Rabi frequency of about 18 kHz. Unfortunately a clear signal
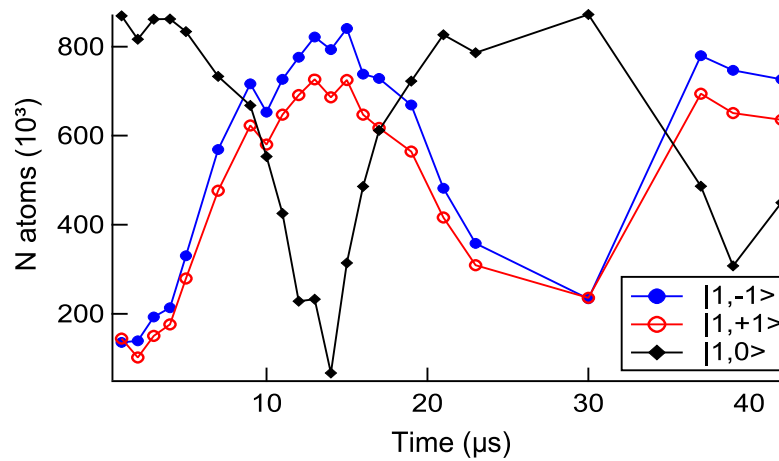

Figure 3.6: Rabi oscillation for the crossed-dipole configuration. The population of the three Zeman sublevels are reported in black ($|1,0\rangle$), blue ($|1,-1\rangle$) and red ($|1,+1\rangle$). The line among the experimental point is only a guide for the eyes, since due to saturation problem a trustworthy fit can not be performed.

of the Rabi oscillation is not easy to take. In fact, in Stern–Gerlach imaging (see 3.6) of all spin states, the OD density of the sample is so high that is is not possible to obtain a reliable estimate of the number of atoms occupying each state. In any case an in-phase evolution of the two external spin states was clearly observed in different cases suggesting that the mixture created is equally populated. Note that the population imbalance of $|1,-1\rangle$ and $|1,+1\rangle$ results from an imaging artifact (see 3.6 or [116]).
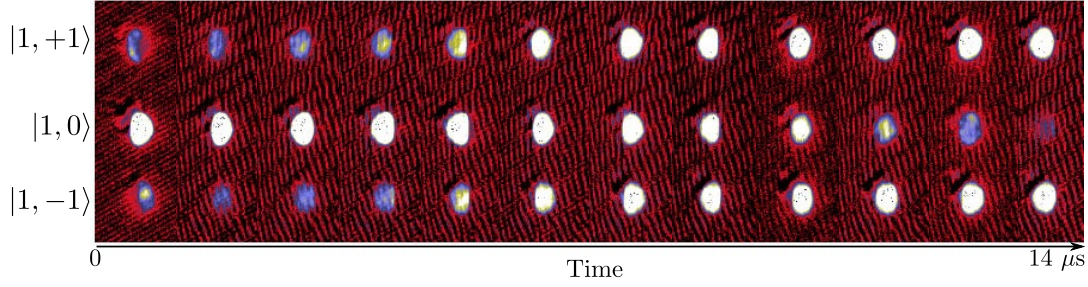
Figure 3.7: Optical densities of the three Zeeman sublevels observed during the first fourth of period of the Rabi oscillation. The uppermost distribution corresponds to the $|1,-1\rangle$ state, the central to $|1,-1\rangle$ and the lowest to $|1,+1\rangle$. As clearly visible the optical density often exceeds the saturation threshold.

3.3.3 μ-wave dressing

Once the mixture $|1,\pm1\rangle$ is created, we need to stabilize it against inelastic collisions. In fact, by looking at Eq.3.2, it is possible to verify that

$$|1,+1\rangle + |1,-1\rangle \rightarrow 2 \times |1,0\rangle + h\nu \qquad (3.8)$$

This process can be suppressed by increasing the energy of $|F=1, m_F=0\rangle$ via μ-wave dressing. The dressing of a state relies on the interaction of the system with an external radiation which is able to energetically shift the levels position depending on the incident radiation. The shift in energy is given by [95]:

Dressed state

$$\Delta E_{light} = \hbar \frac{\Omega^2}{4\delta} \qquad (3.9)$$

where Ω is the Rabi frequency of the induced coupling and δ is the detuning of the incident field. Depending on the detuning the shift can be either positive (blue-detuning) or negative (red-detuning).
For our purpose, a blue-detuned radiation was used to couple the $|F=1, m_F=0\rangle \longrightarrow |F=2, m_F=0\rangle$ transition, whose resonance is at 1.771626 GHz. The μ-wave used to stabilize the system has a detuning of $2\pi \times +14$ kHz with respect to the resonance transition and an estimated Rabi frequency of about $2\pi \times 5$ kHz, producing a shift of about 500 Hz. Regarding the Rabi frequency, it is important to underline that a direct measurement of it was never computed. However, an estimate of the Rabi frequency of the $|F=1, m_F=0\rangle \longrightarrow |F=2, m_F=0\rangle$ transition can be obtained from the measured Rabi frequency of the $|F=1, m_F=-1\rangle \longrightarrow |F=2, m_F=-2\rangle$ transition [117] performed with the same antenna and taking into account for Clebsh-Gordan coefficient and intensity correction. In addition, it is important to note that at $T \neq 0$ thermal particles could populate the $|F=1, m_F=0\rangle$ state, leading to loss mechanism as discussed in Ch.4.
The μ-wave is irradiated to the atomic distribution thanks to a hook-shaped antenna which produces a π- polarized pulse. The signal is turned on immediately after the end of the Rabi $\pi/2$-pulse and it is kept on up to the end of the experimental sequence.
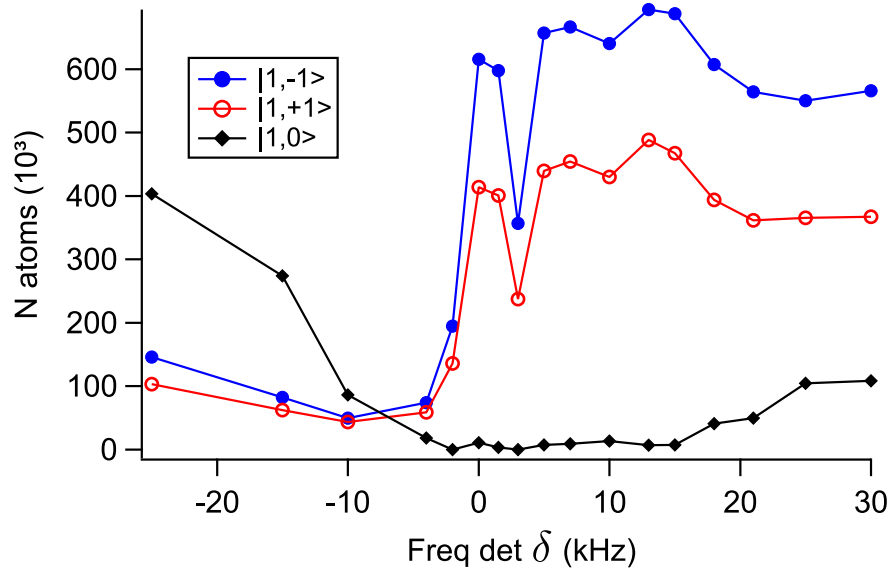
Figure 3.8: Population of the three Zeeman states 300 ms later the Rabi pulse as function of the detuning of the μ-wave applied. The power of the μ-wave is fixed at zero dBm.

The final detuning and the power of the μ-wave signal was chosen after scanning independently these two parameters, in order to study their effect on the population of the Zeeman states. In Fig.3.8 the population of three levels as function of the μ-wave detuning is reported.

In Fig.3.9 a scheme of the experimental sequence used to create and study the binary mixture is reported.

3.4 CALIBRATION OF THE MAGNETIC FIELD $\vec{B}$

Experiments with quantum mixture require a precise knowledge of the magnetic field, both to avoid zero crossing of $\vec{B}$ and to define the quantization axis experienced by atoms.

One strategy to calibrate the magnetic field is to use Zeeman spectroscopy. This technique is based on the Zeeman shift of the atomic levels due to an applied magnetic field. These shifts can be determined inducing a resonance between two Zeeman states by means of a RF coupling. These resonances are studied as a function of an applied magnetic field and permit to determine the residual environmental magnetic field $\vec{B}_r$. If the applied magnetic field is oriented along one specific direction, it is possible to separately determine the value of each component of $\vec{B}_r$.

The calibration of $\vec{B}_r$ is been realized using a RF signal at 400 kHz and a magnetic field produced independently along $\hat{x}, \hat{y}$ and $\hat{z}$. These magnetic fields are created using the shim coils, directly acting on the current flow.

A detail description of the procedure used is described in the following.
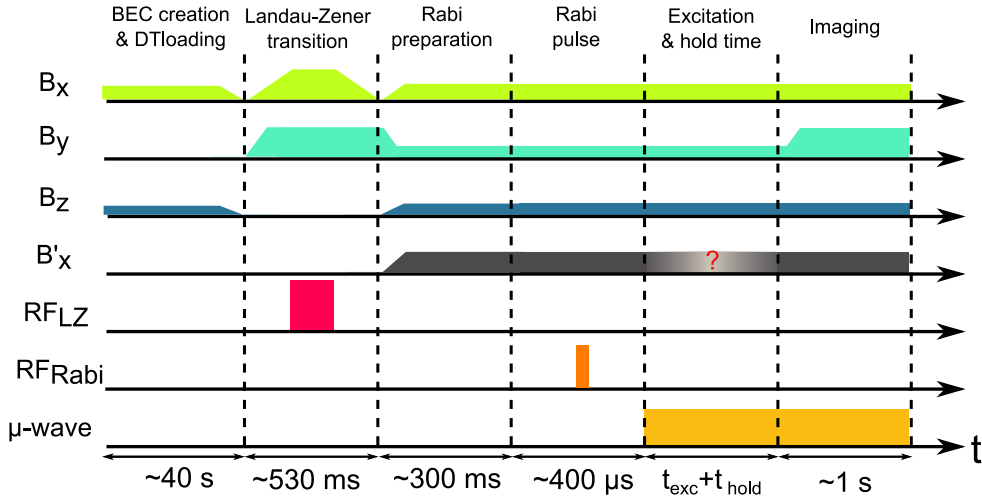
Figure 3.9: Scheme of the experimental procedure used to create, excite and image the binary mixture after the BEC creation. All the steps are shown as columns, whose duration is reported at their bottom. Each rows correspond to a different parameter which was changed during the sequence. From top to bottom magnetic gradient along x, y and z direction, magnetic gradient along $\hat{x}$, RF at 65 MHz, RF at 400 kHz and blue-detuned μ-wave at 1.771 GHz. The value of the magnetic gradient during the phase "Excitation and hold time" depends on the investigated quantity during the experiment (see Ch.4).

3.4.1 B_y

To calibrate the magnetic field we fixed the RF signal frequency and amplitude and we varied the value of one component of the magnetic field in order to transfer some atoms from the $|F = 1, m_F = 0\rangle$ state to $|F = 1, m_F = \pm 1\rangle$. To change the modulus of the magnetic field along one specific direction, we varied the current flowing in the shim coils oriented along the that specific axis.

As first step we searched for the Rabi resonance at 400 kHz keeping fixed the value of the current flowing in the y (I_y) and z (I_z) shim coils, while varying the current flowing in the x (I_x) shim coils. The same measurements were repeated for different value of (I_y) and the resulting curves are reported in Fig.3.10, where the number of atoms transferred in the $|F = 1, m_F = -1\rangle$ state is indicated as a function of I_x.

As visible from the figure, the resonance was found at $I_x \sim 600$ mA of current flowing in the x-shim coils. Changing the value of the current I_y, *i.e.*, the value of B_{r_y}, the amplitude of the resonance was changing as well. For this first characterization the Rabi pulse was 12 μs long.
Once that the condition to observe the Rabi resonance was found, we performed a more precise characterization of the zero of the y component of the residual magnetic field. More in detail the current I_x was kept fixed at 600 mA while the value of I_y was changed. This study was realized for two different conditions of the Rabi pulse and the results are reported in Fig.3.11 where the number of atoms in $|1, -1\rangle$ is indicated as a function of I_y.

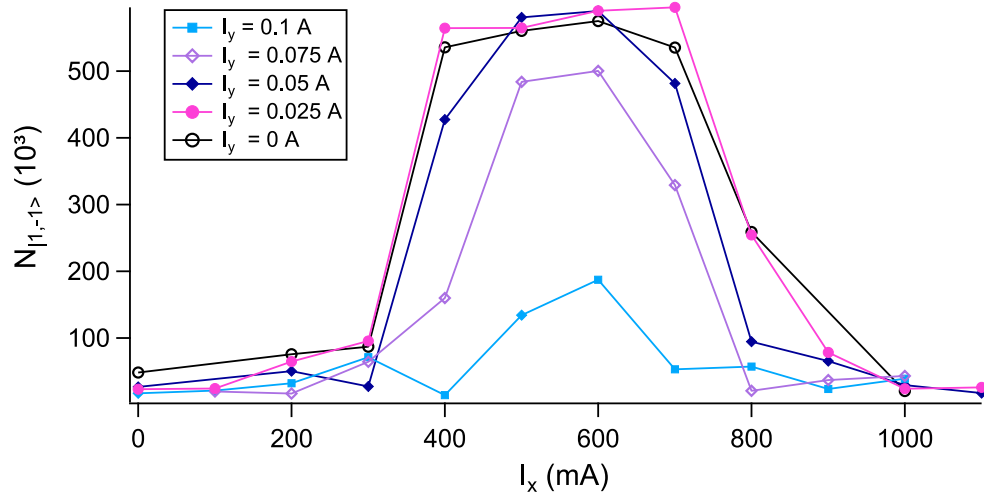From the narrower curve of Fig.3.11 the resonance current $I_y = 23(1)$ mA was found.

Figure 3.10: Population occupying the $|F = 1, m_F = -1\rangle$ state as function of I_x for different I_y. The number of atoms was estimated after a Rabi pulse of 12 μs. The value of I_z was fixed to the one used during the 3D-MOT stage.

3.4.2 B_x

Once that the y component of $\vec{B}_r$ was canceled out, the remaining field can be written, in first approximation, as:

$$B_r = \sqrt{B_{r_x}^2 + B_{r_z}^2} \tag{3.10}$$

and thus for any value of B_{r_x} two resonance values of B_{r_z} exist and *vice versa*. We have searched for those resonances keeping the value of I_z fixed and scanning I_x. This procedure was repeated for different value of I_z and the results are reported in Fig.3.12, where the population in $|1, -1\rangle$ as a function of I_x is reported for different value of I_z.

As visible from Fig.3.12, the two resonances are clearly distinguishable when the residual magnetic field is not well compensated. Approaching the zero of the residual magnetic field the two resonance peaks get closer, since they end up in a unique large resonance distribution. This is compatible with Eq.3.10 and a more clear understanding of it can be obtained looking at Fig.3.13.

Focusing our attention only on one pair of resonance peaks it is possible to estimate the value at which $B_{r_x} = 0$ that will corresponds to half the distance between the two peaks' centers as indicated in Fig.3.14. Proceeding in this way the current value at which the x component of the residual magnetic field is compensated was estimated being I_x=560(2) mA.

3.4.3 B_z

Finally, to calibrate the residual magnetic field along the z direction a procedure equal to the one used for B_{r_x} was followed. Fixing the value of I_x at 1050 mA the two resonances was found and their relative distance was estimated to be I_z=0.43(1) mA.

Thanks to this calibration we were able to cancel out the residual magnetic field with a precision of the order of 1 mG. However, we know that the
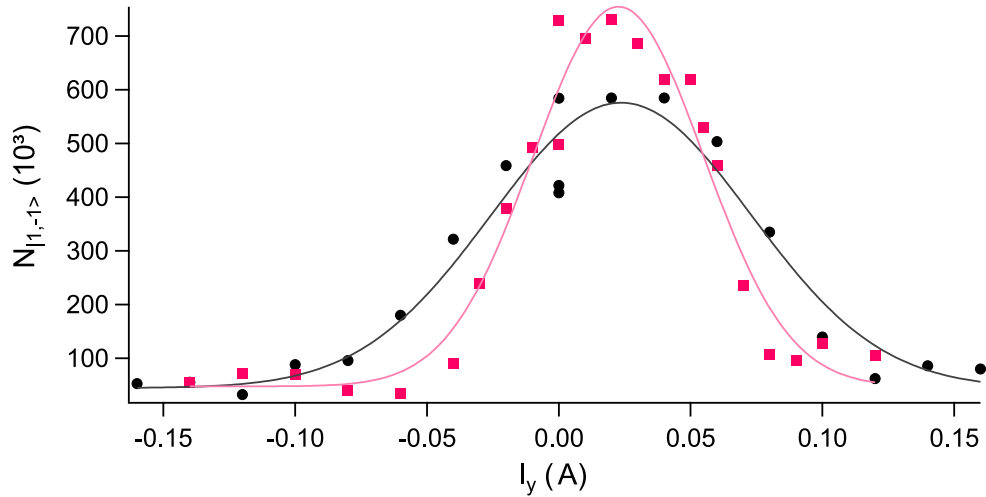
Figure 3.11: Population occupying the $|F = 1, m_F = -1\rangle$ state as function of I_y for different Rabi pulse conditions. The pink squares correspond to a 50 μs long pulse, while the black circles correspond to a 12 μs long pulse at a higher power. The solid lines are the Gaussian fits giving the estimation for I_x such that $B_{r_x} = 0$. The value of I_z was fixed to the one used during the 3D-MOT stage, while I_x was equal to 600 mA.

external magnetic field has fluctuations of the level of a few mG from shot to shot.

3.5 HEATING PROCEDURE

One of the goal of my PhD research is to study the thermal effects on the spin-dipole oscillation and polarizability and, since we transfer from the magnetic trap to the optical one at $T \ll T_C$, a controllable heating procedure of the ultracold atomic sample is necessary. The most popular heating procedure is the parametric heating, but other mechanism can be exploited in order to warm up the sample. For example it is possible to use resonant light to transfer an energy of the order of the recoil energy $E_r = p^2/2m$ (m the atom's mass and p the photon's momentum) to the atoms. The drawback of this procedure is that it leads to losses at high spatial densities due to light-assisted collisions. For this reason we use the parametric heating [118, 119], by modulating the optical potential power on resonance with the radial quadrupole mode of the atomic cloud.

For a thermal sample, where interactions can be neglected, the frequency at which the heating mechanism is induced is twice the trapping frequency [74]. The resonance can be observed either in the increase of the atomic cloud size or in the atomic losses resulting from the evaporation of the heated atoms. When dealing with BECs, the resonance frequency is modified to account for the effect of interactions. In particular, when the Thomas–Fermi approximation is valid and $\omega_x \ll \omega_\perp$, the resonance frequency is expected to be $\sqrt{5}$ bigger than the radial harmonic oscillator [42].

The first heating attempts were realized modulating the power of one of the dipole beams directly using the experimental control software, but soon
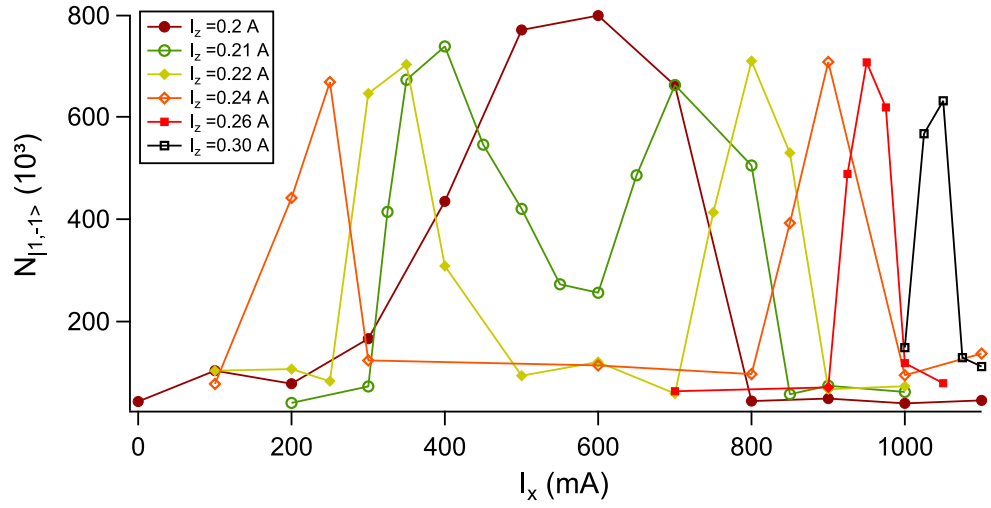
Heating procedure

Figure 3.12: Population occupying the $|F = 1, m_F = -1\rangle$ state as a function of I_x for different I_z. The number of atoms was estimated after a Rabi pulse of 50 μs. The value of I_y was fixed at 23 mA, corresponding to $B_{r_y} = 0$.
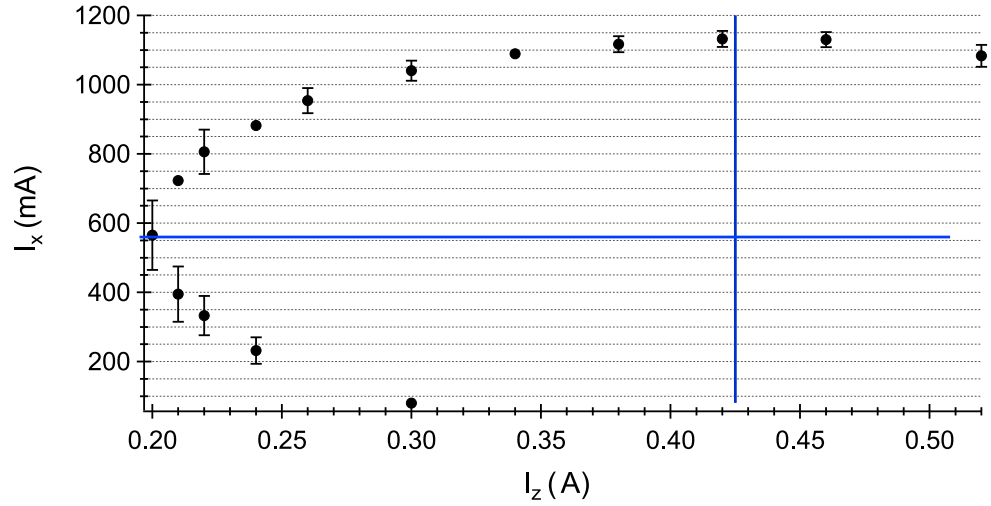

Figure 3.13: Measured I_x resonant values for given I_z. I_y is fixed at 23 mA. The blue solid lines represent the value of current at which B_{r_x} and B_{r_z} are equal to 0.

we implemented a more reliable procedure. The new heating procedure relies on an electrical circuit (Fig.3.15) able to sum the DC power signal of the dipole trap and a sinusoidal modulation created using an arbitrary function generator (*AGILENT 33250A*).

The heating is controlled by varying the number of modulation cycles at fixed amplitude ($10 - 20\%$ of the trap depth) and frequency (twice the trapping radial frequency). The parametric heating procedure is applied on the polarized sample once the BEC was completely transferred to the OT and the MT was turned off. At the end of the heating sequence the mixture of BECs was created using the method described in the previous sections. This procedure enabled us to control the BEC temperature without losing atoms as visible for Fig.3.16. The temperature of the sample after parametric heating was estimated using the relation 2.11, where four different TOF were considered.
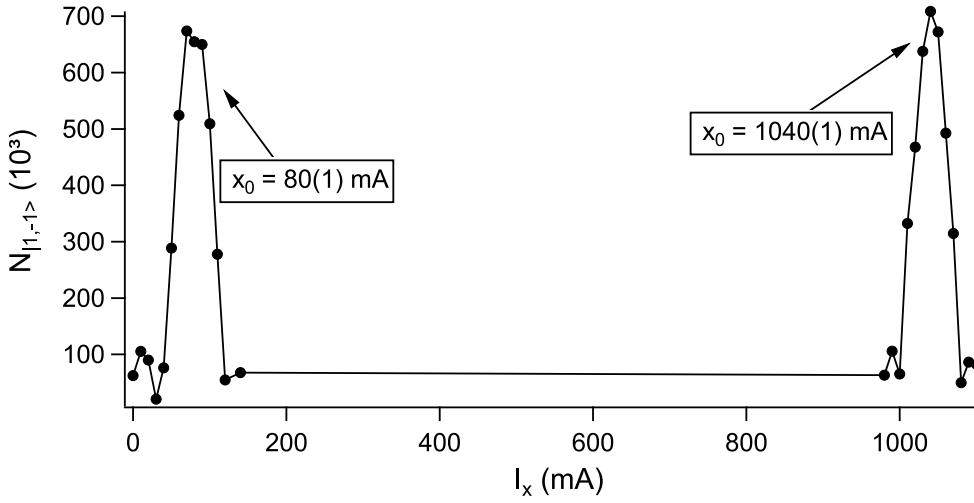
Figure 3.14: Rabi resonances as a function of I_x at fixed I_y (23 mA) and I_z (300 mA) . The number of atoms was estimated after a Rabi pulse of 50 μs. Computing the relative current separation between the two resonances it is possible to estimate the condition satisfying $B_{r_x} = 0$.

The condensed fraction as a function of temperature was estimated and compared with the theoretical predictions. As visible in Fig.3.17, our experimental data are in good agreement with the models, especially with the one taking into account the role of interactions in HF approximation (see Ch.1 or [120]). Thus, thanks to this heating procedure, we were able to heat the sample from $T \sim 0$ up to T_C and to study the role of temperature in the spin dynamics of our mixture.

3.6 STERN−GERLACH IMAGING

Resonant absorption imaging technique is a very powerful tool in ultra cold atomic experiments, but it does not directly discern among the different spin states. For this purpose an imaging technique based on the Stern–Gerlach (SG) separation [121] or dispersive imaging [46] can be used. Here we use SG separation.

As introduced in Sec.2.3, the interaction energy of an atom with an external magnetic field can be written as

$$E = \vec{\mu} \cdot \vec{B} = \mu_B g_F \vec{F} \cdot \vec{B} = \mu_B g_F m_F |B| \tag{3.11}$$

where μ_B is the Bohr magneton, g_F is the Landè factor, $\vec{F}$ is the total atomic angular momentum, m_F defines the internal spin state of the atoms and $\vec{B}$ is the external magnetic field. When the magnetic field is not homogeneous the atom experiences a spin-dependent force equals to

$$F = -\mu_B g_F m_F \nabla |B|. \tag{3.12}$$

In this way atoms occupying different Zeeman sublevels experience a differential force, which, in the case of $|1, \pm 1\rangle$, accelerates the two states in opposite direction. Once that the atomic populations are completely separated the standard absorption imaging technique can be used to probe the
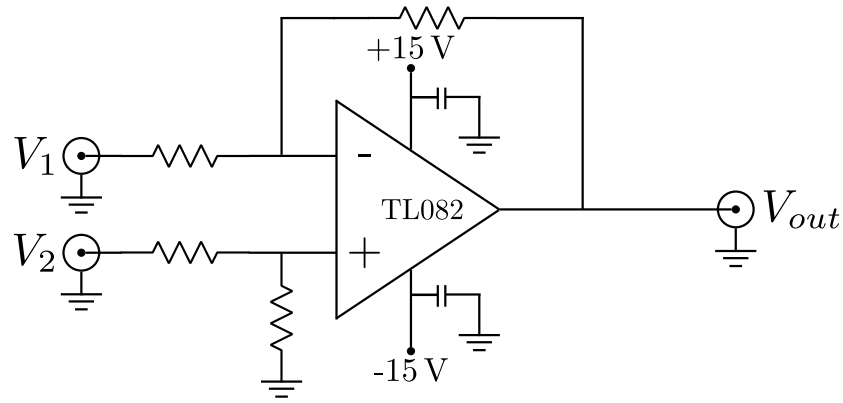
Figure 3.15: Sum circuit built to add a sinusoidal modulation to the DC dipole power. All the resistances are 1 MΩ, while the capacitances are 0.1 μF. The V_1 signal corresponds to the dipole power level set by the experiment control, while V_2 is related to the sinusoidal modulation.

clouds.

In the experimental sequence the Stern–Gerlach imaging is realized by applying a magnetic field gradient along the vertical direction by means of the lower coil of the 3D quadrupole. The resulting force pushes the atoms occupying the $|F = 1, m_F = -1\rangle$ state upward while the atoms occupying the $|F = 1, m_F = +1\rangle$ are pushed downward. To completely separate the different distributions, TOF of the order of 10 ms (or less) are usually necessary with a magnetic field gradient of the order of 8 G/cm. In the following all the imaging are acquired with SG separation.

Even if during the experimental sequence an equally populated mixture is created, the optical density of the two spin states appears to be not the same. This is due mainly to the optical pumping effect that occurs during the imaging procedure [116]. To avoid this inhomogeneous signals a calibration of the scattering cross-sections of the different spin states [122] could be performed in order to take into account the multi-level structure of the sample as well as optical effects. However, this optical pumping effect do not affect the proper estimation of the center-of-mass position of the density distribution of the cloud.
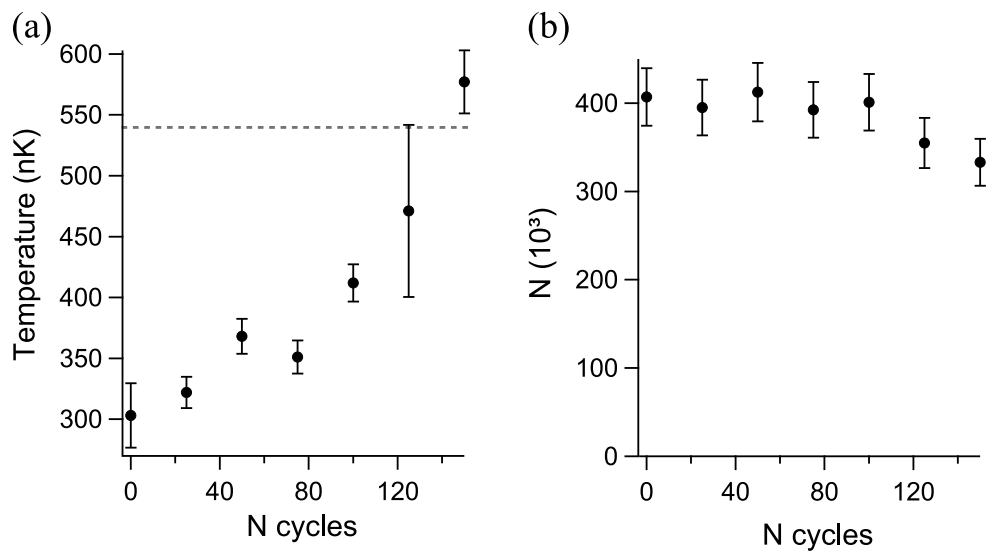
Figure 3.16: Effect of the parametric heating on a fully polarized BEC occupying the $|F = 1, m_F = -1\rangle$ state a the crossed-dipole configuration. Temperature of the atomic distribution (a) and total number of atoms (b) as a function of the number of cycles used to modulate the optical trap. In (a) the value of the critical temperature T_C is indicated as the gray dashed line. Each point of the graph is the mean value of five different data sets.
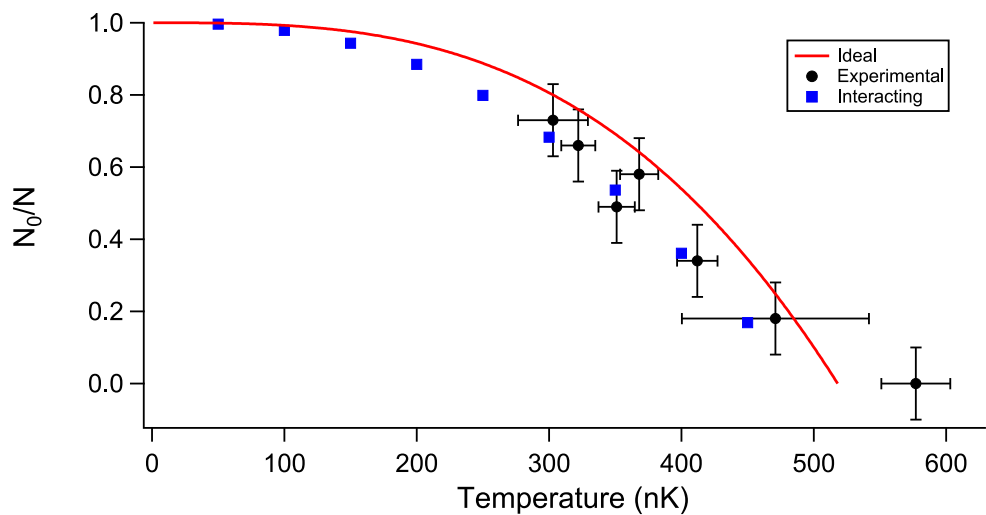

Figure 3.17: Fraction of condensed atoms as function of the temperature experimentally observed (black circles) or calculated for an ideal (red curve) and interacting (blue squares) gas.

4 | EXPERIMENTAL RESULTS

Contents

The realization of BEC mixtures has opened new research opportunities, since different kind of systems can be realized (see Sec.1.2). For example, these systems can be investigated to study phase separation phenomena and associated multicomponent dynamics [123, 25, 124, 125] and, in the case of counterflowing superfluids, they can be used to generate dark-bright solitons [26, 50]. Other relevant research topics concern the spin dynamics and the spin properties of these systems. In fact, in the last years, spin-superuidity and spin-transport phenomena [12] have attracted an increasing interest in the scientific community, especially in the field of condensed matter physics.

Here I report on the measurement of spin properties in BECs like the spin-dipole (SD) oscillation frequency and polarizability (both at $T \sim 0$ and $T \neq 0$), as well as on the study of spin superfluidity at finite temperature.

This chapter is divided in two sections, the first devoted to the $T \sim 0$ case and the second to the finite temperature one. Both sections start with the description of the trap configuration used to perform the experiment. Then I described the main results concerning the SD polarizability and SD oscillation, that in the finite temperature case were studied both in the collisionless and collisional regime.

4.1 TWO–COMPONENT BEC AT T∼ 0

In the following the main results which concern a binary mixture at T close to 0 are reported. The main novelty of this work regards the direct measurement of the static SD polarizability and SD oscillation frequency.

The measurement of these quantities was possible since the sodium mixture used is miscible and not subject to buoyancy (see Sec.1.2). The experiment was performed in a crossed-dipole optical trap, whose configuration is described in Sec.2.4.

4.1.1 Trap frequencies

Trap frequencies

The first step in most of the experiments realized with ultracold atoms is the measurement of the trapping frequencies, useful to estimate the relevant timescales of the system and the BEC parameters. One way to measure the trapping frequencies is studying the center-of-mass (COM) oscillation of the whole atomic distribution. In our case the trapping frequencies are expected to be of the order of a few kHz at maximum and a direct measurement of them was performed exciting the COM oscillation.

Once that the BEC was transferred into the optical-dipole trap, the COM oscillation was excited applying a magnetic field gradient. This gradient, which was applied either along the axial (x) or vertical (z) direction, acts as a force on the fully polarized trapped sample occupying the $|F = 1, m_F = -1\rangle = |\downarrow\rangle$ state, the modulus and the direction of the force being determined by equation 3.12.
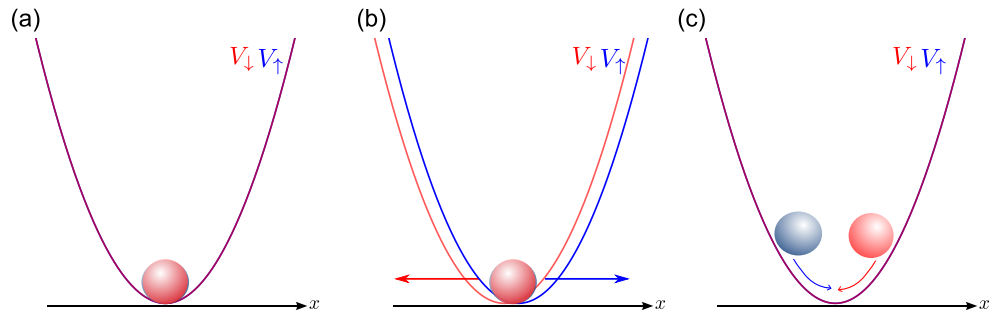

Figure 4.1: Sketch of the trap and atomic configuration before (a), during (b) and after (c) the application of a magnetic field gradient pulse. The potential minima are displaced only when a magnetic gradient is applied (b).

To create the gradient along the axial direction the pinch coil was used, while the levitation configuration was used for creating the gradient along the vertical direction (see Sec.2.3). Exciting the cloud along the axial direction enables us to measure the axial frequency, while the vertical excitation gives access to both radial frequencies, probably because of an imperfect orientation of the gradient with respect to the vertical axis. In both cases the current flowing in the coil was abruptly turned off and the system was let free to evolve in trap for a time t_{hold} before taking the picture of the cloud distribution. In this case a simple imaging along y-direction without SG separation was used since the sample was fully polarized. In addition, to magnify the signal, the picture was taken after a time-of-flight of 17 ms.

In Fig. 4.2 the center-of-mass oscillations along the axial (4.2(a)) and vertical (4.2(b)) direction are reported. The trap frequency ω_x is estimated fitting
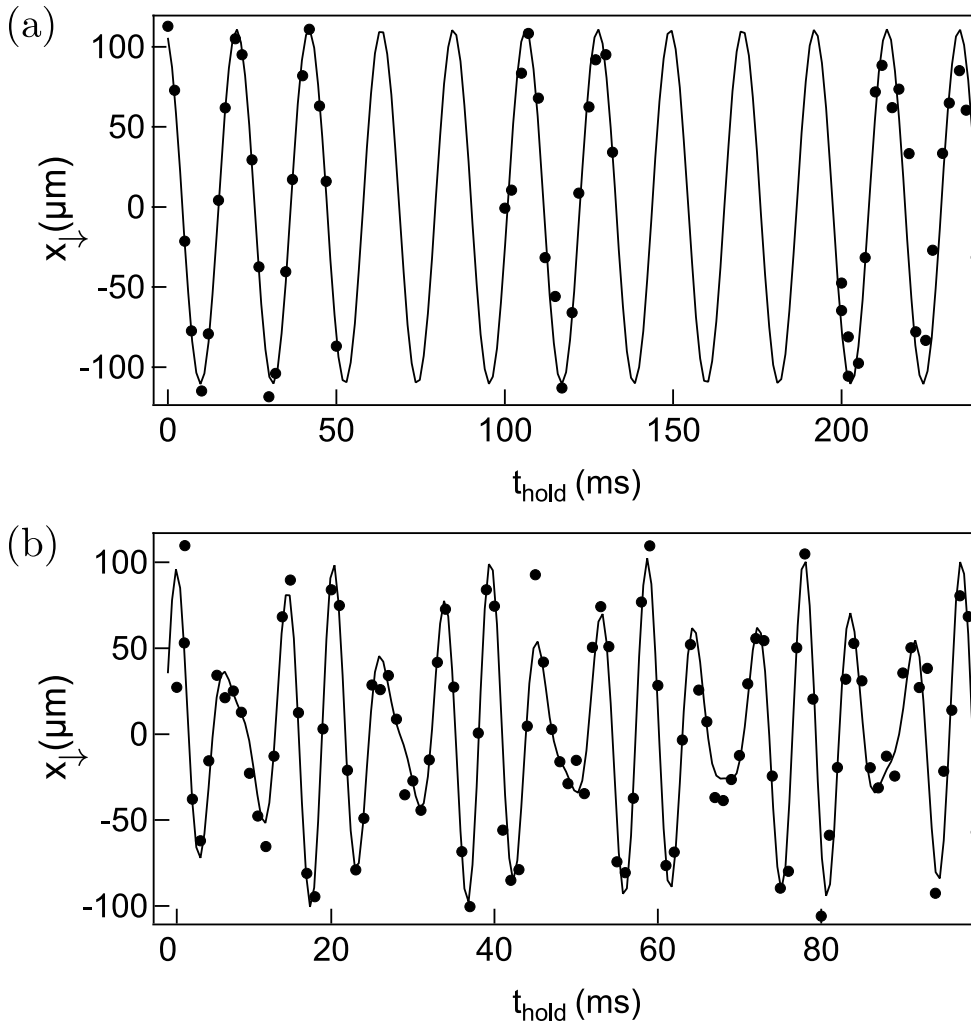
Figure 4.2: Center-of-mass oscillation $x_{\downarrow}$ along the axial (a) and radial (b) direction. In both the figures the black markers are the experimental points while the solid line is the fit used to obtain the trapping frequencies. The fitting functions are a pure sine (a) and a sum of two sinusoidal function having different amplitude.

the axial center-of-mass oscillation with a sinusoidal function, while the radial frequencies ω_y, ω_z were obtained using a beat function as

$$y(t) = A \sin(2\pi\omega_1 t + \phi_1) + B \sin(2\pi\omega_2 t + \phi_2) + y_0, \tag{4.1}$$

where $A, B, \omega_1, \omega_2, \phi_1, \phi_2$ and y_0 are the fitting parameters. The fitted frequencies are $[\omega_x, \omega_y, \omega_z]/2\pi$=[47.7(2), 207.2(3), 156.8(2)] Hz.

Since in this Chapter different trap configurations are considered, in Table 4.1 some relevant parameters characterizing the trap used to study the binary mixture at $T \sim 0$ are reported.

Trap parameters

4.1.2 Calibration of the gradient

When we created the binary mixture for the first time we realized that the two atomic distributions were oscillating out of phase one with respect to the other even in the absence of any external excitation. This was due to a residual axial magnetic gradient of $\sim 0.1\,\text{G/cm}$ able to induce an opposite

Magnetic gradient compensation

	$T \sim 0$ regime		
$N_\uparrow = N_\downarrow$	10^6 (atoms)	N_0/N	> 70 (%)
μ/k_B	200 (nK)	R_x	40 (μm)
$\omega_x/2\pi$	47.7 (Hz)	$\omega_y/2\pi$	207.2 (Hz)
$\omega_z/2\pi$	156.8 (Hz)	T_C	530 (nK)

Table 4.1: Relevant parameters characterizing the trapping potential. Moving from top to bottom the following quantities are reported: (left column) number of atoms in each spin component, the total chemical potential, the trap frequency along $\hat{x}$ and $\hat{z}$, (right column) the condensed fraction, the axial Thomas–Fermi radius (Eq.1.10), the trap frequency along $\hat{y}$ and the critical temperature for a non-interacting system (Eq.1.12).

motion of the two spin states. To avoid this undesired motion we carefully calibrated the residual magnetic gradient every day, since we noticed that there were small day-by-day fluctuations of its absolute value.

The calibration procedure enabled us to control the magnetic gradient with a precision better than 0.5 mG/Acm and it is based on the compensation of the residual magnetic gradient by means of an additional gradient. This compensation gradient is generated using a pair of coils driven with opposite current flow, with symmetry axis along the x direction. It is turned on before the $\pi/2$ Rabi pulse and its modulus is tuned in order to minimize the spin dipole excitation within the detection limit. The residual magnetic gradient was well compensated when the relative motion between the two spin states was stopped.

At this point any variation of the compensation current I_0 produces a controlled magnetic gradient that generates a spin-dependent force on the atoms.

Gradient estimation   Although the theoretical value of the applied gradient can be calculated once that the current and the coil geometry are known, we have directly measured the magnetic gradient produced by the coils. To experimentally determine the magnetic gradient, a simple TOF characterization of the displacement of the center-of-mass position $x_\downarrow$ as function of the applied current can be performed. Given an atomic distribution initially at rest on which a force $\vec{F}$ acts , after a time t the atomic distribution is displaced by the quantity $x = Ft^2/2m$ along the direction of the force. Considering that in our case

$$F = g_F m_F I \frac{dB'_x}{dI},$$

the measured displacement of the atomic cloud after a time t_{TOF} is equal to

$$x_{TOF} = \frac{g_F m_F \cdot I \cdot t_{TOF}^2}{2m} \frac{dB'_x}{dI} \tag{4.2}$$

where g_F is the Landè-factor, m_F defines the internal spin state, dB'_x/dI is the applied magnetic gradient per unit of current along the axial direction, I is the current flowing in the coils and m is the sodium mass.

In Fig.4.3 the displacement Δx of the atomic cloud with respect to the initial position x_{in} as function of the current I is displaced. Performing a linear fit

on the data and using Eq.4.2 dB'_x/dI along the axial direction was estimated as to 0.115(4) G/Acm.
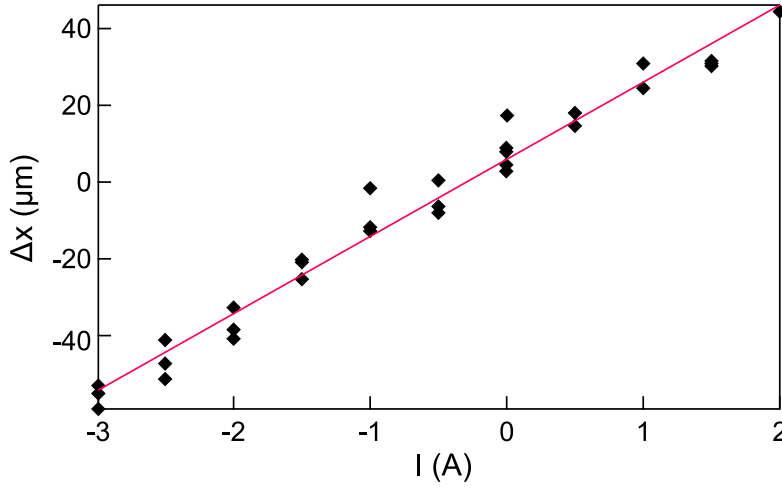

Figure 4.3: Atomic distribution position Δx after a 17 ms TOF as a function of the current I flowing in the coils. The solid line corresponds to the linear fit used to compute the value of the magnetic gradient B'_x.

Once that the value of the applied magnetic gradient is known it is possible to estimate the force acting on the two spin states. This force can be interpreted as a displacement of the trap minima with respect to the rest position. In particular the energy of the trapped system when a magnetic field is present is given by:

$$E = \sum_i \frac{1}{2} m \omega_i^2 x_i^2 + \mu_B m_F g_F |\vec{B}| \tag{4.3}$$

where the first term relates to the optical dipole potential. The equilibrium position is then obtained via differentiation, leading to

$$x_{0i} = x_0 = \frac{\pm g_F m_F \mu_B}{m \omega_i^2} \frac{d|\vec{B}|}{dx_i} \tag{4.4}$$

where $d|\vec{B}|/dx_i$ is the magnetic field gradient.

4.1.3 Measurement of the static polarizability at $T \sim 0$

Our sodium mixture, being completely miscible, allows for the measurement of the linear response to spin excitations, such as the static polarizability. It is related to the ability of the system to adapt itself to an external static spin-dependent force and is deeply sensitive to the vicinity to the miscible-immiscible phase transition. Here the force arises from a shift of the trap minima by a quantity x_0 with respect to the initial resting position. Hence, due to the separation of the trapping potentials, also the atomic distributions of the two components are displaced. For a non-interacting system the separation between the atomic clouds is equal to the distance between the trap minima, while for an interacting system the separation changes. The

different distance between the interacting spin components is related to the SD polarizability $\mathcal{P}$ which is defined as

$$\mathcal{P}(x_0) \equiv \frac{d(x_0)}{2x_0} \tag{4.5}$$

where $2x_0$ is the total distance between the two trap minima and $d(x_0)$ is the relative distance of the center-of-mass $(x_\downarrow, x_\uparrow)$ of the two density distributions as a function of x_0

$$d(x_0) = x_\uparrow(x_0) - x_\downarrow(x_0). \tag{4.6}$$

In a harmonic trap and in linear regime, $\mathcal{P}$ depends only on the scattering lengths characterizing the system [70]. The linear regime is observable for small displacements of the trap minima, such that $2x_0\mathcal{P} \ll R_x$ (where R_x is the TF radius along $\hat{x}$). In this situation it is possible to estimate $\mathcal{P}$ that, given the values of the scattering lengths [78], it is expected to be larger than 20 (see Sec.1.2).

The static SD polarizability was measured using two different methods.

Adiabatic method   The most direct way to study the static response of the system is to adiabatically separate the trapping potential minima. Proceeding in this way, the two atomic distributions do not move once the adiabatic separation is completed. (see Fig.4.6). In order to adiabatically shift the trapping potentials we linearly turn on the magnetic gradient on a timescale of 250 ms which is much longer than the axial frequency timescale. The relative displacement
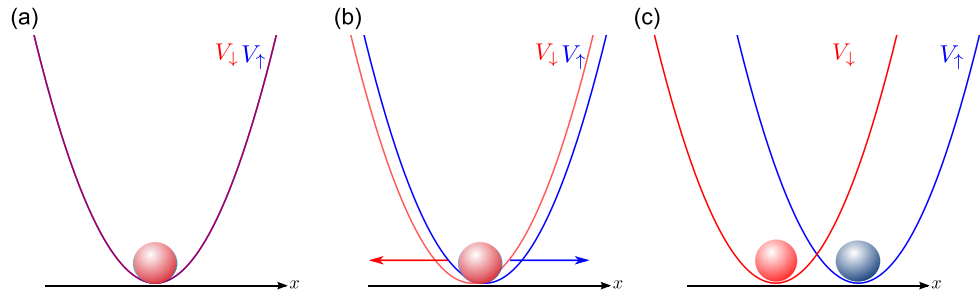

Figure 4.4: Sketch of the trap and atomic configuration before (a), during (b) and after (c) the adiabatic displacement of the trap minima.

as function of x_0 obtained using the adiabatic method is reported in Fig.4.5, where the centers of mass of the two atomic distributions are computed using two independent inverted-parabola fit functions. These data were taken after a 2 ms TOF in SG configuration and show a strong deviation from the behavior of a non-interacting system. In particular for small displacement of the trapping potentials the relative distance of the two atomic distribution shows a linear behavior (linear regime) that tends to saturate outside the linear region.

This behavior results from the crucial role played by interactions, since the SD polarizability is maximum when the two spin distributions overlap completely. Increasing the separation between the $|\uparrow\rangle$ and $|\downarrow\rangle$ states gradually reduces the spatial overlap of the two components, hence relevance of interaction effects.

In Fig.4.5 it is also reported a sketch showing the numerically simulated distributions which present a center-of-mass separation d which is larger than the relative displacement of the two trap potentials. Additional comments on the density distributions and the effect of interaction during the TOF are reported at the end of the section.
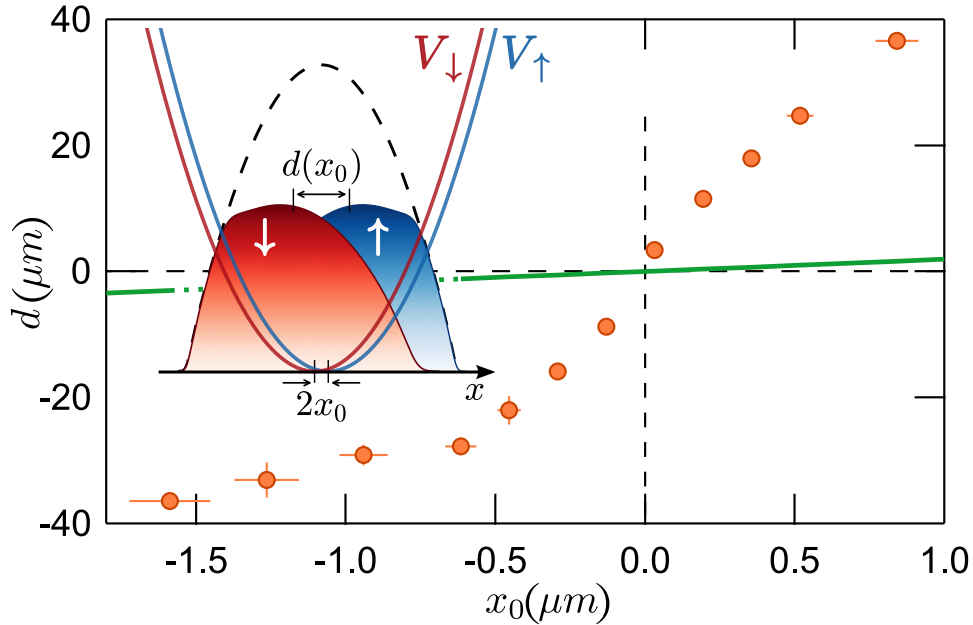

Figure 4.5: Relative displacement d between the two atomic distributions as a function of x_0 (orange dots) obtained using the adiabatic approach. The solid green line corresponds to the case of a non-interacting system for which $d = 2x_0$. A sketch of the numerically simulated distributions for a displacement of $x_0/R_x = 0.01$ is represented as well.

Alternative method

An alternative protocol to indirectly measure the static SD polarizability is based on the measurement of the SD oscillation (see Subs.5.4.5) at different value of x_0. The spin-dipole oscillation is a collective mode presented by
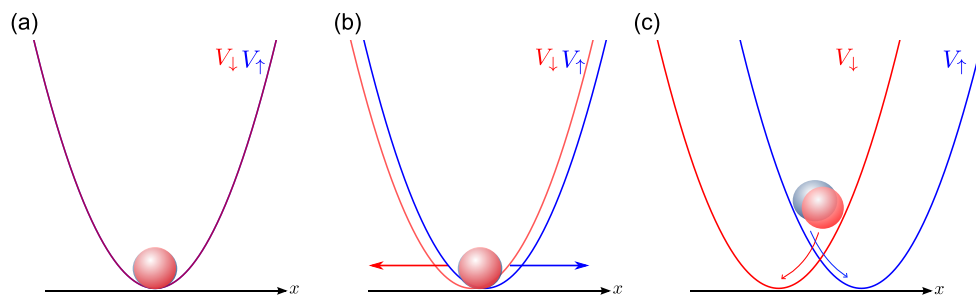

Figure 4.6: Sketch of the trap and atomic configuration before (a), during (b) and at the end (c) of the alternative protocol used to displace the trap minima.

binary systems when the two spin species oscillate in opposite directions. The measurement of the frequency of this oscillation is the subject of the next section where more details on the measurement are reported.
Here I anticipate that the spin-dipole oscillation can be obtained by exciting a relative motion between the two trapped spin components by means of a magnetic field gradient which is abruptly turned on and kept steady during

the evolution of the system. By means of this magnetic gradient the minima of the trapping potentials are displaced such that $V_{\downarrow,\uparrow} = m\omega_x^2(x \pm x_0)^2/2$, where x_0 is computed from Eq.4.4. Since the potentials displacement is not adiabatic, the spin components start to oscillate in opposite directions and a relative sinusoidal motion is excited (Fig.4.4). Similarly to the static case, also with this method, it is important to make the system evolve in the linear regime. The relative motion of the two spin components induced by
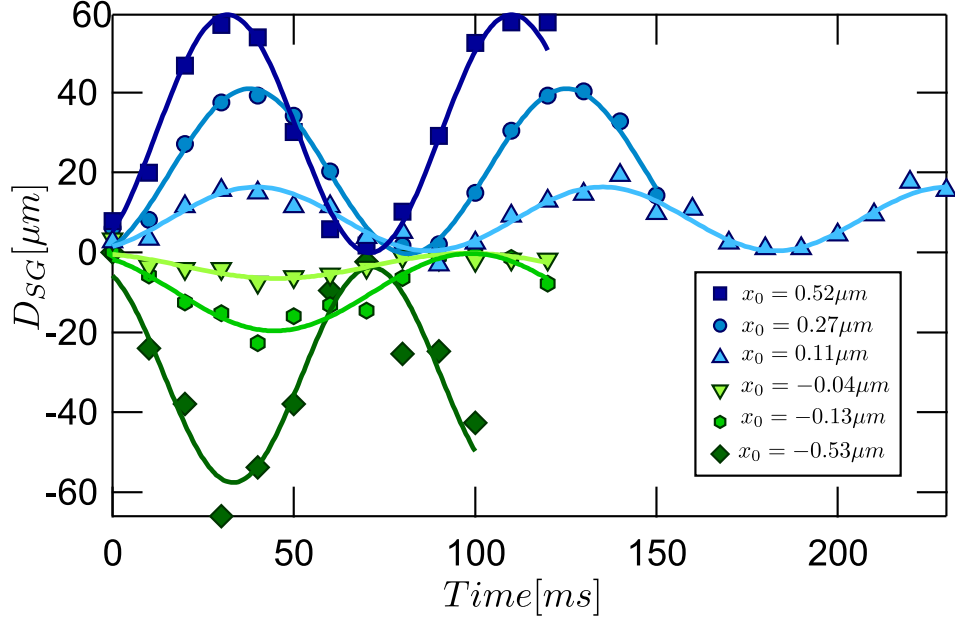

Figure 4.7: Spin-dipole oscillation as a function of the trap minima displacement x_0 after $10\,\mathrm{ms}$ of TOF. The solid lines correspond to the fit computed using Eq.4.7.

the gradient and measured after $10\,\mathrm{ms}$ of TOF, is shown in Fig.4.7. It was fitted using a sinusoidal function

$$D_{SG}(t) = A(x_0, t_{SG}) \cos\left[\omega(x_0)t + \phi(x_0, t_{SG})\right] + y_0, \tag{4.7}$$

where $A(x_0, t_{SG}) = -d(x_0)\sqrt{1 + \omega^2(x_0)t_{SG}^2}$ is related to the in-situ distribution and $\phi(x_0, t_{SG}) = \arctan\left[\omega(x_0)t_{SG}\right]$. Eq.4.7 already takes t_{SG} into account since the displacement between the two spin components after SG expansion is given by $D_{SG}(x_0, t_{SG}) = D(x_0, t) + \partial_t D(x_0, t)t_{SG}$. Here $D(x_0, t)$ is the in-situ relative displacement given by $D(x_0, t) = d(x_0)[1 - \cos(\omega(x_0)t)]$ and $\omega(x_0)$ is the frequency of each oscillation reported in Fig.4.7. This frequency varies as a function of x_0, hence of $A(x_0, t_{SG})$ as shown in Fig.4.13. This small dependence of the SD frequency from the trap minima distance x_0, is related to the size of the excitation which should be small compared to the size of the sample. A theoretical prediction of this dependence is reported in Fig.4.12.

The value of $d(x_0)$, which was computed from $A(x_0, t_{SG})$, is reported in Fig.4.8 as a function of x_0. As it is visible from this figure, the value of $d(x_0)$ shows a non-linear behavior for $|x_0| > 0.2\,\mu\mathrm{m}$. This deviation from the linear behavior is similar to the one observed for the case of steady measurement of $\mathcal{P}$ with adiabatic displacement of the trapping potentials. (see

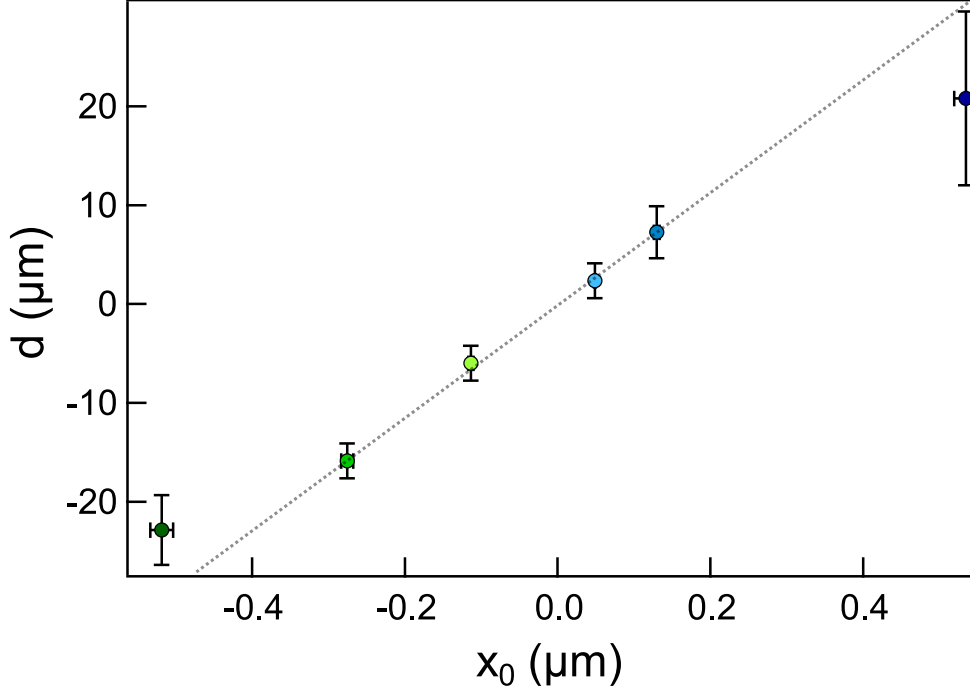Fig.4.5). Once that the value of $d(x_0)$ is known, it is possible to compute

Figure 4.8: Relative displacement d between the two atomic distributions as a function of x_0 obtained using the data of Fig.4.7, where the color of each marker corresponds to the color used for the data set from which d was computed. The dashed gray line is drawn to highlight the non-linear behavior at high value of $|x_0|$.

the static polarizability $\mathcal{P}$. In Fig.4.9 the measurements of the static polarizability, obtained using both procedures, are reported as function of x_0/R_x. In particular the measurements obtained via adiabatic shift of the trapping minima correspond to the orange circles, while the data obtained from the spin-dipole oscillation are indicated as green triangles. In addition, the static polarizability for a non-interacting system is depicted (green solid line) as well as the numerically computed behavior performed via local-density-approximation (LDA) and Gross–Pitaevskii equation (GPE) by Chunlei Qu (see Sec.1.2) (red and black solid lines respectively). The agreement between LDA and GPE simulations is generally very good except for the region close to $x_0 = 0$ where the LDA approximation is no longer valid due to the large value of the spin healing length compared to the trap minima displacement.

From Fig.4.9 we notice that both the static and dynamic experimental data reveal the enhancement of the polarizability with respect to the non-interacting case. In addition, both experimental data well reproduce the scaling with x_0/R_x predicted by numerical simulations. However, the experimental data are given a $\mathcal{P}$ systematically larger than theoretical curves. In first approximation, this can be explained considering that in our data analysis the interaction between the two spin components during SG expansion was neglected. Indeed, performing a GPE simulation of the expansion in the presence of interaction, it turns out that an overestimation of $\mathcal{P}$ of 5 % and of 30 % occurs for a SG expansion of 2 ms and 10 ms, respectively. In addition, since the sample is at $T \sim 0$, a small effect due to the interaction with
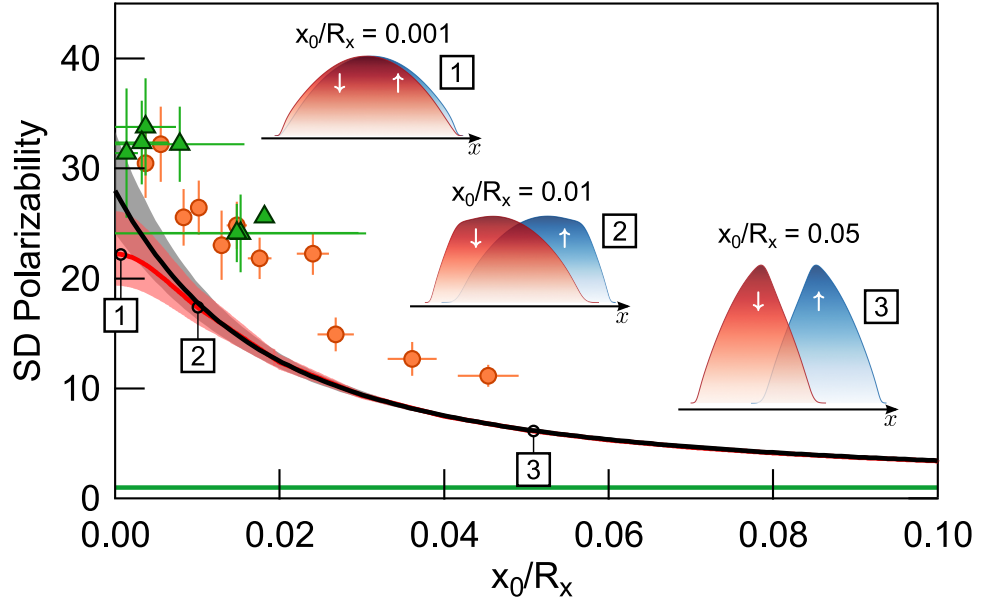
Figure 4.9: SD polarizability computed from the data of Fig.4.5 (orange dots) and Fig.4.7 (green triangles). The black and red solid lines are the prediction computed using the GPE and LDA, respectively. The green solid line corresponds to the case of non-interacting system. The density profiles $n_{\uparrow,\downarrow}(x,0,0)$ from the GPE for $x_0/R_x = 0.001, 0.01, 0.05$ are also reported. The error bars of the experimental data, for all the figures reported in this chapter, are calculated taking into account both the systematic and statistical error which are summed in quadrature, while the theoretical uncertainty is given by the errors on the knowledge of the coupling constants $g_{\uparrow\uparrow,\downarrow\downarrow}$ and $g_{\uparrow\downarrow}$ [78].

thermal atoms should be considered (see Sec.1.5 and Sec.4.2).

Another relevant feature concerning our experimental data regards the fitting formula for the density distributions. In fact, performing GPE simulations of the density profiles at different x_0, it turned out that the usual inverted parabola expected in the Thomas–Fermi limit is no longer a good approximation of the atomic distribution shape. This is particularly true for large values of x_0 as visible from Fig.4.9, where the theoretical density distribution profiles are reported for three different value of x_0.

Since, in our experiment it is difficult to resolve the details of the axial density density distribution in each spin state, we simply fit all our density distributions to the standard inverted-parabola profile. However, we have estimated the discrepancy between the center-of-mass of the density distribution computed via experimental fit and via direct integration of the computed distribution. This discrepancy results in an overestimation of the experimental SD polarizability $\mathcal{P}$ of at most 6%.

4.1.4 Measurement of the spin dipole oscillation at $T \sim 0$

In addition to the static SD polarizability, another quantity that can be measured in our harmonically trapped sodium mixture is the value of the spin-dipole oscillation frequencies ω_{SD}. As explained in Subs.5.4.5, the SD oscillation corresponds to the out-of-phase motion between the two spin

components. The frequency at which this oscillation occurs depends on interactions and, in our case, is expected to be about 0.2 times smaller than the harmonic oscillator trap frequency. To measure ω_{SD} two different methods, labeled as direct and indirect, were used.

In the direct method, we excite the SD oscillation by suddenly applying a magnetic gradient generated with the pinch coil, which is kept on for a few ms and is then turned off. Thus, we can think at it as a kick able to excite the atomic motion, with the two component oscillating back and forth around the same point (their potential minima coincide during the motion as sketch in Fig.4.4). To detect the spin-dipole oscillation we used SG imaging and the two atomic distributions were independently fitted in order to estimate d. The relative displacement of $|\uparrow\rangle$ and $|\downarrow\rangle$ measured after TOF is indicated as D_{SG} in order to underline that it does not correspond to the in-situ separation. The formula that links D_{SG} to the in-situ displacement d is Eq.4.7. As in the measurement of the axial trapping frequency, the relative position D_{SG} was measured for different holding times t_{hold} and is reported in Fig.4.10.
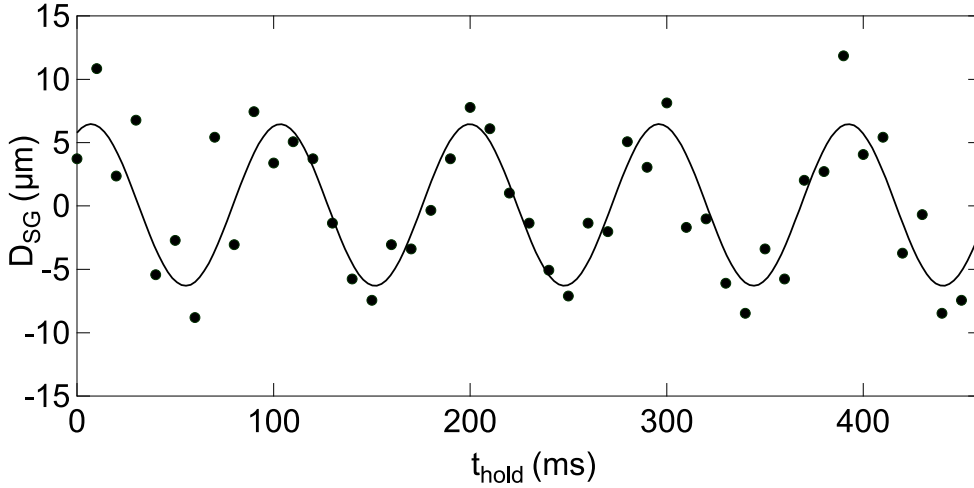
Direct method

Figure 4.10: SD oscillation along the axial direction as a function of the holding time. The solid line corresponds to the sinusoidal fit from which the SD frequency was measured. To take these data a 3 ms gradient pulse and a 10 ms t_{TOF} were used.

From the fit of $D_{SG}(t_{\text{hold}})$, a SD frequency $\omega_{SD}/2\pi$=10.4(1) Hz was found. This value can be compared with the trap frequency ω_x being their ratio $\omega_{SD}/\omega_x = 0.218(2)$ [69]. The difference between the two frequencies is clearly visible from Fig.4.11, where a direct comparison of the two measurements is reported.

The experimental estimate of ω_{SD} can be compared to the theoretical simulations performed within LDA and via numerical integration of GPE. Using our experimental parameters, ω_{SD} turned out to be equal to $\omega_{SD}/\omega_x = 0.189(15)$ for the LDA and $\omega_{SD}/\omega_x = 0.213(17)$ for the GPE simulations, respectively. Since it is not possible to easily simulate the dynamics of our systems, the values of ω_{SD} were estimated starting from the estimate of $\mathcal{P}$, using the relation based on a sum rule approach (see Subs.1.2.3)

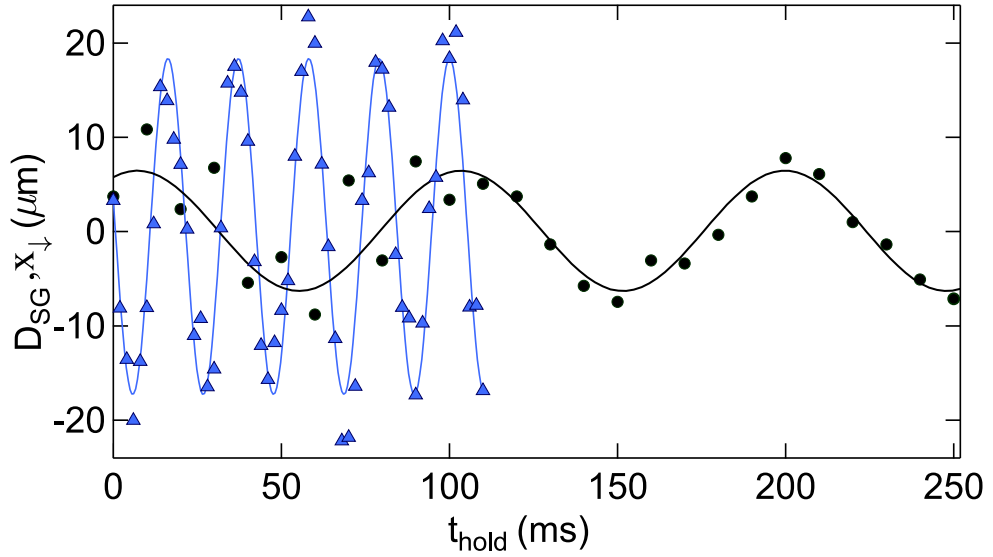$$\omega_{SD} = \frac{\omega_x}{\sqrt{\mathcal{P}(x_0 \to 0)}} \tag{4.8}$$

Figure 4.11: Comparison of the spin-dipole (black circles) and center-of-mass (blue triangles) oscillations. Note that the data of the center-of-mass oscillation $x_\downarrow$ reported in the figure are taken with a smaller magnetic gradient with respect to the case reported in Fig.4.2.

where $\mathcal{P}(x_0 \to 0)$ is the value of the static polarizability in the linear regime, *i.e.*, $x_0 \to 0$ (see Subs.4.1.3).

It is worth to mentioning that, in order to consider Eq.4.8 valid, it is the necessity to have a small in-situ amplitude compared to the Thomas–Fermi radius. Only when the amplitude of the oscillation is small compared to the sample size, Eq.4.8 is valid. Indeed, performing a dynamical simulation of the SD oscillation frequency, it turns out that Eq.4.8 is strictly valid only for $x_0/R_x < 0.02$ and that the SD frequency slightly depends on the initial amplitude x_0 as reported in Fig.4.12.

In our experiment, taking the time-of-flight into account, a good approximation for the in-situ amplitude is $D_{SD} = D_{SG}/\sqrt{1 + \omega_{SD}^2 t_{TOF}^2} = 5.4 \ \mu$m which is small compared to the Thomas–Fermi radius R_x=40 μm.

Indirect method   A different way to measure the SD frequency is based on the indirect method. In this framework, the value of ω_{SD} is extrapolated from measurements of the frequency $\omega(x_0)$ taken for different displacements of the trap minima. These data are reported in Fig.4.7 and are the same used to indirectly estimate $\mathcal{P}$. Differently from the direct method, the magnetic gradient is kept on up to the end of the experimental sequence.

The value of ω_{SD} is obtained extrapolating the value of the SD oscillation frequency $\omega(x_0)$ at $x_0 = 0$. To extrapolate this value we fitted the frequency of the oscillation $\omega(x_0)$ as function of the amplitude $A(x_0, t_{SG})$ using a linear function, where the y-intercept of the line corresponds to the value of ω_{SD}. The values of the frequency $\omega(x_0)$ in units of ω_x as function of the amplitude $A(x_0, t_{SG})$ are shown in Fig.4.13, where a comparison with the theoretical expectations is also reported.

As clearly visible from Fig.4.13 the extrapolated value of ω_{SD} is compatible with the prediction of the local-density-approximation (LDA) and slightly
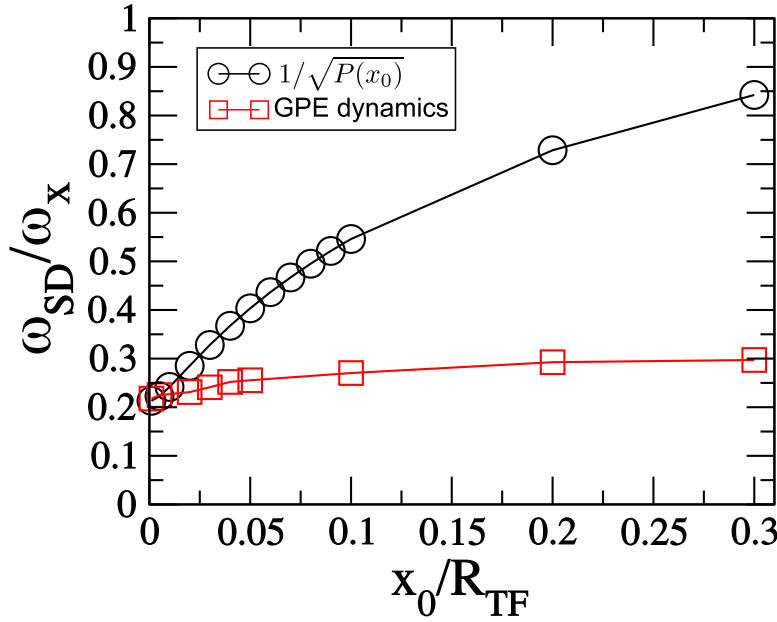
Figure 4.12: Comparison of the dynamical simulated SD oscillation frequency (red squares) and the formula $\omega_{SD}/\omega_x = 1/\sqrt{\mathcal{P}(x_0)}$ (black circles) for $T = 0$. To compute the GPE dynamics, the imaginary time evolution of the Gross–Pitaevskii equation for a system in which the two trapping minima were initially displaced by $2x_0$ was taken as starting condition for the real time evolution of the system were the trap minima coincide.

smaller than the one obtained using the Gross–Pitaevskii equation (GPE). Since the local-density-approximation tends to fail at small value of x_0, the most reliable estimation of ω_{SD}/ω_x is the one obtained via numerical integration of the GPE. This suggests that in order to measure the SD oscillation frequency, the direct protocol is more advisable.

4.2 TWO–COMPONENT BEC AT FINITE TEMPERATURE

This section is devoted to the results obtained studying a two-component BEC at finite temperature. In this regime, the system can be described by a four-fluid model, where two condensates and two thermal clouds are present. In this framework, the interaction between BEC and thermal cloud are not negligible, since they are able to considerably affect the SD polarizability of the system.

As in the previous section the SD oscillation and polarizability were studied and compared with the theoretical simulations. In particular, the role of temperature was investigated for two different regimes, labeled as collisionless and collisional, in which the interactions among thermal atoms were different.

4.2.1 Collisional regimes

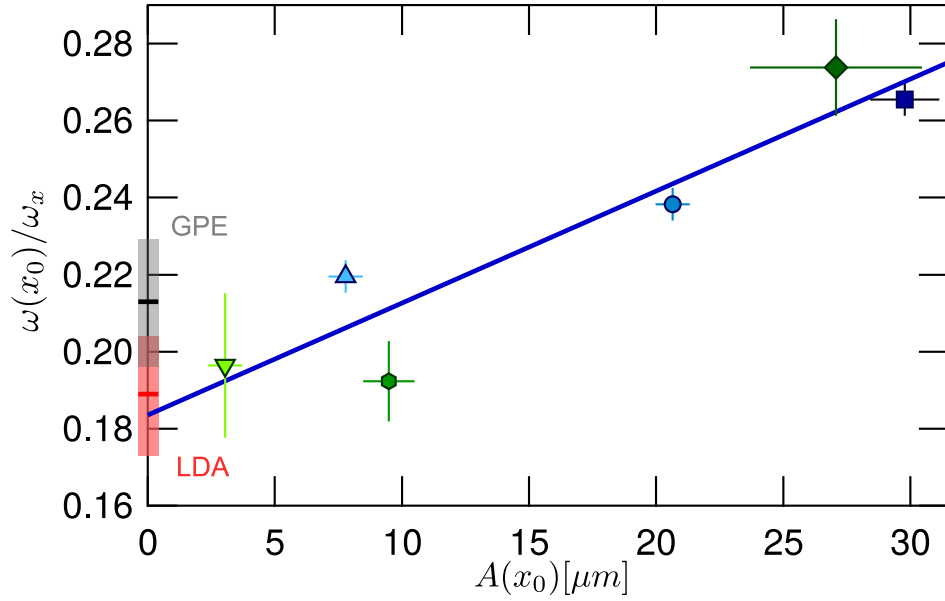When dealing with a system at finite T, interactions among atoms can

Figure 4.13: Ratio $\omega(x_0)/\omega_x$ as a function of the amplitude $A(x_0)$ for the data reported in Fig. 4.7 (same marker styles). The black (red) marker is the prediction of the GPE $\omega_{SD}/\omega_x = 0.213(17)$ (LDA $\omega_{SD}/\omega_x = 0.189(15)$). The y-intercept of the linear fit gives $\omega_{SD}/\omega_x = 0.18(1)$.

be described using a mean-field approach which reveals three interaction phenomena (see 1.4). On the one hand, we have the interaction among condensed atoms ($gn_0^2/2$ term in Eq.1.50) and among thermal atoms (gn_T^2 term) and, on the other, there is the mutual interaction between BEC and thermal cloud (proportional to $gn_T n_0$).

Usually gn_T^2 is neglected in the description of the system, since the density of the thermal cloud is generally small compared to n_0. However, depending on the collisional rate among thermal atoms, two different regimes can be distinguished, which are labeled as collisionless and collisional.

These two regimes can be distinguished by introducing the collisional time τ, that in the case of distinguishable particles $|\uparrow\rangle$ and $|\downarrow\rangle$ is
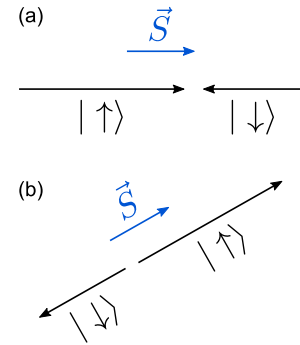

Figure 4.14: Sketch of the spin current before (a) and after (b) collisions in the case of collision between atoms with different spin $|\uparrow\rangle$ and $|\downarrow\rangle$.

$$1/\tau_{\uparrow\downarrow} = n_{\uparrow\downarrow}^T \sigma_{\uparrow\downarrow} v_{rel}, \tag{4.9}$$

where $n_{\uparrow\downarrow}^T = \left[m\bar{\omega}^2/(2\pi k_B)\right]^{3/2} N_{\uparrow\downarrow} T^{-3/2}$ corresponds to the peak density of the non-interacting thermal distribution [42], $N_{\uparrow\downarrow} = N/2$, m is the atom mass and $\bar{\omega} = (\omega_x \omega_y \omega_z)^{1/3}$ is the geometric average of the harmonic oscillator frequencies. In addition, in Eq.4.9 $\sigma_{\uparrow\downarrow} = 4\pi a_{\uparrow\downarrow}^2$ is the cross section of two distinguishable particles and $v_{rel} = \sqrt{8k_B T/(\pi m_r)}$ is their average relative velocity and $m_r = m/2$ is the reduced mass.

Comparing the value of the collisional time $\tau_{\uparrow\downarrow}$ with the relevant excitation frequency ω it is possible to distinguish between collisionless and collisional

regime. More in detail, if $\omega\tau_{\uparrow\downarrow} \gg 1$ the system is called collisionless, while if $\omega\tau_{\uparrow\downarrow} \ll 1$ the system is labeled as collisional [126].

The collisionless regime is usually achieved at low temperature and/or low density of the thermal cloud and is generally described by mean-field approaches, where the thermal atoms are treated as a thermal bath lacking of damping. Damping mechanisms usually appear at high temperatures and/or high thermal densities, when collisions are more important and can affect the nature of the collective excitations, leading to the so called spin drag effect [33], *i.e.*, a relaxation mechanism due to collisions between different spin species (see Fig.4.14).

Thus, in order to include damping, a dynamic description of both condensed and thermal distributions is needed.

In our case, it was possible to explore both regimes by changing the trap geometry. In particular, in the crossed-dipole trap a collisionless regime was found, while the single-beam trap configuration is characterized by a more collisional regime. The estimated value of $\omega\tau_{\uparrow\downarrow}$ for both trap geometries are reported in Tab.4.2 and Tab.4.3.

4.2.2 Traps frequencies and depths

As already mentioned, the role of the temperature was investigated using two different trap geometries. The use of a second trap configuration was needed to ensure the adequate trapping of the thermal atoms.

Considering a single-focused beam propagating along $\hat{x}$, the trapping potential U is *Trap depth*

$$U(r,x) = \frac{3\pi c^2}{2\omega_0^3}\frac{\Gamma}{\Delta}I(r,x), \tag{4.10}$$

where Γ is the natural linewidth of the resonant excited state, Δ is the detuning of the trapping laser with respect to the resonance transition and $I(r,z)$ is the Gaussian laser intensity given by

$$I(r,x) = \frac{2P}{\pi w^2(x)}exp\left(-\frac{2r^2}{w^2(x)}\right). \tag{4.11}$$

In Eq.4.11, r identifies the radial directions y and z, while $w(x)$ is equal to

$$w(x) = w_0\sqrt{1 + \left(\frac{x}{x_R}\right)^2} \tag{4.12}$$

being w_0 the waist of the beam and x_R the Rayleigh range.

When $U(r,x) > k_B T$ and the radial and axial extension of the sample are smaller than the waist and Rayleigh range of the Gaussian beam respectively, the optical potential can be approximated to a harmonic oscillator with cylindrical symmetry so that the trapping frequencies are

$$\omega_x = \sqrt{\frac{2U_0}{mx_R^2}} \tag{4.13}$$

$$\omega_r = \sqrt{\frac{4U_0}{mw_0^2}}, \tag{4.14}$$

being $U_0 = U(r = 0, x = 0)$. The central trapping depth U_0 can be determine experimentally by measuring the trap frequency and inverting Eqs.4.13 and 4.14.

Another issue to consider is the role played by gravity. Indeed, the gravity potential induces a lowering of the vertical potential depth that, in first approximation, is equal to

$$U_{grav} = mgw_0 \tag{4.15}$$

where g is the Earth gravity acceleration. This also results in a gravitational sag of the trap center (see also Sec.2.3)

$$\Delta z = \frac{g}{\omega_z^2}. \tag{4.16}$$

For a given beam power, the larger the waist of the trapping beam, the more important is the role of gravity.

In our case, the crossed-dipole trap geometry not only has a relatively small trap depth (of the order of T_C), but it was deeply affected by gravity. In fact, since the horizontal beam waist was of the order of $\sim 50\ \mu$m, the correction due to gravity was not negligible compared to the vertical trap depth (see Tab.4.2). For this reason, we reduced the focus of the horizontal beam in order to increase the trap depth and to reduce the gravitational sag.

The further focusing of the horizontal beam has led to the necessity to use a single-beam configuration, since the crossed-dipole beam configuration was no longer suitable to trap the whole sample. In fact, the tightly-focused horizontal beam was able to capture the warmest atoms which were not trapped by the crossed configuration. This was experimentally observed and the proof is reported in Fig.4.15. From the figure, it is visible that the thermal and condensed clouds have a different behavior, suggesting that they were experiencing different trapping potentials. In fact, while the BEC oscillates at a certain frequency, the thermal atoms show a quickly suppress oscillation at a much lower frequency. To solve this problem we used a single-beam trap configuration.

The trapping frequencies of the crossed-dipole configuration were directly measured using the same procedure described in Subs.4.1.1 and they are $[\omega_x, \omega_y, \omega_z]/2\pi$=[87.4(3), 327(1), 247.6(8)] Hz (see Fig.4.16).

For what concerns the single-beam trap, due to the tight radial confinement, we chose to measure the radial frequency via parametric heating (see Sec.3.5). This procedure permits to determine the trapping frequency inducing a resonant heating mechanism in the sample. The radial frequencies were measured using a thermal sample in order to avoid confusion with excitation of many-body modes of the BEC. Such measurements gave $[\omega_x, \omega_y, \omega_z]/2\pi$=[11.9(1), 1350(100), 1350(100)] Hz.

In Tabs.4.2 and 4.3 all the relevant parameters of the crossed-dipole and   single-beam trap configurations are reported.

The advantage of using a single-beam trap geometry is even more clear when a direct comparison between the two trap configurations is made. Thus, in the following, I will present and compare some relevant issues characterizing both trap configurations.
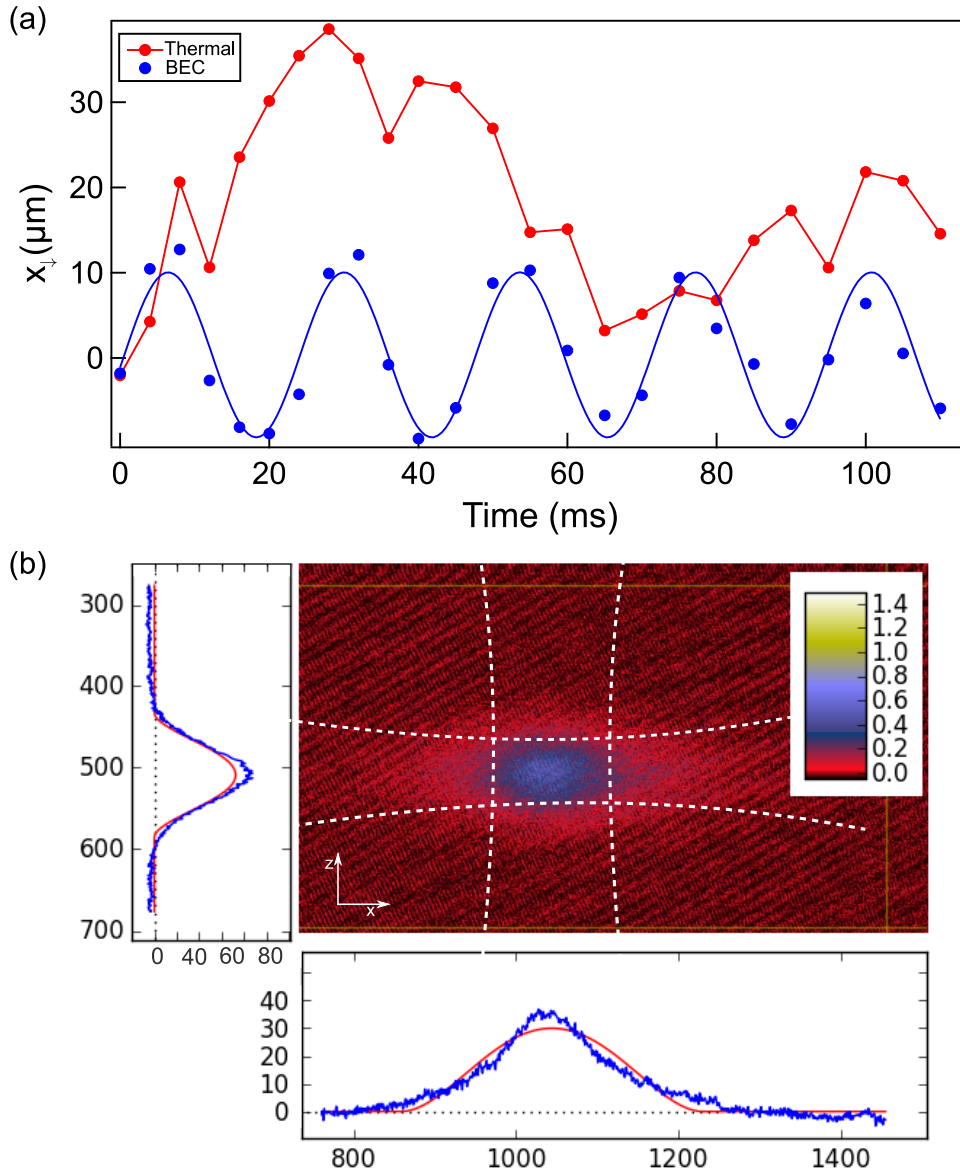
Figure 4.15: (a) Center of mass motion of the $|\downarrow\rangle$ component of the condensed (blue) and thermal (red) atoms as a function of time measured after 17 ms of TOF in the crossed-dipole configuration. The BEC presents several oscillations at the trap frequency, while the thermal cloud presents a damped oscillation at a lower frequency. (b) Sketch of the thermal sample trapped in the crossed-dipole configuration with the real fit profiles along $\vec{x}$ and $\vec{z}$ obtained using a Gaussian function. The length of the density distributions are expressed in pixel (1pixel $= 4.4\,\mu m$, while the colorscale represents the OD. As visible, while along the z direction the density profile is well reproduced by a Gaussian function, along x the density distribution do not coincide with the standard Gaussian distribution.

In order to prove that in the crossed-dipole configuration it was not possible to heat the sample at different temperatures, some relevant parameters for two different condensed fractions are compared in Fig.4.17.

By looking at Fig.4.17(a,b), one can deduce that in both situations the absolute temperatures of the sample was essentially the same. In fact, considering that $\sigma \propto T^{1/2}$ and that for a trapped sample $N_{Th} \propto T^3$ (see Sec.2.6), the ratio between the two σ (which is compatible with the ratio of the number of ther-
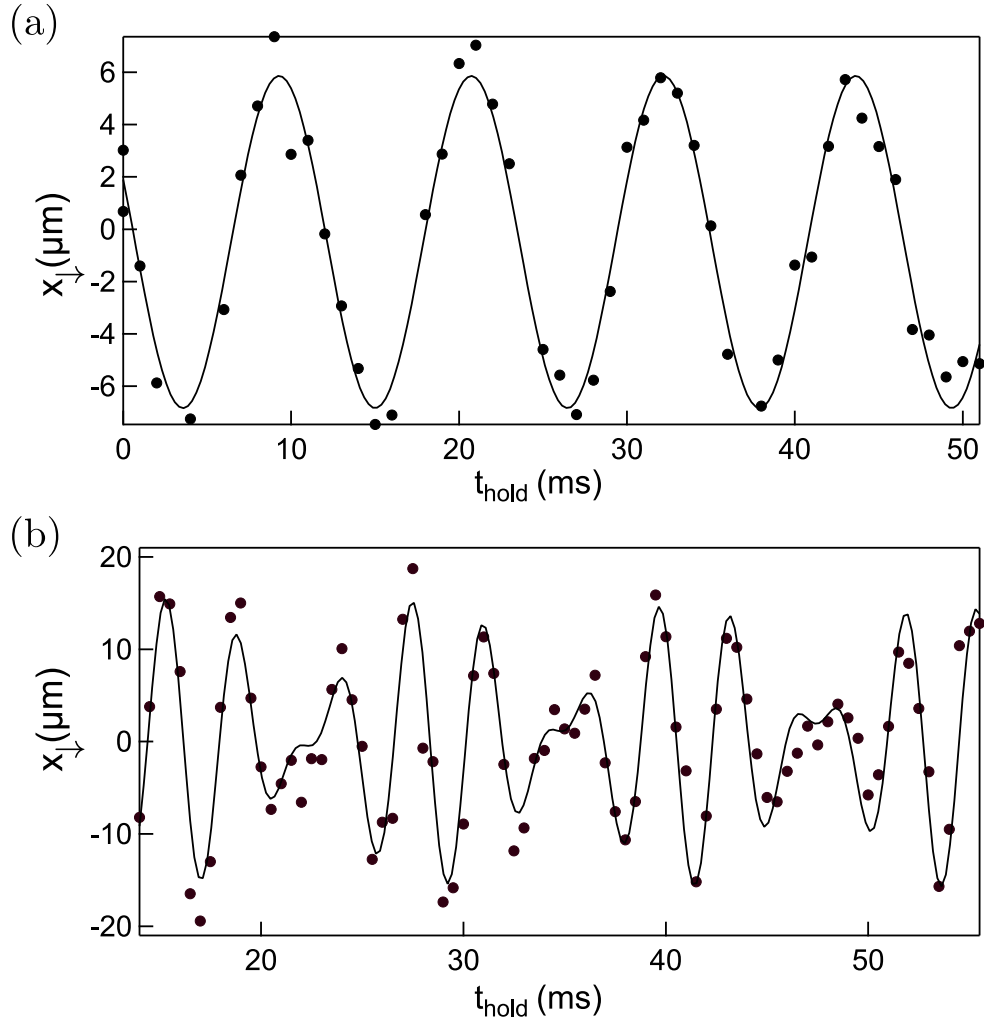
Figure 4.16: Center-of-mass oscillation along the axial (a) and radial (b) direction for the trap configuration associated with the collisionless regime. In both the figures the black markers are the experimental points while the solid line is the fit used to obtain the trapping frequencies. The fitting functions are a pure sine (a) and a sum of two sinusoidal function having different amplitude.

mal atoms at the power of six) is close to one. In addition, since the number of thermal atoms remains almost constant in time, the temperature can be considered fixed.

However, the configuration associated to $N_0/N = 0.23$ presents an initial total number of atoms N smaller than the case associated to $N_0/N = 0.35$. This suggest that the effect of the induced "heating" is to empty the sample, rather than warm it.

Lastly, it is worth to note that the number of condensed atoms is decreasing in time, as well as the BEC fraction (Fig.4.17(c,d)). This phenomenon might be due to some loss mechanisms. Three-body recombination effect, loss due to the presence of the μ-wave or frequency/intensity noise of the infrared laser beam are possible loss mechanisms able to affect our system. However, using the three-body recombination rate measured in [43] and the computed peak density of our system (of the order of $^{14}\,\mathrm{cm}^{-3}$), the timescale for three-body loss decay is of a few tens of seconds. This is inconsistent

Collisionless regime			
$N_\uparrow = N_\downarrow$	$4 \cdot 10^5$ (atoms)	R_x	25 (μm)
μ/k_B	250 (nK)	$\tau_{\uparrow\downarrow}$	~25 (ms)
n_T	$2.5 \cdot 10^{13}$ (cm^{-3})	T_C	640 (nK)
U_{0x}/k_B	4.2 (μK)	U_{0z}/k_B	2.1 (μK)
U_{grav}/k_B	1.3 (μK)	Δz	4 (μm)
w_{0x}	~ 50 (μm)	z_{Rx}	~ 7 (mm)
$\omega_x/2\pi$	87.4 (Hz)	$\omega_y/2\pi$	327 (Hz)
w_{0z}	~ 100 (μm)	z_{Rz}	~ 30 (mm)
$\omega_z/2\pi$	247.6 (Hz)	$\bar{\omega}/2\pi$	190 (Hz)

Table 4.2: Relevant parameters characterizing the crossed-dipole trap used in the collisionless regime. Moving from top to bottom, the following quantities are reported: (left column) number of atoms in each spin component, the total chemical potential, the thermal peak density at T_C, the axial trap depth, the gravitational potential depth, the x trap frequency, the z trap frequency, (right column) the condensed fraction, the collisional time at T_C, the critical temperature, the z trap depth, the gravitational sag, the y trap frequency and the geometric average of the harmonic oscillator.

Collisional regime			
$N_\uparrow = N_\downarrow$	$4 \cdot 10^5$ (atoms)	R_x	230 (μm)
μ/k_B	400 (nK)	$\tau_{\uparrow\downarrow}$	~10 (ms)
n_T	$5 \cdot 10^{13}$ (cm^{-3})	T_C	850 (nK)
U_{0x}/k_B	7 (μK)	$\bar{\omega}/2\pi$	280 (rad/s)
U_{grav}/k_B	0.3 (μK)	Δz	0.13 (μm)
w_{0x}	~ 12 (μm)	z_{Rx}	~ 0.4 (mm)
$\omega_x/2\pi$	11.9 (Hz)	$\omega_y/2\pi$	1350 (Hz)
$\omega_x/2\pi$	1350 (Hz)		

Table 4.3: Relevant parameters characterizing the single-beam trap used in the collisionless regime. Moving from top to bottom, the following quantities are reported: (left column) number of atoms in each spin component, the total chemical potential, the thermal peak density at T_C, the axial trap depth, the gravitational potential depth, the x trap frequency, the z trap frequency, (right column) the condensed fraction, the collisional time at T_C, the critical temperature, the z trap depth, the gravitational sag, the y trap frequency and the geometric average of the harmonic oscillator.

with the timescale observed, which is two orders of magnitude faster. Thus, this loss mechanism can be ascribed to hyperfine relaxation [99], where two thermal atoms having opposite spin can interact producing two atoms in $|1, 0\rangle$. These atoms can be initially promoted to $|2, 0\rangle$[1] due to the μ-wave and then decay (via hyperfine relaxation) to the ground state releasing an

---

[1] A direct promotion of atoms in $|1, \pm 1\rangle$ states in $|F = 2\rangle$ is negligible considering that the linear Zeeman shift among each level is of the order of 400kHz.
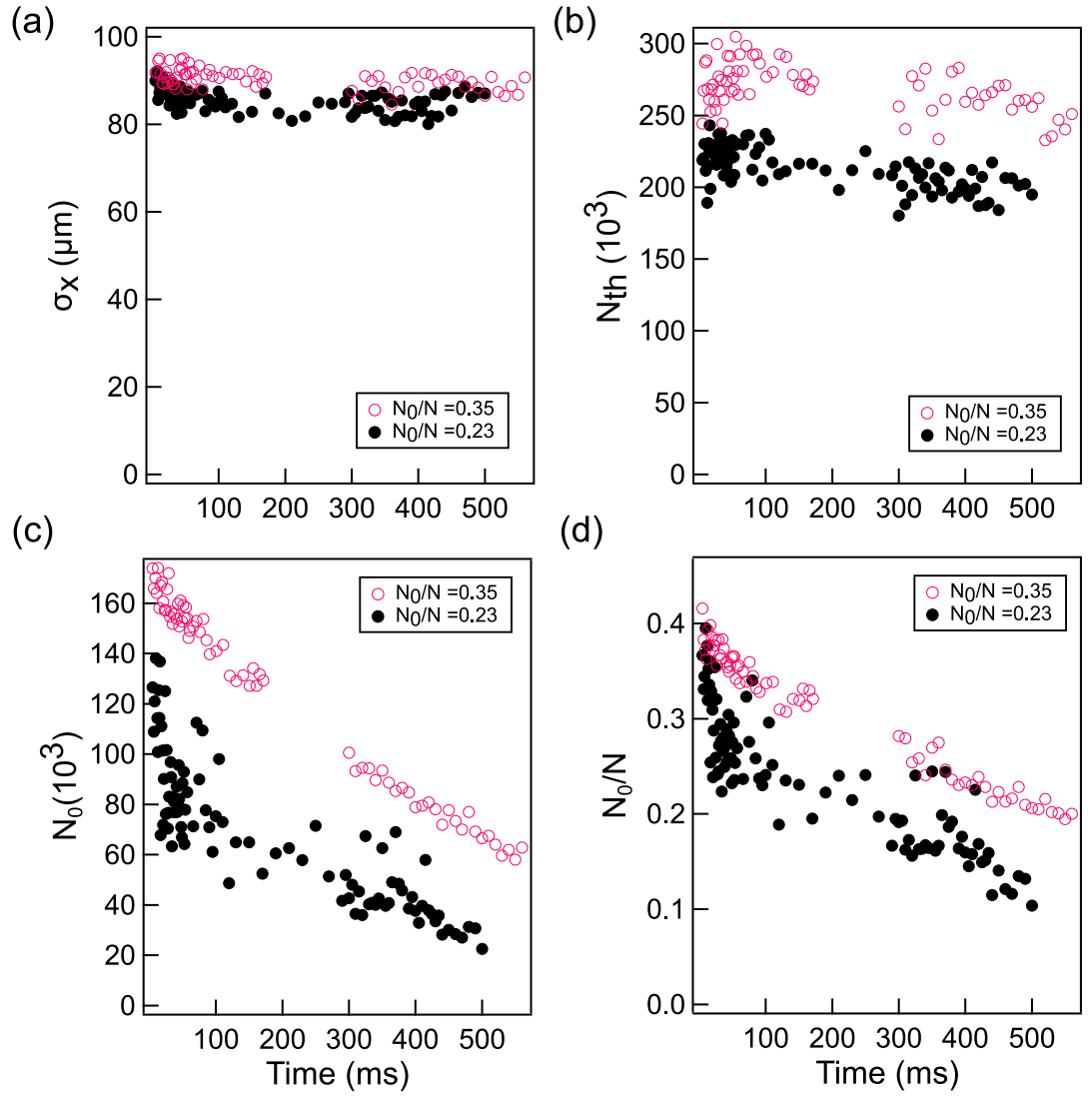
Figure 4.17: Axial width of the Gaussian thermal distribution (a), number of thermal atoms (b), number of condensed atoms (c) and BEC fraction as functions of time for the atoms occupying the $|\downarrow\rangle$ spin state in the collisionless regime (crossed-dipole trap) after 7 ms of TOF. The empty magenta circles correspond to a condensed fraction equal to $N_0/N = 0.35$, while the solid black circles correspond to a condensed fraction equal to $N_0/N = 0.23$. The behavior of the $|\uparrow\rangle$ is similar in all four cases. In this configuration, due to a small trap depth, it was not possible to properly heat the sample and the effect of the heating procedure was to empty the condensate.

amount of energy higher than the trap depth ($E/h = 1.771$ GHz). Since this energy is transferred to the two interacting atoms in term of kinetic energy, they can be escape from the optical trap. However, it is possible that part of this energy is transferred to the system so that it can remain at equilibrium. By means of the single-beam trap, it is possible to overcome some limits imposed by the crossed-dipole configuration. To prove that, a similar analysis to the one done for the crossed-dipole trap is reported in Fig.4.18.

From Fig.4.18, it is visible that σ and N_{Th} are different depending on the BEC fraction, meaning that the two sample are at different temperatures. In addition, also in this case, the initial temperature of the sample remains con-
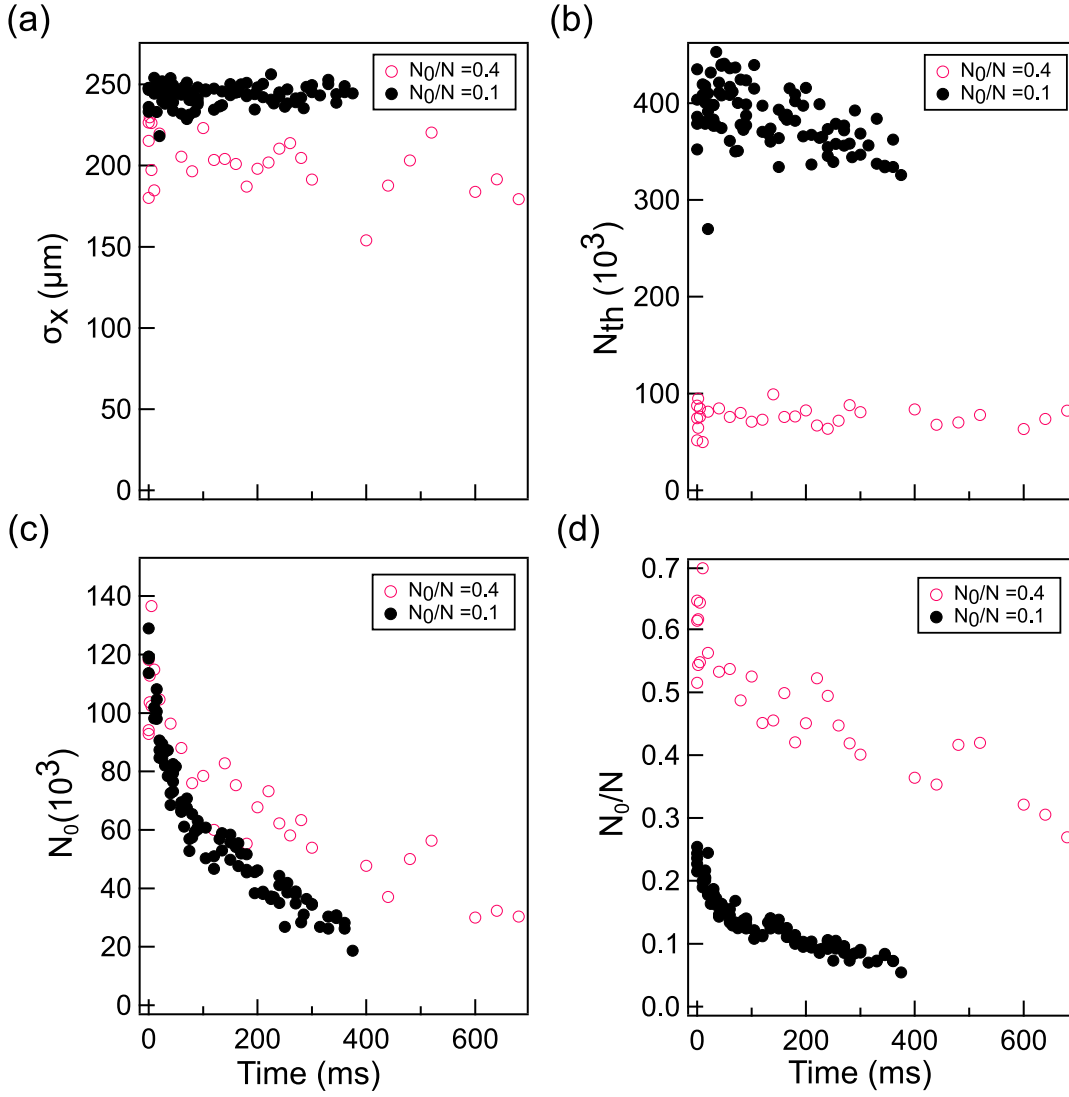
Figure 4.18: Axial width of the Gaussian thermal distribution (a), number of thermal atoms (b), number of condensed atoms and BEC fraction (c) as functions of time for the atoms occupying the $|\downarrow\rangle$ spin state in the collisional regime (single-beam trap) after 7.5 ms of TOF . The empty magenta circles correspond to a condensed fraction equal to $N_0/N = 0.4$, while the solid black circles correspond to a condensed fraction equal to $N_0/N = 0.1$. The behavior of the $|\uparrow\rangle$ is similar in all four cases. This configuration permitted to control and tune the temperature of the sample at will.

stant in time, since the number of thermal atoms does not change. However, in this situation there is a discrepancy ($\sim 20\%$) between the temperature estimated using σ and N_{Th}. This can be related to the difficulty in estimate the real number of atoms at such a low temperature and/or deviation from a Gaussian profile due to interactions.

However, as for the crossed-dipole, we observed a reduction of the BEC fraction during the evolution of the system, proving that this loss phenomenon is independent of the trap configuration.

The presence of this loss mechanism explains why we were able to observed only one complete SD oscillation in the collisional regime, where the SD oscillation period was of the order of 500 ms.

The analysis for the $|\uparrow\rangle$ spin component was also done and provides results consistent with the one reported in Fig.4.17 and Fig.4.18for $|\downarrow\rangle$. In addition, the condensed fractions were found to be equal within 10% uncertainty.

4.2.3 Measurement of the spin dipole oscillation at finite temperature

As for the zero temperature case, we investigated the spin dynamics of the system at finite temperature by looking at the SD oscillation both in the collisionless and collisional regime. From the SD oscillation data, we directly observed that the two trapping geometries provide different collisional regimes for the thermal atoms that show a different dynamics. In both regimes investigated, we started with a sample close to $T = 0$ and we heated it by means of parametric heating (see Sec.3.5).
To measure the SD frequency at finite T, we used the direct method (see Subs.4.1.4), which was proven to be more reliable. The measurements related to the collisional regime were taken switching off the compensation magnetic gradient descibed in Subs.4.1.2 for a few ms before restoring its initial value. For these data set we used a slightly different setup and, since the response time of the power supply used to produce the magnetic gradient is of the order of a few hundreds of μs, we were limited in the lowest force applicable to the system.
On the contrary, for the collisionless case, we were able to turn on an additional magnetic gradient, keeping the compensation one always on. This enabled us to control the magnitude of the force acting on the atoms with high precision. This is the reason why, in general, the oscillation amplitude of the collisionless case is smaller than the one observed in the collisional regime.

$T < T_C$ case   In Fig.4.19 the spin-dipole oscillations in the collisionless and collisional regimes are reported for the case of a condensed fraction equals to $N_0/N_{tot} = 0.3$ and $N_0/N_{tot} = 0.4$ respectively [77].

At finite temperature the binary system is composed of four fluids, being the two spin components of the thermal and condensed atoms. To distinguish between the spin components we keep using the labels $|\uparrow\rangle$ and $|\downarrow\rangle$, while to discern between the thermal and condensed atoms I introduce the labels T and 0, respectively. In this framework, the spin-dipole oscillation of the system is characterized by the relative motion of the condensed and thermal distributions, which are defined as

$$S^0 = x_\downarrow^0 - x_\uparrow^0 \qquad\qquad S^T = x_\downarrow^T - x_\uparrow^T. \qquad\qquad (4.17)$$

To independently identify the centers of mass of the thermal and condensed fraction, a modified bimodal fit was implemented, allowing independent identification of the centers of mass of the Gaussian and inverted-parabola profiles.
In Fig.4.19(a,b) the horizontal axis corresponds to the holding time t_{hold}, normalized with respect to the specific axial trap period.

BEC behavior   The behavior of the condensed fraction is similar in both cases, showing a persistent spin oscillation, not only in the case of a collisionless regime
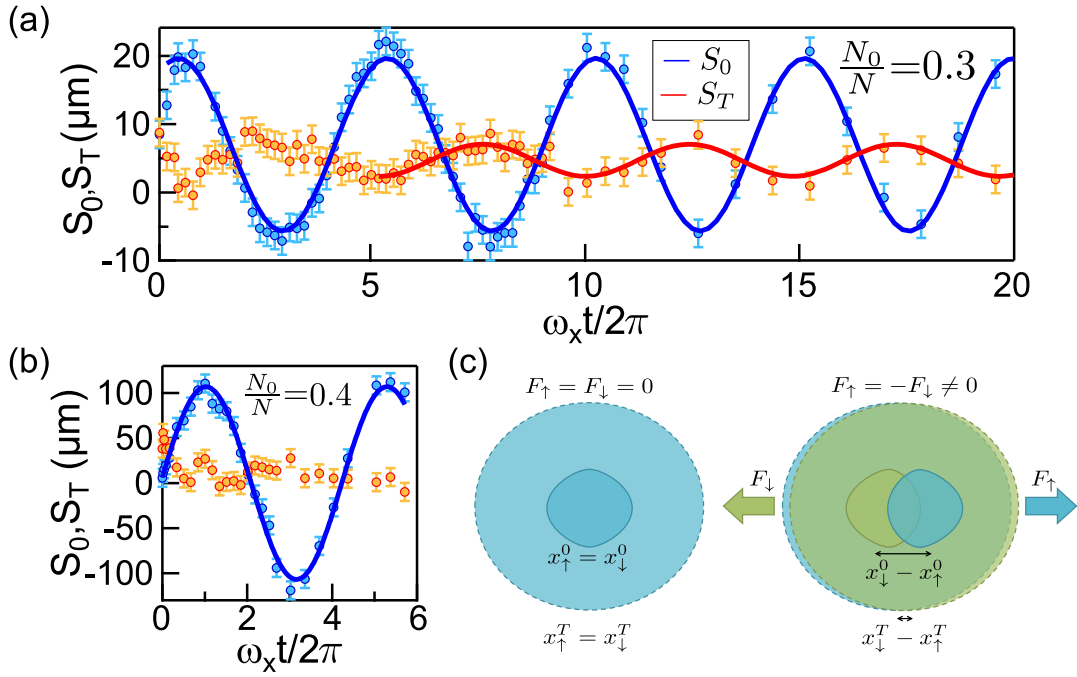
Figure 4.19: (a) Spin-dipole oscillation of the condensed S^0 (blue) and thermal S^T (red) part in the collisionless regime for a mixture with $N_0/N = 0.3$. (b) Spin-dipole oscillation of the condensed S^0 (blue) and thermal S^T (red) part in the collisional regime for a mixture with $N_0/N = 0.4$. (c) Sketch of the four-fluid system without (left) and with (right) an external magnetic gradient. The green and blue colors represent the two spin components, while the external larger and internal smaller distributions represent the thermal and condensed part respectively.

but also in the collisional one. The observation of this oscillation in the collisional regime is a proof of the superfluid nature of the spin current. In both cases the value of the SD oscillation frequency is close to the one predicted by hydrodynamic theory for $T = 0$ that, indeed, is independent of the number of atoms and condensate density of the sample. More in detail the measured value are $\omega_{SD}/\omega_x = 0.205(2)$ and $\omega_{SD}/\omega_x = 0.233(5)$ for the collisionless and collisional regime, respecitvely. The slightly higher SD frequency observed in the collisional regime can be ascribed to the large oscillation amplitude, which is $\sim 50\%$ of the Thomas–Fermi radius R_x.

Thermal clouds behavior

The behavior of the thermal clouds is qualitatively different between the two regimes investigated. In the collisionless regime, the spin-dipole displacement S_T of the thermal clouds oscillates at the same frequency ω_{SD} measured for the condensed fraction and presents, after an initial transient, an out-of-phase behavior with respects to S_0. In addition, the oscillation amplitude A_T is smaller than the amplitude of S_0, being $A_T = 0.18(2)A_0$. This out-of-phase oscillation is driven by the mean-field repulsive interaction of the thermal component with the condensate and can be predicted by studying the SD polarizability of the system.

On the contrary, in the collisional regime, the relative motion of the thermal components shows a fast relaxation due to interactions among atoms. This damping happens on a timescale of a few ms, being compatible with the timescale estimated above T_C (see Fig.4.20) and computed theoretically us-

ing Eq.4.9.

Regarding Fig.4.19, it is worth mentioning that the spin dynamics was investigated at different temperatures for both regimes showing no relevant dependence on the condensed fraction. Finally, it is also important to mention that for the collisional configuration, due to the loss mechanism described in the previous section, it was not possible to explore timescales longer than *T > T_C case* 500 ms, which roughly corresponds to one period of the SD oscillation. .

To have an additional proof that two different regimes were investigated, the relative motion of the thermal spin components S_T above T_C was studied (see Fig.4.20).
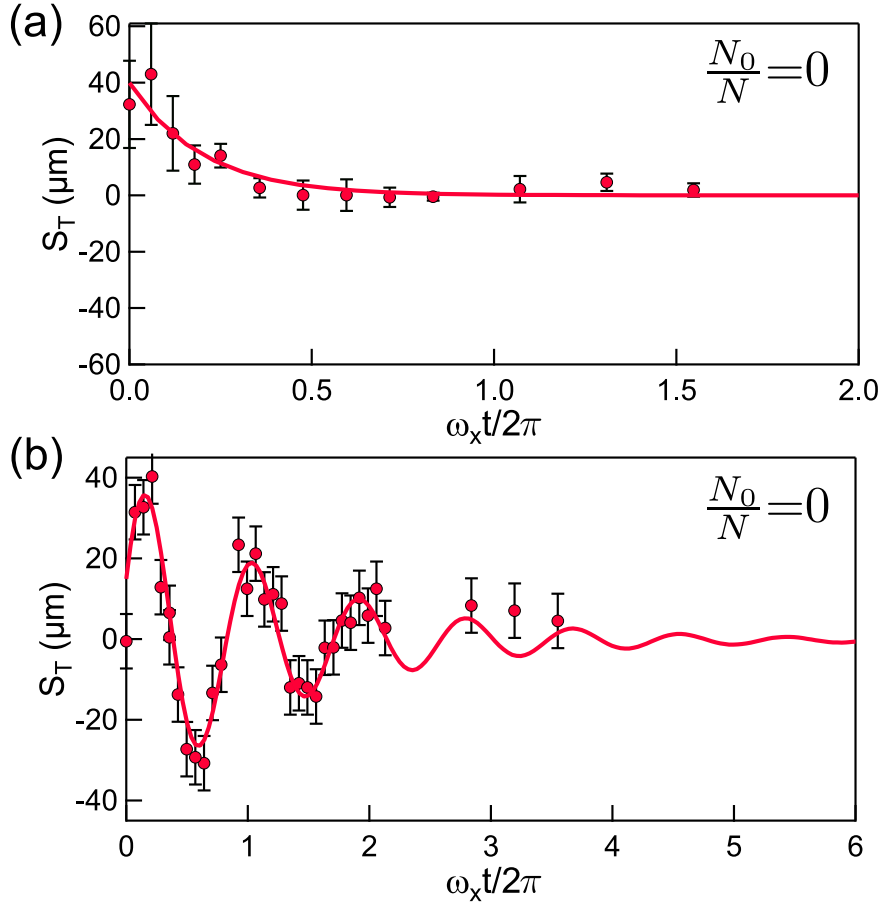

Figure 4.20: Spin thermal current S^T above T_C as a function of the normalized holding time for collisionless (a) and collisional (b) regime.

In the case of collisionless regime the thermal spin current presents several oscillations before being damped, while for the collisional regime an overdamped motion is observed. The collisional times $\tau_{\uparrow\downarrow}$ are obtained from the data using a damped sine and exponential function for the collisionless and collisional regime, being $\omega\tau_{\uparrow\downarrow} = 11(2)$ and $\omega\tau_{\uparrow\downarrow} = 1.2(4)$ respectively. These values are in good agreement with the theoretical estimate that predicts $\omega\tau_{\uparrow\downarrow}$ of a few tens in the collisionless regime and of the order of unity in the collisional one.

Density current In addition, it is important to mention that the density dipole oscillations,*i.e.*, the motion of the center of mass of the condensed and thermal

parts, are not damped in the collisional regime (and also in the collisionless regime). The center-of-mass oscillations are defined as

$$D_0 = x_\uparrow^0 + x_\downarrow^0 \quad \text{and} \quad D_T = x_\uparrow^T + x_\downarrow^T \tag{4.18}$$

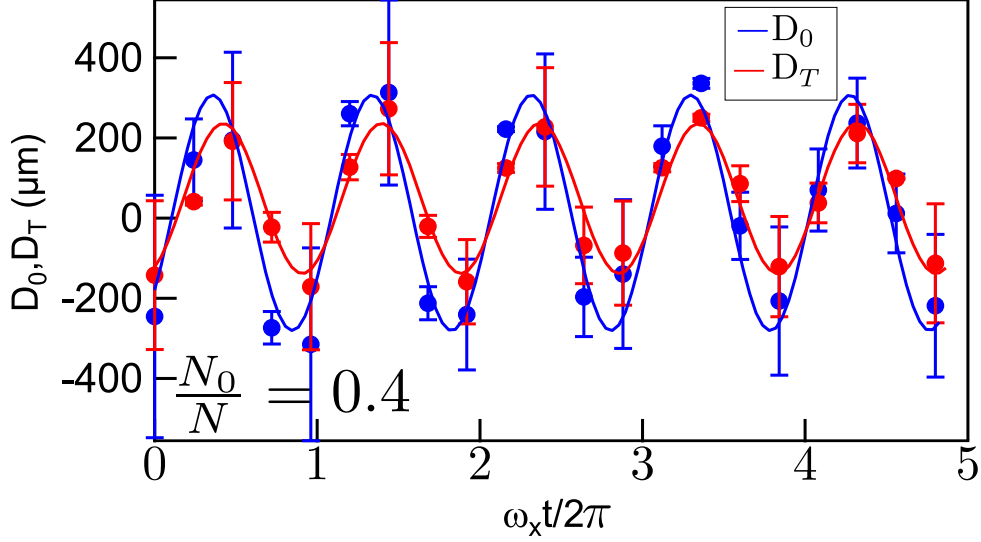for the condensed and thermal part respectively and are reported in Fig.4.21.

Figure 4.21: Center of mass oscillation of the total condensed (blue) and thermal (red) part as a function of the normalized holding time for the collisional regime. Data taken after 7.5 ms of TOF in SG configuration with roughly the same BEC fraction between the two spin components.

As shown in Fi.4.21, the condensed and thermal part oscillate in phase without damping. This means that the overdamped oscillation of S^T observed for the collisional regime is only due to spin drag effect and that it was not ascribable to anharmonicity of the system.

Regarding the spin-dipole oscillation, it is worth mentioning that close to the BEC border, the Landau critical velocity (Subs.1.2.1) is vanishingly zero, being related to the density of the sample. Differently from the the center-of-mass oscillation in the single component case, in our mixture, for small oscillation amplitude, the absence of friction near the BEC border is due to the fact that the spin velocity is strongly suppressed near the surface of the condensate.

Landau critical velocity at the border

4.2.4 Measurement of the static polarizabiliy at finite temperature

Differently from the SD dynamics, the SD polarizability $\mathcal{P}$ shows a temperature dependence, which was investigated both experimentally and theoretically. This temperature dependence is associated to interactions between the BEC and thermal clouds.
A major difference with respect to the $T \sim 0$ case, comes from the need to discern between SD polarizability of the condensed and thermal part. In fact, at finite T, the polarizability of the BEC ($\mathcal{P}_0$) and of the thermal cloud ($\mathcal{P}_T$) show different behaviors.
This set of experimental data was taken only in the collisional regime, while

the theoretical simulations were computed in both regimes, even if no significant difference is expected between the two regimes.

The experimental sequence used to measure the static polarizability is the same as the adiabatic measurement taken in the $T \sim 0$ case, which is explained in Subs.4.1.4. Using the adiabatic procedure, we studied the static SD polarizability at two different condensed fractions, $N_0/N = 0.4$ and $N_0/N = 0.1$. In Fig.4.22 the relative displacement S_0, S_T of the condensed and thermal spin components is reported as a function of the induced displacement of the trap minima.

Regarding the condensed fraction, it is visible that the lower the temperature of the system, the higher the spin dipole S_0. In fact, when $N_0/N = 0.1$, S_0 slightly exceeds $40\,\mu\text{m}$, while when $N_0/N = 0.4$, S_0 is almost three times larger.

By looking at the thermal components, we observed that in both cases the behavior of S_T is deeply different from the one of S_0. In general, the two curves appear flatter and the poor signal to noise prevents a precise estimation of $\mathcal{P}_T$.

From the data reported in Fig.4.22 we extract the value of the SD polarizability by performing a linear fit around the origin. In particular the estimate of the polarizability is done taking into account not only the uncertainty of the linear fit, but it includes statistical and systematic errors, as well as the uncertainty in the estimation of the linear region. Eventually, the SD polarizabilities were estimated as $P_0 = 58(6)$ and $P_T = -3(3)$ for the $N_0/N = 0.4$ case. From the analysis at $N_0/N = 0.1$ instead, we found $P_0 = 19(3)$ and $P_T = 0(2)$. The total polarizability P_{tot} can be computed considering that

$$P_{tot} = \frac{N_0 P_0 + N_T P_T}{N}. \tag{4.19}$$

The estimated value of P_0, P_T and P_{tot} can be compared with the theoretical simulation only for the case of $N_0/N = 0.4$. In fact, when the temperature increases the Thomas–Fermi radius shrinks and, when the system is close to the critical temperature, the size of the BEC is comparable to the spin healing length ζ_s (see Sec.1.2), so that our theoretical predictions are no longer reliable. Although a direct comparison between theory and experiment in the case of $N_0/N = 0.1$ is not possible, it is worth to underline that when the system reaches the critical temperature, it is expected to behave like a non-interacting system, whose polarizability is equal to 1. This is consistent with the reduction of the polarizability observed approaching T_C from below.

In Fig.4.23 the comparison between the experimental data of the polarizability contributions at $N_0/N = 0.4$ and the theoretical simulation calculated at $x_0/R_x = 0.001$ for the collisional and collisionless regime is reported.

As it is visible, the experimental points are in agreement with the theoretical prediction. Unfortunately, it was not possible to experimentally explore a wider range of temperature due to some issues which are discussed at the end of this subsection.

Even more than the agreement between theory and experiment, what is surprising in Fig.4.23 is the increase of P_0 as a function of T. This unexpected behavior can be understood considering that when rising the temperature,
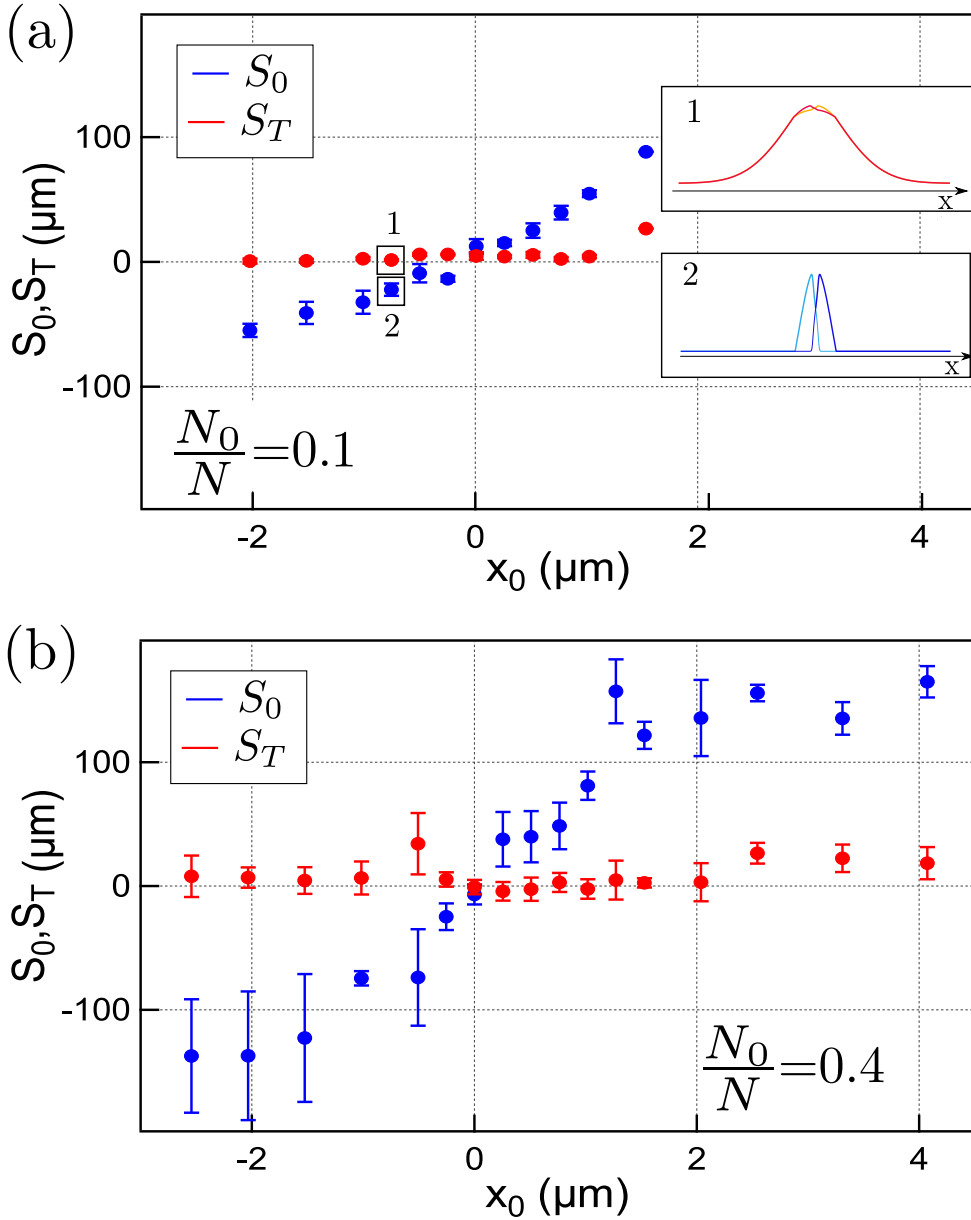
Temperature dependence and thermal contributions

Figure 4.22: Spin displacements S_0, S_T for the thermal (red) and condensed components (blue) of the mixture as a function of x_0 for $N_0/N = 0.1$ (a) and $N_0/N = 0.4$ (b) measured in the collisional regime. Each data point is the average of five different measurements and the error bar is its relative standard deviation. From these data, we extract the value of polarizability P_0, P_T performing a linear fit in the linear region around the origin. In (a) the inset reports the atomic density distributions $n_{\uparrow\downarrow}(x, 0, 0)$ are reported for the [1] thermal and [2] condensed atoms.

interactions between thermal and condensed atoms are no longer negligible. In addition to this phenomenon, another relevant aspect was highlighted by the theoretical simulations and regards the behavior of the thermal atoms. In fact, from Fig.4.23, it is clear that the polarizability of the thermal component is negative and increases with temperature. In fact, it turned out that the polarizability of the thermal fraction depends on the overlap with the condensate (Fig.4.24). For this reason, we distinguish between the region of overlap
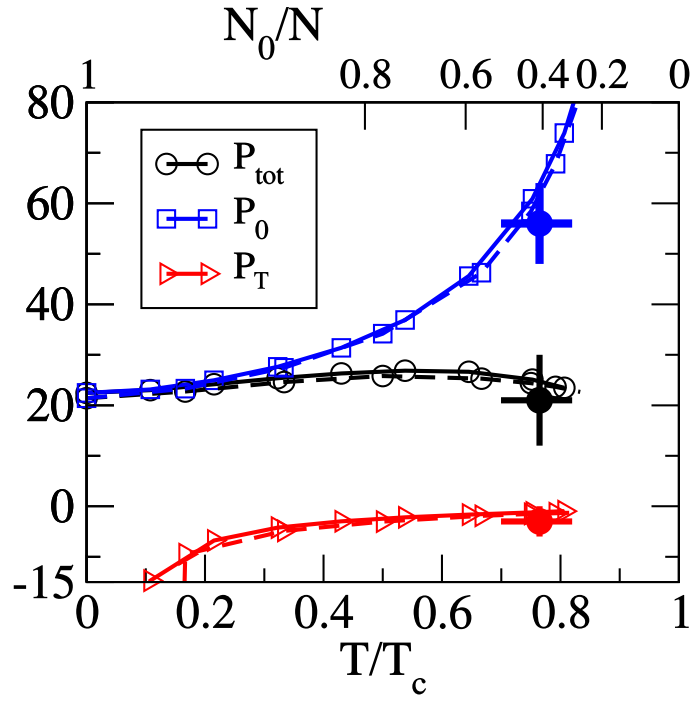
Figure 4.23: Theoretical and experimental static spin-dipole polarizability as a function of temperature of the the superuid (blue), the thermal component (red) and the total component (black). The theoretical calculations were performed for the collisonless (solid) and collisional (dashed) regime. The static polarizabilities measured for $N_0/N = 0.4$ are shown (solid dots) and well agrees with the predictions of theory.

and non-overlap by labeling them as *IN* and *OUT*, respectively. The static polarizability of the internal and external thermal distributions are reported in Fig.4.24 for the case of $x_0/R_x = 0.001$. From the figure it is visible that the polarizability of the external atoms is positive and it is close to $P_{OUT}^{Th} = 1$. On the contrary, the polarizability of the internal atoms is negative and its absolute value is not close to 1. This is in agreement with what reported in Eq.1.65, where it is shown that the spin polarization of the internal thermal distribution is enhanced by the same interaction factor $(a + a_{\uparrow\downarrow})/(a - a_{\uparrow\downarrow})$ affecting the condensed atoms. The total thermal polarizability reported in Fig.4.23 is thus obtained as

$$P_T = \frac{N_T^{IN} P_T^{IN} + N_T^{OUT} P_T^{OUT}}{N_T} \tag{4.20}$$

From the analysis of the thermal polarizability, it is possible to explain why, in the collisionless regime, an out-of-phase oscillation was observed. In fact, considering that the polarizability of the BEC and the whole thermal distribution have opposite sign, their response to an external perturbation is also opposite, leading to the observed out-of-phase oscillation (Fig.4.19). In principle, only the $_{IN}$ thermal atoms are expected to show an out-of-phase oscillatory behavior, which is induced by the presence of BECs. However, experimentally it is not possible to discern between *IN* and *OUT*.

It is important to underline that the role played by the interaction among thermal and condensed atoms become less and less important at larger trap
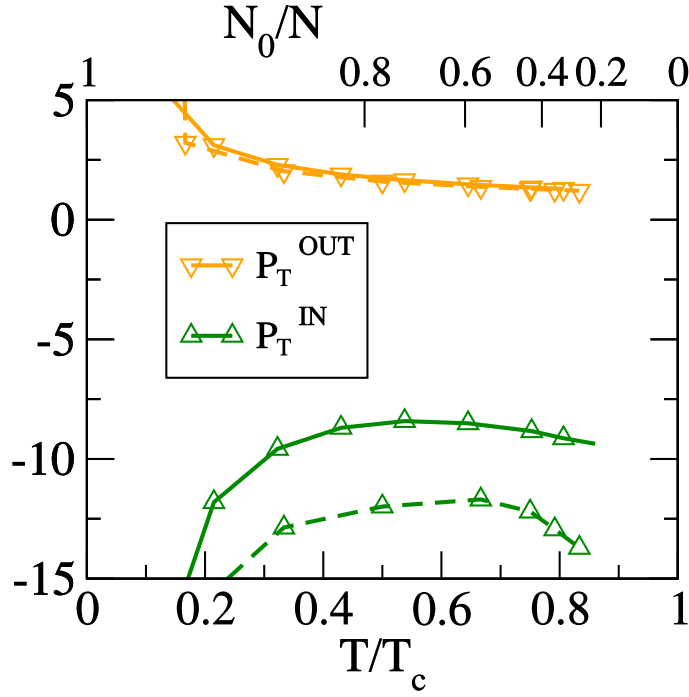
Figure 4.24: Computed spin-dipole polarizability of the thermal atoms inside (green) or outside (yellow) the region occupied by the BEC. The theoretical calculations were performed both for collisonless (solid) and collisional (dashed) regime. The collisional regime shows an higher absolute value of $\mathcal{P}_T^{IN}$ due to the higher density of n_T.

minima displacement (see Fig.1.4), since the role played by interactions decreases.

Finally, I want to mention that two main issues made difficult to acquire extensive experimental data at finite temperature. One regards the atoms redistributions after the creation of the binary mixture explained in Subs.1.2.4, since in the collisional regime the total number of atoms captured by the dipole trap is relative small, the highest condensed fraction achievable is about 50%.

Relevant issues

The second aspect regards the dimension of the system. In fact, in the single-beam configuration the system presents an aspect ratio $\omega_\perp / \omega_x$ 100. In such a situation, probably due to phase fluctuations along the BEC extension, interference effects appeared and affected the imaging, making difficult a clear signal detection.

5 | MAGNETIC SHIELD

Contents

One goal of my PhD research was to develop a magnetic shield that will be used to perform new classes of experiments with ultracold gases in a magnetically controlled environment. An example of experiments of this kind is represented by studies of two-component BECs in different internal states in the presence of coherent coupling. In order to preserve coherence in time between the two states it is essential to stabilize the magnetic field so that the coupling frequency is maintained on resonance with the atomic system. In our case, the coupling will act on the $|F = 1, m_F = \pm 1\rangle$ spin states of sodium, whose Zeeman separation at low magnetic field is equalt to $2 \cdot 700\,\mathrm{kHz/G}$. Since we need to investigate the system for hundreds of ms, therefore the field stability in the atomic region should be better than tens of μG.

Before choosing the final shield geometry, several theoretical studies were done via finite element numerical simulations. From these simulations, we studied the effect of different parameters characterizing the shield and, finally, we chose the shield geometry.

The chapter is divided into two parts. The first part, which includes Sec.5.1 and Sec.5.2, is devoted to the theoretical description of magnetic shielding and to an overview on passive shielding.

The second part, which is composed of Sec.5.3 and Sec.5.4, is devoted to the practical realization of the shield. Here, both requirements that the shield must fulfill and results of simulations are reported. Finally, at the end of the chapter, the chosen design and its theoretical shielding efficiency are presented.

5.1 INTRODUCTION TO MAGNETIC SHIELDING

The need to work in the presence of a stable and well-controlled magnetic field is the key ingredient of many experiments in a wide range of scientific area. Atom interferometry and microgravity [127, 128], ultra cold atomic physics [129, 130, 131], electron microscopy [132] and nuclear magnetic resonance [133] are just few examples of experiments in which a control on external magnetic fields is required. The control should guarantee attenuation and stability against the Earth's magnetic field and residual magnetic fields generated by electrical instruments and, more generally, by magnetized objects. The needed level of this control varies depending on the experiments and, usually, ranges from 10^{-3} Gauss to 10^{-6} Gauss. In general, two different types of magnetic shielding can be distinguished: active and passive.

Active and passive magnetic shielding

Active magnetic shielding is based on the use of electromagnets to generate a magnetic field opposite to the unwanted one. It has the advantage to have a low cost and a light weight but, it requires a real-time and accurate magnetic field monitoring which can be difficult to implement.

The passive magnetic shielding is based on the use of materials having a large magnetic permeability μ_r that offer a preferential path along which the magnetic field can flow. They present the advantage of being high-performance and easy to use, but they are generally expensive and bulky.

Both these shielding techniques can be successfully used to control static or oscillating magnetic fields. However, in the case of passive magnetic shielding, the choice of the material depends on the type of field to screen (see Sec.5.2).

We chose to build our magnetic shield by means of passive magnetic shielding (keeping the option to add active stabilization in the future), thus, in the following, I will focus my attention on this technique.

5.2 PASSIVE MAGNETIC SHIELDING

Passive magnetic shielding requires different materials depending on the frequency of the magnetic field to attenuate. Usually, DC or quasi-static magnetic fields (up to a few hundreds of Hz) are screened using high magnetic permeability materials, while for AC fields (from kHz or higher frequency) highly conductive material are recommended.

Depending on the material parameters two different shielding mechanisms can occur, namely flux shunting and eddy-current cancellation.

When dealing with the flux-shunting technique, the spatial distribution of the magnetic field is modified and the lines of the magnetic induction are moved away from the shielded region. The distortion of the magnetic field distribution depends on the material physical parameters, the shield geometry and the frequency of the magnetic source.

DC shielding mechanism

The flux-shunting mechanism is related to the behavior of the magnetic field $\vec{H}$ and of the magnetic induction (or flux density) $\vec{B}$, which is gov-
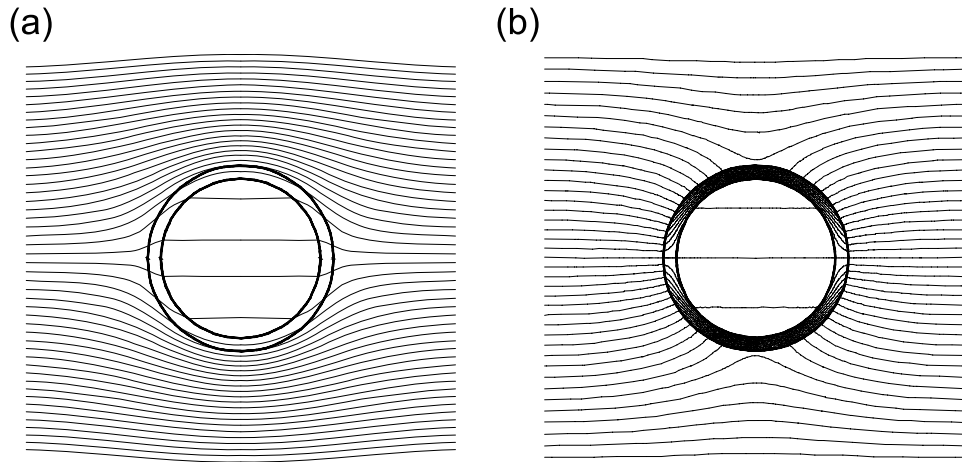
(a)

(b)

Figure 5.1: Magnetic field distribution at the interface between air and a cylindrical highly-conductive (AC) (a) and ferromagnetic (DC) (b) shield in the case of uniform external field. Images from [134].

erned by Maxwell equations. For a linear, homogeneous, isotropic, and non-dispersive material the constitutive relation which links $\vec{H}$ to $\vec{B}$ is

$$\vec{B}(\vec{r},t) = \mu\vec{H}(\vec{r},t) = \mu_r\mu_0\vec{H}(\vec{r},t), \tag{5.1}$$

where μ_0 and μ_r are the magnetic permeability of vacuum and of the material, respectively. Ampere's and Gauss's laws require that, in absence of currents, the tangential component of $\vec{H}$ and the normal component of $\vec{B}$ are continuous across material discontinuities. To satisfy these requirements, at the interface between different media, both the magnetic field and the magnetic induction can change their direction abruptly. Let us use Fig.5.1(b) as a reference, where the case of air-ferromagnetic interface is considered (for more detail on ferromagnetism see Subs.5.2.2). On the air side, the magnetic field is pulled toward the ferromagnetic material nearly perpendicular to the surface. Since the normal component of $\vec{B}$ must be the same in the two media, due to the high permeability of ferromagnetic materials the magnetic field penetrates nearly tangential into the shield. The higher the value of μ, the stronger the bending of the magnetic induction, hence the shielding efficiency [134, 135].

Since the relative permeability of the ferromagnetic materials decreases as a function of the field frequency, this technique is particularly suitable in case of DC or low-frequency fields (up to a few hundreds of Hertz as shown in Fig.5.2). In addition, another factor that influences the shield performance is its geometry, which is the main topic of Sec.5.4.

The eddy-current cancellation mechanism is related to the presence of a time-dependent magnetic field and an highly-conductive material. According to Faraday's law, an AC magnetic field induces an electric field which, in the presence of a conductive medium, can produce electric currents known as eddy currents. These currents give rise to a magnetic field opposite to the incident one, so that the general result is the forcing of the magnetic field to run parallel to the surface of the shield (Fig.5.1(a)). Note that this mechanism occurs in any electrically conducting material, regardless of its
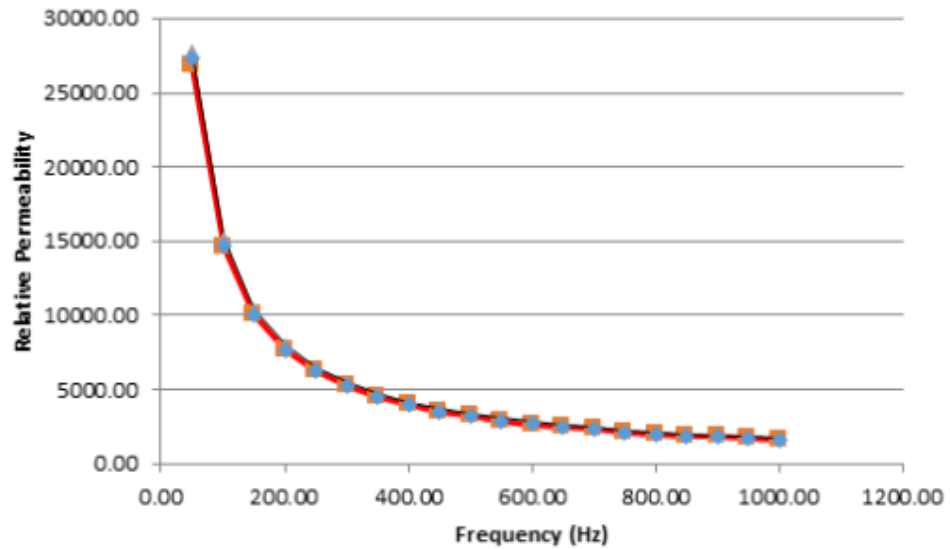
AC shielding mechanism

Figure 5.2: Image from [Magnetic Shield Corp.] showing the response of the relative permeability of a Mu-Metal toroidal core as a function of frequency. This frequency response should not be construed as the general response of the material, since it can changed depending on the geometry of the core and on the external magnetic field.

magnetic properties. In addition, the boundary conditions to satisfy in this framework are opposite to the DC case, being the normal component of $\vec{H}$ a conserved quantity.

In general, the thickness of the shield is a fundamental parameter which should be compared with the skin depth δ, for instance in the AC case. The skin depth corresponds to the characteristic length at which the magnetic induction can penetrate into the material before being suppressed by eddy currents. Efficient magnetic shielding can occur only if the thickness of the shield is larger than the skin depth and, since the inductive coupling with the AC field is proportional to the area which intercepts the source flux, a better performance is expected for larger shields (at fixed thickness).

Since we are mainly sensitive to DC and low-frequency (up to a few tens of Hz) magnetic fields, our shield is composed of high magnetic permeability material, whose characteristics are described in the next sections as well as some issues relevant for DC magnetic shielding. In addition, considering that the coherent coupling between the spin states will be of the order of a few hundreds of hertz, the relevant timescale for temporal fluctuations is of the order of a few tens of ms so that we can assume that the shielding efficiency is essentially unchanged (see Fig.5.2).

5.2.1 Magnetic shield shapes performances

One crucial aspect which determines the efficiency of a magnetic shield is its shape. In general, the design of a magnetic shield should be realized taking into account the specific requirements of an experiment. Thus, it is not possible to define a geometry which fits for every situation and a careful investigation via numerical simulations should be performed (see Sec.5.4).

However, it is possible to identify some general guidelines to help in defining the best shield design for a specific experiment.

The ideal shape of a magnetic shield is a sphere or an infinitely long cylinder. This is because having sharp corners can lead to flux leakage into the shield itself. Then, creating shields with rounded edges is always recommended.

Rules of thumb

Another general rule concerns the use of shields as small as possible. In fact, for a spherical or cylindrical shield, the attenuation scales as the inverse of the shield radius at fixed thickness. This is related to the fact that increasing the size also the amount of magnetic flux density collected by the shield increases. Thus, instead of increasing the size of the shield, it is preferable to increase its thickness (see Eq.5.2).

Another recommendation regards the manufacturing of continuously extended shields. When conditions make it impossible to use a single-piece shield, continuity at corners and transitions should be maintained either mechanically with good overlapping contact or through welds.

In addition, the presence of opening and holes is always discouraged since magnetic field can penetrate trough them. Generally, magnetic fields can travel into an opening up to five times the diameter of that opening [Amuneal] and, if it is not possible to ensure a close shield design, some precautions can be taken to minimize the magnetic field penetration in the internal volume. For example, in case of open ends in a cylindrical shield, the length of the shield can be increased in order to maximize the length-diameter ratio.

Similarly, it is possible to add collars around all openings. The length of these collars should be at least equal to the diameter of the hole and in general the longer the better.

Since it is generally difficult to design a shield which satisfies all the properties listed above, a popular strategy is to employ a multi-layer shield. In this way, the effect of the outer layer is to weaken the magnetic field so that the inner layer exhibits a better performance. The total results is that the whole efficiency of a multi-layer shield is higher than the sum of the efficiencies that would be associated to each single layer. In fact, in first approximation, the transverse attenuation of a single cylindrical layer is

Multi-layer shield

$$A_{single} = \frac{\mu_r t}{2R} \quad , \tag{5.2}$$

where μ_r is the relative permeability of the material, t is the cylinder thickness and R its mean radius. In the case of a multi-layer shield with n layers, Eq.5.2 becomes

$$A_{multi} = A_n \prod_{i=1}^{n-1} A_i \left[1 - \left(\frac{R_i}{R_{i+1}} \right)^2 \right], \tag{5.3}$$

where A_i is given by Eq.5.2 [136].

A similar shielding attenuation behavior is expected longitudinally to the shield, where the attenuation can be computed as [137, 128]

$$A_{multi} = A_n \prod_{i=1}^{n-1} A_i \left[1 - \left(\frac{L_i}{L_{i+1}} \right) \right], \tag{5.4}$$

where L_i is the length of the i-th cylinder.

As anticipated before, these are simply general limits and formulas that should be kept in mind when designing the shield. Anyway the final design should be chosen only after having performed simulations to highlight the effect of each parameter of the shield in the specific experimental case.

5.2.2 Materials

When dealing with DC (or low-frequency) magnetic fields, the best shielding performance is reached using high permeability materials. The magnetic permeability defines the ability of a material to support a magnetic flux density $\vec{B}$.

Usually three different classes of materials can be distinguished, depending on the value of μ_r:

- diamagnetic: $\mu_r < 1$ and small in modulus;

- paramagnetic: $\mu_r > 1$ and small in modulus;

- ferromagnetic: $\mu_r > 1$, non linear and generally large in modulus.

Since we are interested in having a large μ_r, we will focus our attention to ferromagnetic materials.

Ferromagnetic materials properties   Ferromagnetic materials are characterized by a magnetic permeability which changes depending on the modulus of $\vec{H}$ and by the presence of a residual magnetization M_r when the external field is turned off, thus, Eq.5.1 can be rewritten as

$$\vec{B} = \mu_0 \left(\mu_r(H)\vec{H} + \vec{M} \right) \tag{5.5}$$

The non-linear behavior of μ_r and the residual magnetization M_r are visible from the hysteresis cycle, which represents the response of the material to an external magnetic field (see Fig.5.3). Another relevant property of ferromagnetic material is the saturation threshold, which corresponds to the maximum flux density that can be sustained by the material. Microscopically the saturation regime corresponds to the situation in which all the magnetic domains of the material particles are aligned with the external field.

A few examples   Among all ferromagnetic elements and alloys, one of the most common material used for magnetic shielding is Mu-Metal, which is a magnetically soft[1] alloy. It is composed of 80% of nickel, 5% of molybdenum and iron to balance. This material saturates at 0.75 T (80 A/m) and it has a magnetic permeability of 470000 at 0.4 A/m [Magnetic shields]. Mu-Metal permits to reach high shielding efficiency but it saturates with quite small magnetic fields.

A material which presents a smaller permeability, but saturates less easily is Supra-50. It is an alloy composed of 48% of nickel and 48% iron. It saturates at 1.5 T (800 A/m), has a maximal magnetic permeability of 200000 and, compared to Mu-Metal, is magnetically less soft.

Annealing procedure   In general, the performances of ferromagnetic materials are highly sensitive to the history of the material itself. For this reason, to guarantee the best

---

1 A material is said magnetically soft when the coercive field required to cancel the residual magnetization is small.
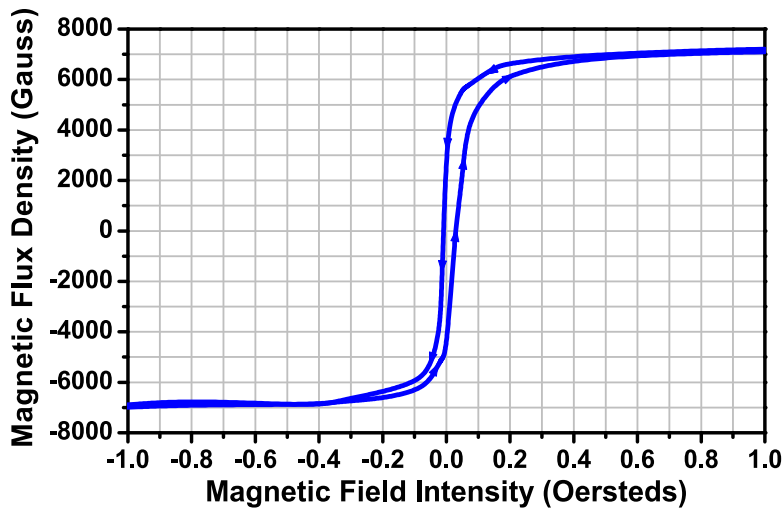
Figure 5.3: Experimental hysteresis curve of a Mu-Metal foil taken from [Thorlabs].

magnetic permeability, an annealing procedure is recommended after manufacturing. This procedure consists of a heat treatment up to 1200°C performed in a controlled environment (typically Hydrogen) able to alter the micro-structure of the material and to relieve any residual tension. In fact, the permeability of these materials is extremely sensitive both to elastic and plastic strain. In case of elastic strain, which corresponds to a distortion of the crystal lattice, a sequence of demagnetization procedures (see Subs.5.2.3) can be enough to restore the original performance. Instead, when a dislocation of part of the crystal lattice occurs (plastic strain), a new annealing procedure should be applied.

5.2.3 Degaussing

Ferromagnetic materials are characterized by the presence of a residual magnetization M_r even when no external magnetic field is applied. Since this magnetization can reduce the performance of the shield, a procedure to suppress M_r is generally required. The most common procedure used goes by the name of degaussing or demagnetization. The basic idea of degaussing is to gradually decrease the magnetization of the material by means of an oscillating external magnetic field, whose amplitude is gradually reduced to zero as sketched in Fig.5.4.

The ideal degaussing procedure requires to have no surrounding magnetic fields and no magnetic part inside the shield. It also requires that the oscillating magnetic field runs along a close pathway in the material to treat, since surface degaussing is not so efficient. This last requirement can be satisfied, in the case of cylindrical shields, by wounding a coil (degaussing coil) around the long axis of the shield itself. In the case of multi-layer shields, it would be preferable to wound a coil around each layer and when, for different reasons, it is not possible to degauss separately each layer of the shield, it is recommended to degauss at least the innermost layer [128].
The degaussing electromagnets must be supplied with alternating current such that the produced magnetic field is strong enough to reach the satura-
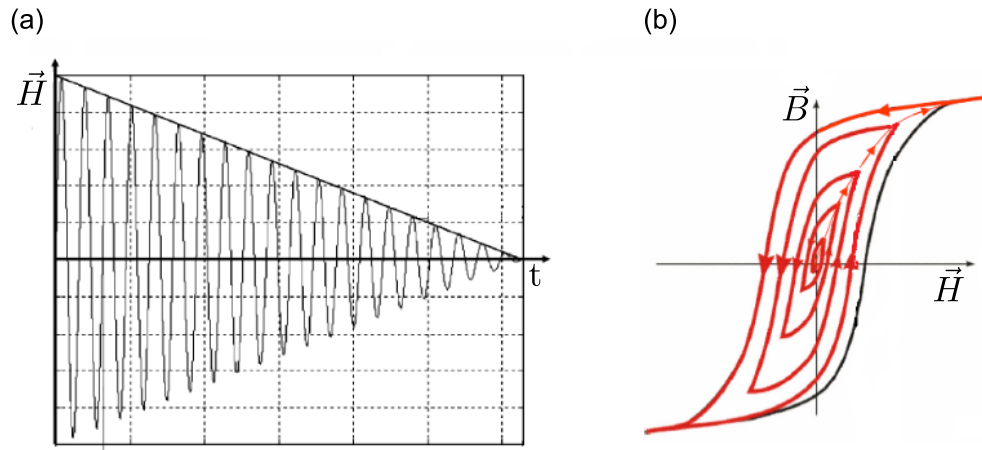
(a)

(b)

Figure 5.4: (a) Oscillating magnetic field $\vec{H}$ gradually reduced to zero. (b)Hysteresis loop of the material during the degauss procedure. Picture (a) from [138] and picture (b) from [139].

tion regime. Then the current intensity must be turned down to zero slowly enough to ensure that the magnetic domains react to the applied magnetic field.

From a microscopic point of view, degaussing works as follows: initially, above the saturation threshold, all magnetic domains are aligned with the magnetic field. Then the alternating magnetic field changes the orientation of all domains which will start to have a random orientation since they respond to different field intensities. As a result, when $\vec{H}$ is zero, the residual magnetization $\vec{M}_r$ will be zero as well.

In our shield, a specific aperture to host the degaussing coil cables was designed in order to guarantee the possibility of degaussing the material, as well as to have an access for antenna and electromagnets cables.

5.3 SHIELD CONSTRAINTS

In the previous section, the main features concerning passive magnetic shielding were presented. It was pointed out that, even if some general guidelines can be followed, a good approach consists in performing simulations to find out the best shield design for a specific experiment given the specific constraints imposed by the experimental setup and the goal of the experiment. In our case the final goal of the shield was outlined at the beginning of the chapter, while the experimental setup constraints are reported in the following.

In this section, all mandatory characteristics that our shield should have are described.

Experimental setup geometry   The main geometrical constraints come from the design of the UHV chamber which hosts the atomic sample. This UHV cell is a quartz octagonal shaped cell which is sustained by a horizontal tube of 12.5 mm radius and about 80 mm length, directly connected to the main vacuum apparatus (see
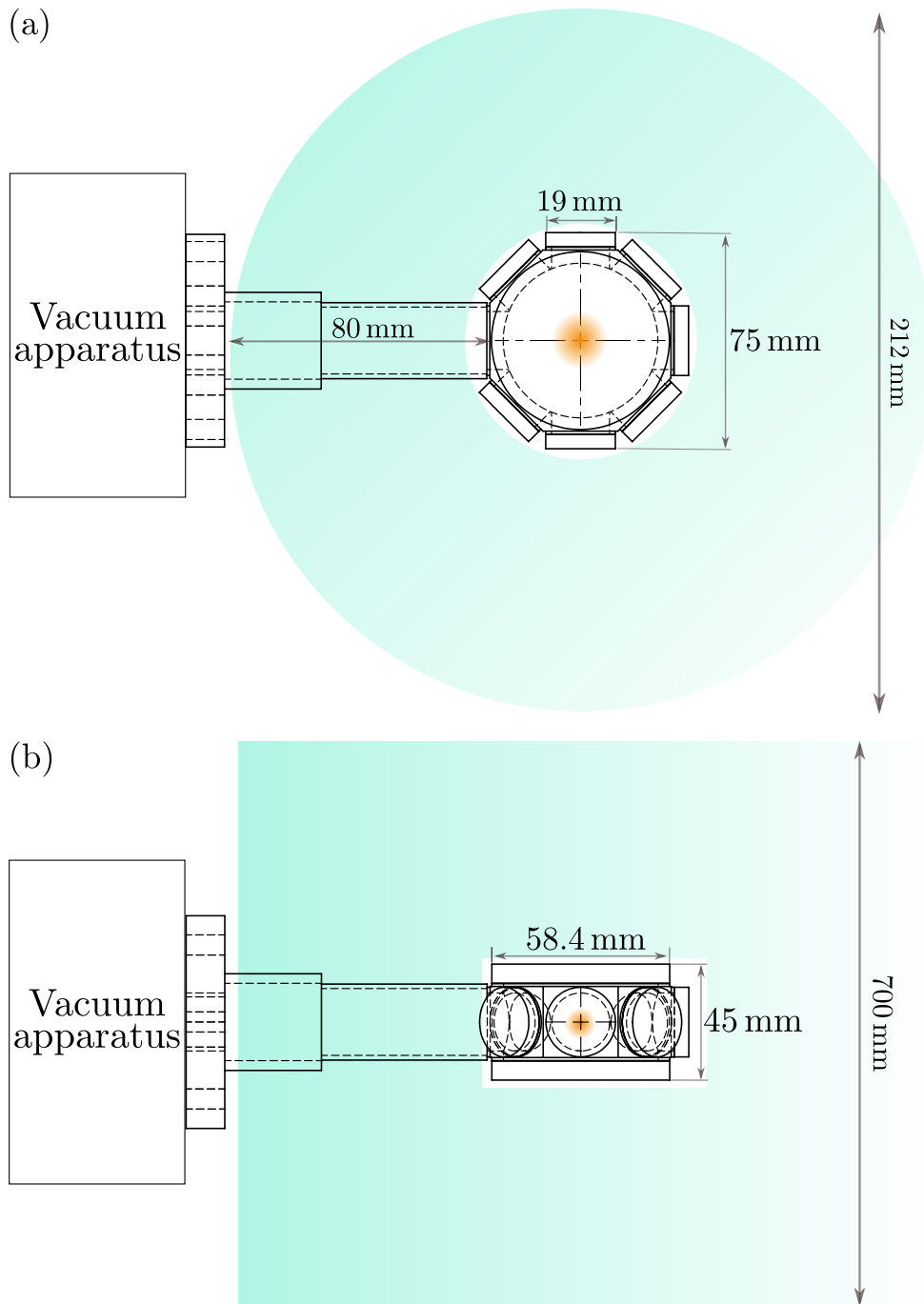
Figure 5.5: Top (a) and side (b) view of the quartz cell. In both cases the orange spot represents the region of $\sim 1\,cm^3$ where the atoms are collocated. In addition the area where the magnetic shield could be located is highlighted in azure.

Fig.5.5). One of the eight flat side faces of the cell is welded to the tube used to support the cell itself, while the remaining seven faces have a 19 mm diameter window each. Two extra 58.4 mm diameter windows are located at the top and at the bottom of the UHV cell. The seven small windows are 4.8 mm thick, whereas the two largest windows are 7.8 mm thick to prevent the window stress induced by atmospheric pressure. Since the BEC, whose typical extension is of a few hundreds of μm, will be created at the center of the quartz cell in a region of about 1 cm^3 (the region of interest), all the windows have anti-reflection coating (R$\sim$ 0.02% on the spectral range 500 $\div$ 1100 nm) on both sides in order to guarantee an excellent optical access of the laser light. The outer distance between two parallel faces is about 75 mm, while the distance between the center of the UHV cell and the edge of the vacuum apparatus (up to the head of the screws used to fix the flange on which the quartz tube is mounted) is about 106 mm. Thus, to have the region of interest at the center of the shield, the smallest radius of the shield can be $r_{min} = 38$ mm and the largest $r_{max} = 105.5$ mm.

For what concerns the height of the shield the only limitation is given by the presence of the optical table on which the vacuum apparatus is mounted, which is 350 mm below the center of the quartz cell. Thus the total height of the outermost cylinder should be smaller than 700 mm.

Optical access   In addition to the geometrical constraints imposed by the setup geometry, there are further constraints imposed by the experiment that we want to perform with the magnetic shield. In fact, since we want to study BECs, we need to have an optical access to manipulate and probe atoms. This optical access can be provided by the presence of holes in the shield. The position and size of the optical apertures were chosen by considering the experimental sequence that we will employ during the experiment. In particular, a set of ten apertures is implemented in the shield design and, since the largest beam that we plan to use is 12.5 mm radius, all holes have a diameter of 30 mm (taking into account the extra space needed for the optics supports). Two apertures are along the vertical symmetry axis, while the others are located along the circumferences of the shielding layers displaced by 45° one from the other and they are centered at half the height of the shield. One of these apertures is meant to enclose the glass tube which connects the UHV cell to the vacuum apparatus.

Degauss   Another aspect to be taken into account for the shield design is the possibility to perform a degauss procedure (see Subs.5.2.3 and to send RF and μ-wave signals thanks to specific antennas. Thus, an additional pair of apertures is included in the shield design in order to guarantee an access to the cables of the degaussing electromagnets and the antenna's cables that will be placed around each shielding layer. These two holes, whose diameter is 10 mm, are located at the top and at the bottom of the shield being slightly displaced with respect to the circumference's center.

Internal electromagnets   Finally, a crucial requirement for the realization of the experiment is the presence of (at least) a pair of electromagnets inside the shield. These electromagnets, whose internal radius is 46 mm, are used to generate either a quadrupole magnetic field (for the MOT) and a uniform magnetic field (for instance to define the quantization axis and fix the Zeeman splitting). They are placed around the two vertical large windows of the UHV cell. These

electromagnets will be used during the experimental sequence to produce a static field of about $0.1\,\text{G}$ and a magnetic gradient of more than $20\,\text{G/cm}$. The presence of the electromagnets plays a crucial role on the final design of the magnetic shield since the saturation threshold of the innermost layer could be reached causing a decrease of the shielding efficiency. Thus, specific simulations on the effect of internal magnetic fields and gradients were performed (see Subs.5.4.3).

5.4 FINITE ELEMENT METHOD SIMULATIONS

In this section I present the all simulations performed in order to find the best design, which should be able to satisfy all our requirements and constraints. Studying individually the role played by different parameters, it was possible to design a magnetic shield that according to the simulations will guarantee a stability of the magnetic field in the range of micro Gauss through the attenuation of external perturbations by more than four orders of magnitude.

5.4.1 Introduction to finite element method (FEM)

The efficiency of magnetic shielding depends deeply on the design of the shield, which can be different from one experiment to the other. The most used procedure to simulate the effect of a given shield, is based on the finite element method[2] (FEM), which is suitable to numerically solve differential equations with boundary conditions and/or initial value problems. The operating principle of FEM is the replacement of continuous functions by piecewise approximations, usually using polynomials. These approximations are done by dividing the region where the differential equations should be solved into several sub-regions called finite elements (or mesh). In case of a 3D simulation, these elements can be tetrahedrons, pyramids, bricks or prisms and the choice of the element shape depends on the geometry of the object to study (see Fig.5.6). Within each element the solution is approximated by a function that depends on its vertex values. The overall solution is determined once all vertex values of the whole system have been found and combined. Proceeding in this way, it is possible to study complex systems, without losing information on local effects. In addition, since each element can be treated independently, different materials and/or physical properties can be attributed to each sub-region.

In our case, the software used to perform simulations is Comsol multiphysics, which permits to simulate a large variety of problems, also taking into account several physical phenomena simultaneously.

5.4.2 Number of layers

As anticipated in Sec.5.2, a way to increase the attenuation efficiency of a magnetic shield is to use a multi-layer geometry. Since we aim to obtain

---

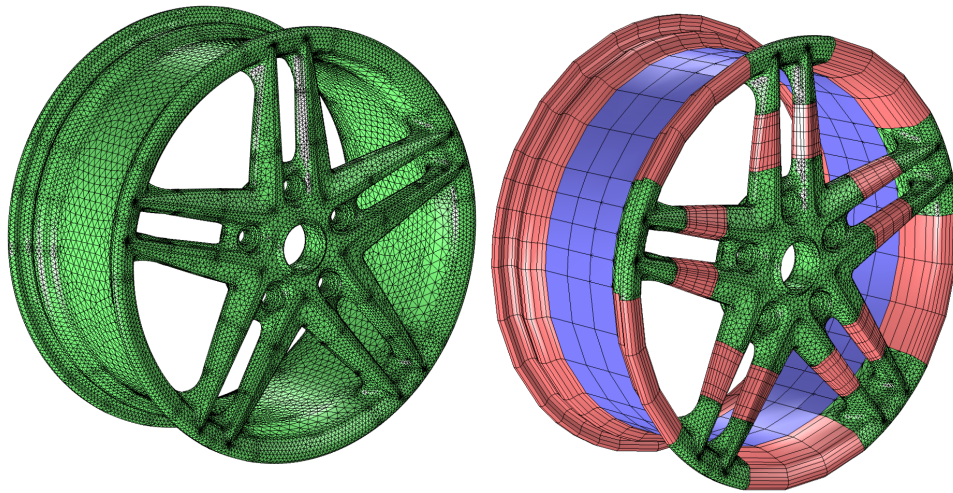2 Sometimes it can be labeled as finite element analysis (FEA).

Figure 5.6: Two different mesh configuration for the same 3D model. On the left only tetrahedrons are used, while on the right a combination of tetrahedrons, bricks and prisms is reported. Image from [Comsol Multiphysics].

a stability of the magnetic field at the level of μG, we planned from the beginning to use a multi-layer shield. In the literature most works report on shields with at least three layers and thus and we opted for a four-layer as configuration. From the simulations it turns out that adding an additional layer, the magnetic attenuation is improved by a factor 3 reported in Fig.5.7. In the figure the value of $|\vec{B}|(x,0,0)$ and $|\vec{B}|(0,0,z)$ are reported in case of an external magnetic field aligned along $\hat{z}$. From this figure, one sees that the effect of the fourth layer is not only of reducing the absolute value of the magnetic flux, but also providing a more uniform field, especially along the horizontal plane. For these reasons, we decided to work with a four-layer configuration. To perform this simulation we use a simplified geometry composed of three or four concentrically cylinders, which are exposed to a uniform magnetic field of 1 G. The innermost cylinder has an internal radius of 60 mm, it is 120 mm high and 1 mm thick. In this simulation, each next layer is increased by 40 mm both in diameter and height. In addition, in order to save computational time and memory, the magnetic permeability of this specific simulation is set to 4000, which corresponds to a conservative value with respect to the actual response of Mu-Metal.

5.4.3 Saturation

To perform the new experiment we need to apply magnetic fields and gradients inside the magnetic shield. This, in general, is not a problem, providing that the intensities of the applied fields are low with respect to the saturation threshold B_{sat} of the material used for the shield. This is a crucial requirement since the high permeability of the medium, hence its screening efficiency, is guaranteed only if $B_{in} < B_{sat}$. We performed several simulations in order to verify this requirement. The goal is to check whether the innermost layer of the shield, which is the one directly exposed to internal
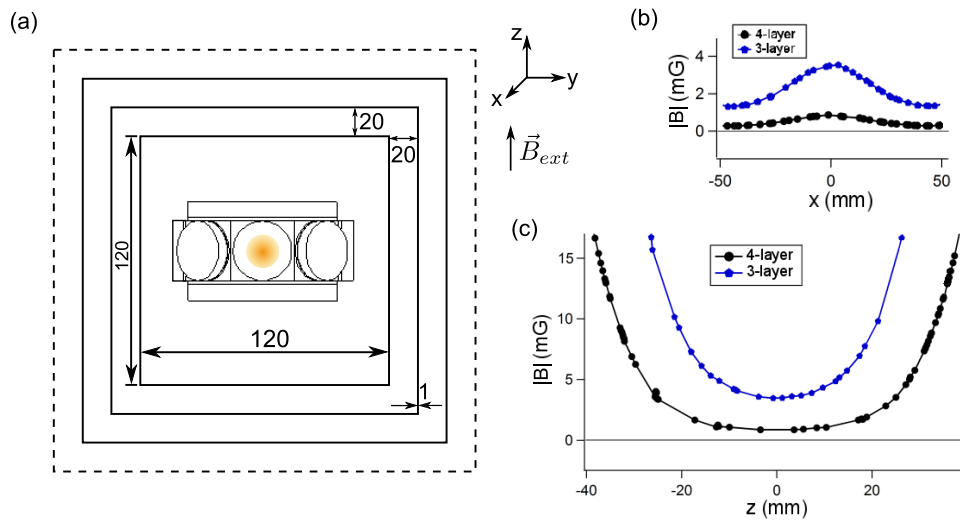
Figure 5.7: (a) Sketch of the shield design used to simulate the effect of the fourth layer (dashed). Magnetic density flux B along $(x, 0, 0)$ (b) and z-component of the magnetic density flux along $(0, 0, z)$ (c) of a (blue pentagons) three and (black dots) four layer magnetic shield with an external magnetic field of $1\,\mathrm{G}$ along $\hat{z}$.

magnetic fields, is able to sustain, without saturating, the magnetic fields that will be applied during the experimental sequence. The role of the thickness and of the distance from the magnetic field source was investigated as well.

From the simulations it is clear that the effect of increasing the thickness of the layer is not only to reduce the value of magnetic flux density flowing in the medium, but also to slightly reduce the sensitivity to the vicinity of the source (see Fig.5.8). In addition, the simulations show that the configuration in which the experiment will be performed can not saturate the innermost layer of the shield, being the maximum magnetic flux propagating in the shield much lower than B_{sat}.

In order to study the role of the thickness and distance from the source, I considered the magnetic field produced by two coils placed around the two vertical windows of the quartz cell having a mean radius and a relative distance of 31 mm, thus able to produce both a quadrupole and a uniform magnetic field. The value of the current flowing in the coils was chosen such that a magnetic gradients of up to $100\,\mathrm{G/cm}$ are created. Then a single cylinder placed around the coils of external height $70\,\mathrm{mm}$, initial external radius of $40\,\mathrm{mm}$ and variable thickness (1 and $2\,\mathrm{mm}$) was modeled. Since these simulations aim to study the saturation level of the shield, the permeability used in this case is the one of the Mu-Metal (Fig.5.3) which depends on the magnetic field $\vec{H}$ applied.

Role of thickness and distance from the source

In this framework I checked the maximum value of the magnetic flux B_{max} flowing inside the shield (in the $\hat{z} = 0$ plane) as a function of the shield's radius for both values of the magnetic gradient. The results obtained are reported in Fig(5.8). From this graph we can extract many information. As expected, increasing the distance between the shield and the magnetic field source has the effect to lower the magnetic flux inside the shield, as well as increasing the thickness. It is interesting to note that the flux is more
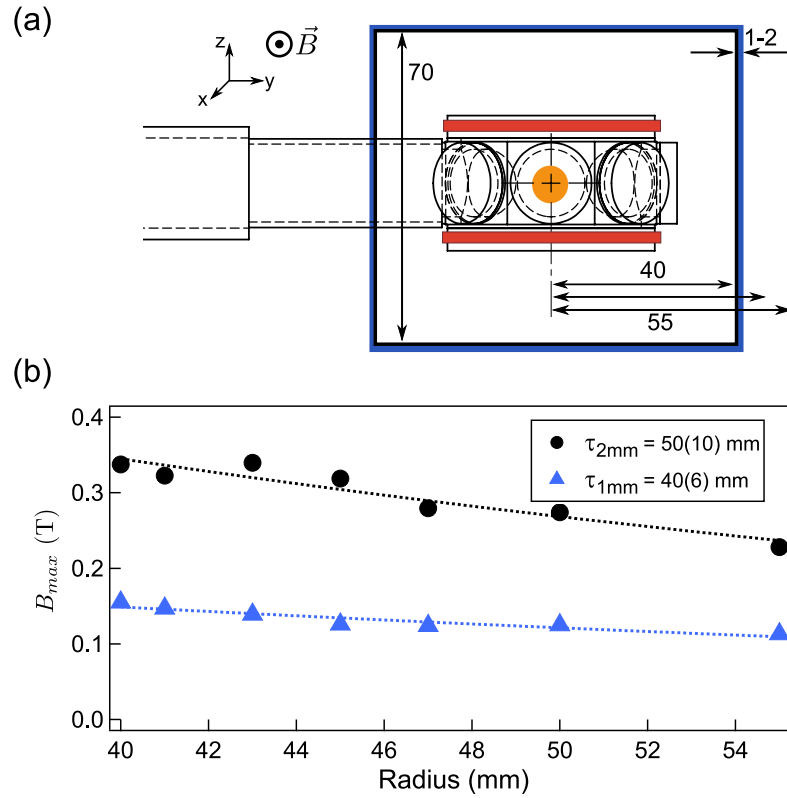
Figure 5.8: (a) Sketch of the shield geometry used to simulate the role of the thickness and the distance from the coils. The two thickness used for the cylinder are 1 (black) and 2 (blue) mm, the height is 70 mm and the radius is varied from 40 to 55 mm (three adjacent arrows). (b) Maximum value of the magnetic flux density B inside the magnetic shield as function of the shield's radius in the $\hat{z} = 0$ plane in the presence of a 100 G/cm magnetic gradient. The black dots refer to the case of 1 mm of thickness, whereas the blue triangles refer to the case of a cylinder 2 mm thick. The solid lines are the exponential fits giving the decays reported in the insert. The value of B_{sat} are ~ 0.7 and ~ 1.5 T for Mu-Metal and Supra-50, respectively.

than halved when the thickness is doubled. For example, when the radius is 40 mm, $B_{max_{1mm}} = 0.33(1)\,\text{T}$ and $B_{max_{2mm}} = 0.15(1)\,\text{T}$ and I recall that the value of B_{sat} is of the order of 0.7 T for Mu-Metal. Moreover the decay rate of the magnetic flux as a function of the radius is higher for smaller thickness. This phenomenon emphasizes even more the importance of having a thicker layer, which can guarantee a better performance for smaller shields.

An additional information obtained by the simulation is the value of $|\vec{B}|$ inside all the shield geometry (thus not only in the $\hat{z} = 0$ plane). For the case of a 1 mm thick layer of Mu-Metal, in the presence of a 100 G/cm gradient, the maximum value of $|\vec{B}|$ was close to the saturation threshold of $B_{sat} \sim 0.7\,\text{T}$. In fact, close to the edge of the cylinder, it was of the order of 0.5 T. Considering that this simulation was performed for a simplified configuration where, for example, apertures were not modeled, we decided to use a different material for the innermost layer: a 2.5 mm thick layer of Supra-50 (see Subs.5.2.2) in order to further suppress saturation problems.

Saturation realistic simulation

In order to verify if the 2.5 mm thick layer of Supra-50 is able to sustain the magnetic field gradient that will be used during the experimental sequence, we performed a more realistic simulation. In particular, keeping fixed the size of the coils, a cylinder of 211 mm height and 54 mm radius was designed. The cylinder was modeled with all 11 apertures as described in Sec.5.3. It was exposed to a magnetic gradient of the order of 50 G/cm, which is higher than the gradient required during the experiment. The result of the simulation is reported in Fig.5.9, where it is reported the value of $|\vec{B}|$ around all the surface of the shield. The maximum value of $|\vec{B}|$ is around 250 G, which is well below the saturation value of Supra-50 ($\vec{B}_{sat} = 1.6\,\text{T}$). Thus, even considering a discrepancy between theoretical simulations and real response of the material, we can consider unlikely to saturate the Supra-50 layer during the experimental sequence.

5.4.4 Inter-layer distance

Another aspect to study is the role of inter-spacing between adjacent layers with respect to the dimension of the innermost layer. In the literature evidence of the attenuation scaling as a function of layer radii is reported in [140]. In this work, which is based on a three-layer cylindrical configuration, authors suggest to use cylinders whose radius is double than the inner one (cylinders whose radius increases by doubling at each layer). Unfortunately, due to space limitations, we cannot adapt this criterion in the radial direction.

However, it is important to remind that in cylindrical shield geometries, the poorer attenuation is expected along the axial direction (see Eq.5.3 and Eq.5.4). For this reason, and since our space constraint in the vertical axial direction are looser, we investigate the role of axial inter-layer distance. In particular, we are interested in understanding the role of initial size of the innermost layer with respect to inter-layer distance.

At first, we have investigated the role of the height of the innermost layer, which is increased in steps of 20 mm, while the inter-layer distance is kept fixed at 10 mm each side. The result of these simulations shows that increas-
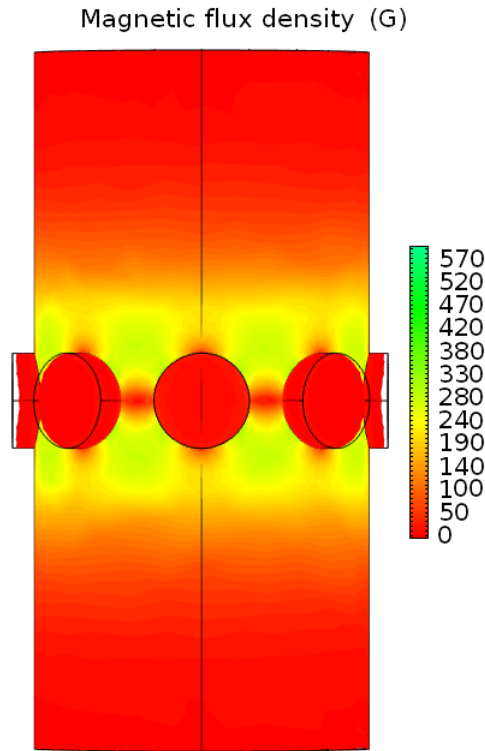
Magnetic flux density (G)

Figure 5.9: Magnetic flux density intensity B inside the inner shield in the presence of magnetic gradient of 50 G/cm produced by means of electromagnets located inside the shield. The skeleton of the cylindrical shield corresponds to the black solid lines.

ing the length of the system has a double benefit. On the one hand it increases the shielding efficiency, on the other, it helps having a more homogeneous residual magnetic field inside the region of interest (see Fig.5.11). The absolute values of $\vec{B}$ at the center of the shield for three different configurations are reported in Table(5.1).

$L_{in} [mm]$	84.1	104.1	124.1
$B_{res} [\mu G]$	416	197	154

Table 5.1: Residual magnetic field intensity B_{res} measured at the center of the four-layer magnetic shield as a function of the initial height of the shield L_{in} with an external magnetic field of 1 G along $\hat{x}$. Here the total inter-layer axial distance is 20 mm (10 mm each side).

A similar analysis was done keeping the height of the innermost layer fixed at 84 mm and varying the total inter-layer distance d_{inter} from 20 to 60[3] mm as sketched in Fig.5.10. The values of B at the center of the shield are reported in Table(5.2).

---

3 Note that these simulations were performed before defining the actual geometry of the experimental setup, hence not considering real space constraints.
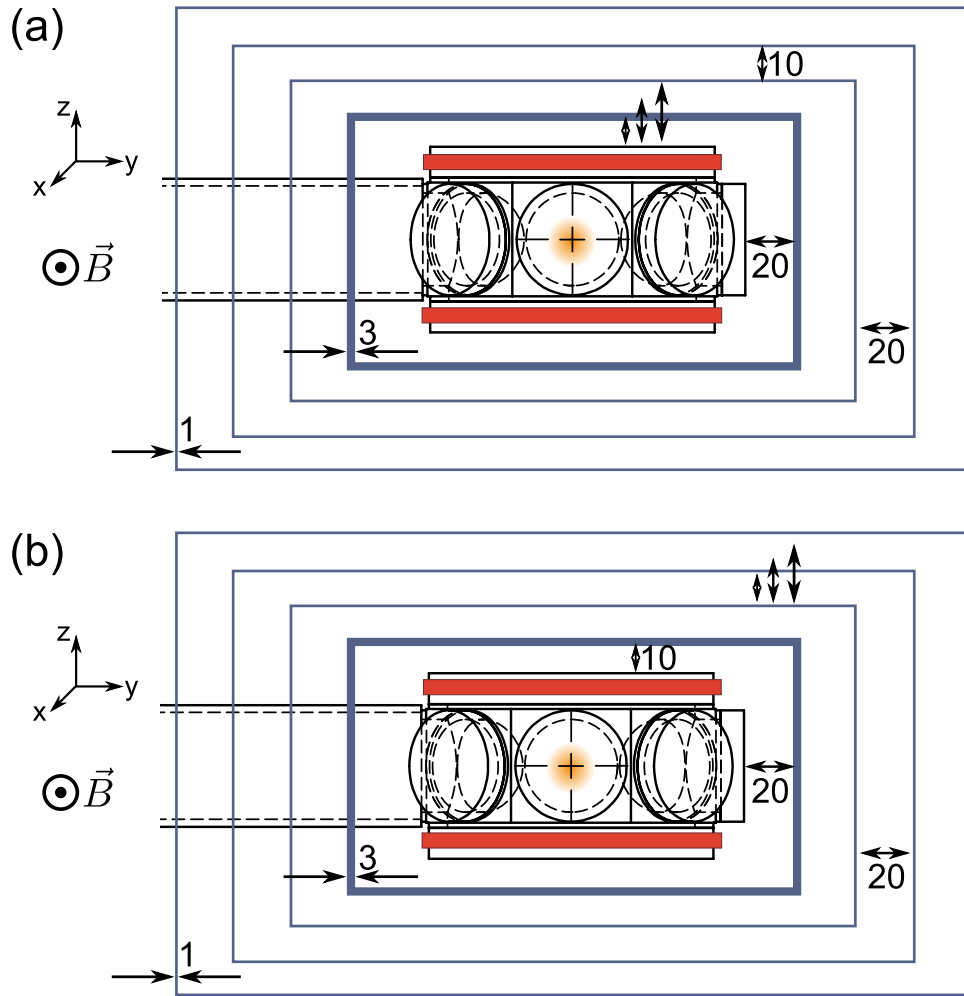
Figure 5.10: Sketch of the shield geometry used to simulate the role of the height of the innermost layer L_{in} (a) and the role of inter-layer distance d_{inter} (b). In the figure the octagonal cell and the internal electromagnets (red) are drawn at the center of the shield, as well as the thickness of each layer. All measurements are in mm. The three adjacent arrows reported in both figures, represent the quantity which was varied during the simulation.

d_{inter} [mm]	20	40	60
B_{res} [μG]	416	69	43

Table 5.2: Residual magnetic field intensity B_{res} measured at the center of the four-layer magnetic shield as a function of the total inter-layer spacing d_{inter} with an external magnetic field of 1 G along $\hat{x}$. The height of the innermost layer is fixed at 84.1 mm.

As one could expect, by increasing the distance between adjacent layers it is possible to reduce the residual magnetic field at the center of the shield. In particular, its absolute value is smaller than the one observed when the sizes of all layers are rigidly increased. Concerning the homogeneity of the magnetic field inside the shield, increasing the inter-layer distance helps obtaining a more uniform $\vec{B}$ in the region of interest. These simulations also show that increasing the inter-layer distance from 10 to 20 mm produces a
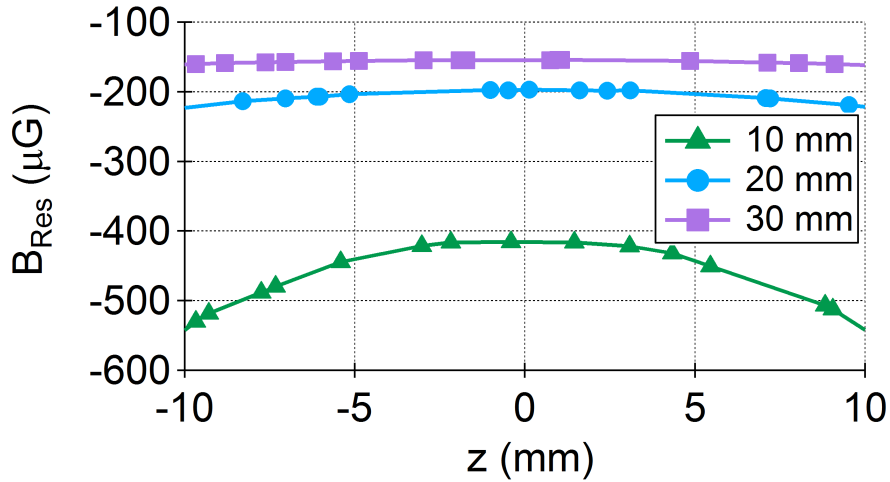
Figure 5.11: Detail of the residual magnetic field intensity B_{res} along $(0, 0, z)$ as a function of the initial height of the shield L_{in} with an external magnetic field of 1 G along $\hat{x}$. Here the total inter-layer axial distance is fixed at 20 mm (10 mm each side).

considerable improvement both in terms of homogeneity and attenuation, while increasing d_{inter} does not bring substantial benefits.

All these simulations were realized considering the geometry reported in Fig.5.10, where the innermost layer has a radius of 57 mm, it is 84 mm high and the external magnetic field is oriented along $\hat{x}$ or $\hat{z}$. The different orientations of the external magnetic field produce similar results, thus we decided to fix the inter-layer distance close to 20 mm and to largely increase the length of the innermost layer. This elongated design permits to obtain a good shielding performance (see Sec.5.4.6) also in the axial direction which, generally, is the less efficient when dealing with cylindrical geometries.

5.4.5 Collar

Another possibility to consider is the employ of collars around the holes of the shield. In fact, as already explained in Subs.5.2.1, in presence of openings the external magnetic field can penetrate in the shielded region and one way to prevent it is to add collars around each hole.

In our case, since we have no possibility to put collars around the inner cylinders due to geometry constraints, we only simulate the presence of collars around the holes of the outermost layer.

As for the other simulations we have studied the effect of an external field $B = 1$ G pointing both along x and z directions. The results show that the presence of collars helps reducing the magnetic field close to the shield walls, while at the center of the shield their contribution is not appreciable. In addition, even if the absolute value of $\vec{B}$ is slightly smaller, its spatial stability is essentially unchanged in agreement with what observed in [140]. For these reasons, we excluded the employment collars around the holes of the outermost layer.

5.4.6 Final design

The final magnetic shield design is composed of four-cylindrical layers, whose dimension in mm are reported in Fig.5.12. This design was chosen considering all results of performed simulations and including manufacturing issues.

Definitive design

The shield is composed of four layers of different material and sizes. The innermost layer is composed of Supra-50 and it is 2.5 mm thick, while the outer layer are composed of Mu-Metal and are 2 mm thick. Each layer is composed of two halves (top-layer and bottom-layer) having an opened end each. The internal radius of the bottom-layer is equal to the external radius of the top-layer (see Fig.5.13). Each top and bottom-layer is intended to be arranged one inside the other, in order to provide contact continuity. This design permits to assemble and disassemble the overall structure with relative ease. To facilitate the correct assembly of the shield, two sets of nylon supports (see Fig.5.14) were manufactured in order to fix the spacing between next layers (both top and bottom) along the axial and radial direction. The shield presents a set of ten 30 mm diameter holes and a pair of 10 mm diameter holes, which will be used for optical and cables access, respectively. In addition, in order to screw all support and layers in the correct position, a set of three holes of 4 mm diameter are present at the top and at the bottom of the six outer layers.

Theoretically, this geometry would guarantee a stability of B at the level of $10\,\mu$G (or less) and an overall attenuation of the magnetic field of more than four orders of magnitude, depending on the direction of the external magnetic field. It is worth noticing that, given the internal quantization direction i, any fluctuations of the external magnetic field will mainly affect the direction along i, since in the orthogonal direction the two field components sum in quadrature.

Expected performance

The values just introduced were obtained performing two final simulations with the real shield dimensions, holes (except for the screw ones) and a purely cylindrical geometry. The simulations were performed imposing an external magnetic field of 1 G along $\hat{x}$ and $\hat{z}$, respectively[4]. The results of these simulations are reported in Fig.5.15, where the residual magnetic field modulus B_{res} along $(x,0,0)$ and $(0,0,z)$ is shown for both orientations of the external magnetic field.

---

4 The behavior along the y direction is expected to be symmetric with respect to x.
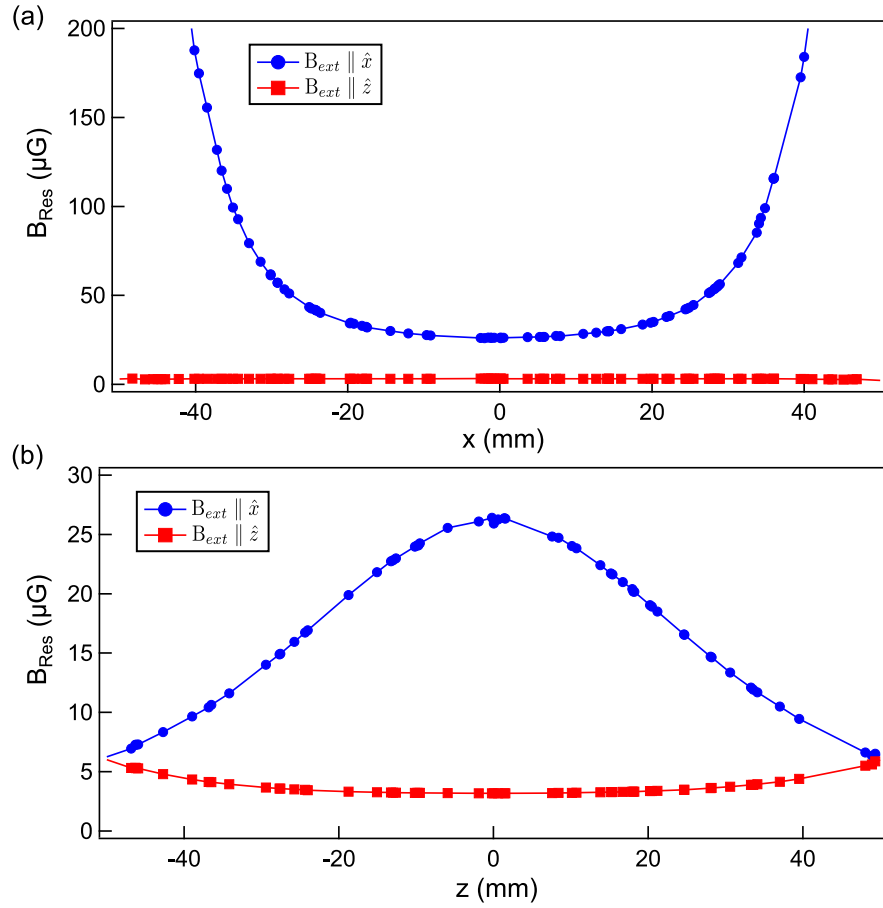
Figure 5.15: Value of the residual magnetic field intensity B_{res} along $(x, 0, 0)$ (a) and $(0, 0, z)$ (b) for two different direction of the external magnetic field $\vec{B} = 1\,\text{G}$ ($\vec{x}$ and $\vec{z}$).

In both configurations, it is visible that B_{res} is smaller and more uniform when an external magnetic field is applied along the z direction. A quantitative summary of the results obtained from the final simulations is reported in Tab.5.3.

B_{ext} direction	$B_{res}\,[\mu G]$	$\Delta B_{res_x}\,[\mu G/\text{cm}]$	$\Delta B_{res_z}\,[\mu G/\text{cm}]$
x	30	5	< 1
z	3	3	< 1

Table 5.3: Table reporting the value of the residual magnetic field intensity B_{res} at the center of the magnetic shield and its stability ΔB_{res} along $(x, 0, 0)$ and $(0, 0, z)$ for two different direction of the external magnetic field ($\vec{x}$ and $\vec{z}$).

These results show that, in principle, the shield is able to guarantee a homogeneity of the magnetic field at the level required for the experiment, being at the level of a few μG (or less). However, it is important to underline that the real shielding efficiency of the magnetic shield could be worse. In fact, in these simulations, the role of screw holes, contact between upper and lower part of the shield and welded junctions were not included. In first approximation, these factors should provide just a correction to the final attenuation, since the contact between layers is good, the welded junctions

were limited and the screw holes are small.

An additional issue that is important to mention, regards the role of the internal magnetic field applied with the electromagnets placed inside the shield. In fact, in order to have an effective stable coupling between the two hyperfine states, the internal magnetic field should be stable as well. The stability of the internal field is provided by the use of highly controlled power supplies, which will provide current to the internal electromagnets. For example, commercial laser diode drivers can ensure a current stability at the level of $1\,\mu$A and a maximum current of $100\,$mA ($SRS - LD500$), hence $\delta I/I \sim 10^{-5}$. Thus, using this kind of devices, it is possible to obtain highly stable magnetic field. This can be used to apply to the atom a $|\vec{B}| \simeq 0.1G$ or lower, which results in a Zeeman splitting of the order of a few tens of kHz. This energetic separation is large enough to permit an efficient control of the coherent coupling.

In the next future we will characterize the final shielding efficiency of the magnetic shield directly on the atoms. To do this, it is possible, for example, to compare the stability of Rabi oscillations between two hyperfine states with and without the magnetic shield, since the coherence time of these oscillations provides a direct estimate of the magnetic field stability.
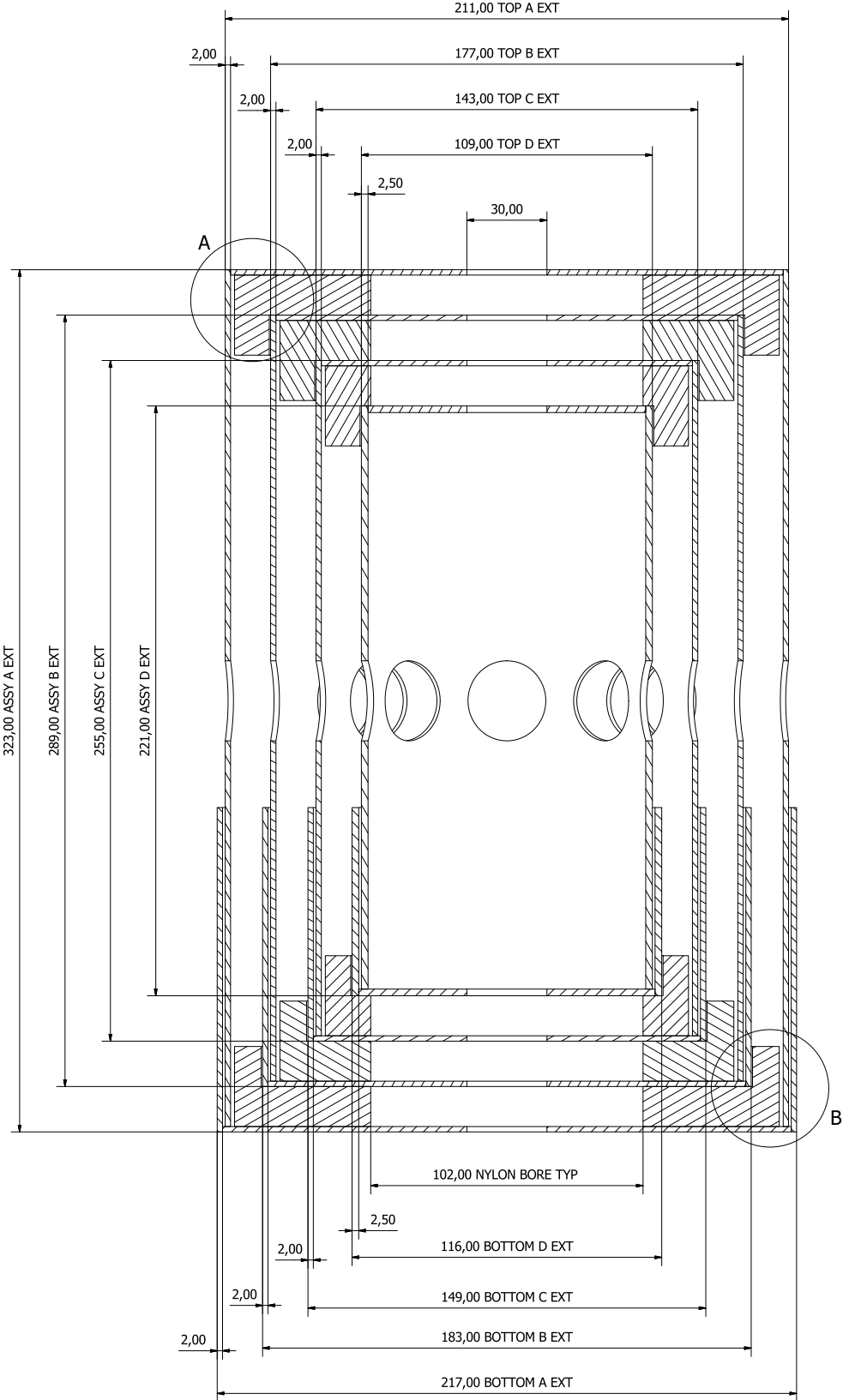
Figure 5.12: Mechanical design of the frontal section of the magnetic shield actually realized. All measures are in mm.
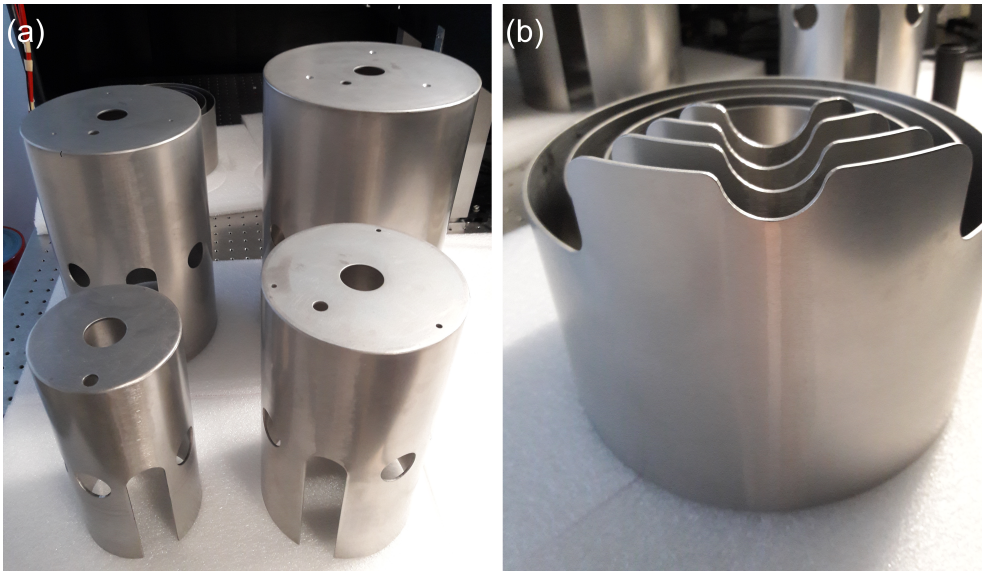
Figure 5.13: Picture of the four top-layers composing the magnetic shield (a) and picture of the four bottom-layers in the final arrangement configuration (b).

Figure 5.14: Set of nylon supports used to correctly arrange the magnetic shield, since they provide the right axial and radial spacing between each next layer.

6 | CONCLUSION

In this thesis I report on the most relevant results obtained during my doctoral studies, which mainly concern the study of spin properties of a BECs binary mixture of sodium atoms occupying $|F = 1, m_F = \pm 1\rangle$ states. The main advantage of this mixture is related to its miscibility properties, which permit to create a completely miscible mixture, not subject to buoyancy. The absence of buoyancy plays a crucial role since, for the first time, it opens to investigation of spin properties in the linear regime.

In our system, thanks to the vicinity to the miscible-immiscible phase transition, the role of interactions is magnified leading to the peculiar spin properties observed. In fact at $T = 0$ the spin-dipole oscillation frequency ω_{SD}, which characterizes the spin dynamics, was found to be about five times smaller than the harmonic oscillator ω_{ho}. In the same way, the measurement of the static spin-dipole polarizability $\mathcal{P}$ was more than twenty times larger than in the non-interacting system. From a theoretical point of view, both these quantities are expected to be influenced by interactions among particles and are expected to diverge when approaching the condition of phase separation. From the knowledge of the value of the scattering lengths, we can estimate the value of ω_{SD} and $\mathcal{P}$ as a function of the trapping condition and we find a good agreement between experimental observation and numerical simulations.

We studied the spin properties of our sodium mixture also in the regime of finite temperature below T_C. In particular, two collisional regimes were studied, namely collisionless and collisional. In both cases, the measured ω_{SD} is compatible with the one measured at $T \sim 0$ and the condensed spin oscillation shows no visible damping, oppositely to the thermal clouds relative motion which is quickly suppressed in the collisional regime. This is one of the major result of my work, since it is a direct prove of the superfluid nature of spin oscillations in the collisional regime. In addition, the static spin-dipole polarizability $\mathcal{P}$ was investigated in the case of collisional regime, showing a further enhancement with respect to the $T \sim 0$ case. In fact, at finite temperature, the role of interactions among thermal and condensed particles is not negligible. These interactions turned out to affect not only the BEC part, but also the thermal atoms which occupy the same spatial region of the condensate. This mutual interaction of thermal and condensed atoms leads to an opposite response to the displacement of the trap minima, which was observed both in the static and dynamic behavior. Also in the case of finite temperature, a direct comparison between theory and experiment was done, resulting in a good agreement.

Another topic of my research was the development of a magnetic shield able to provide an optimal control on the magnetic field experienced by the atoms, at the level of a few μG. The final shield design is a four-layer cylindrical shield made of high-permeability materials, which, theoretically, is able

to attenuate the external magnetic field by more than four orders of magnitude, hence opening to measurement of resonantly-coupled spin BECs in principle on timescale of the order of one second.

My works will contribute to the implementation of new classes of experiments in the unexplored regime when the internal spin dynamics exhibits coherence on a timescale longer than the orbital many-body dynamics. In fact, while the magnetic shield is an essential tool to have long Rabi-coupling between spin states, the study of the simplest collective oscillation of our mixture paves the way for investigating more complex dynamics, especially in the presence of coherent coupling.

As future perspectives, we aim to study the binary mixture in the presence of coupling in order to explore supersolid phases exhibited by the system and to simulate quark confinement by means of vortex-bound states. An additional perspective of my research, is the realization of a magnetic soliton which corresponds to a localized spin polarization $n_1 - n_2$ (being n_1 and n_2 the densities of the two spin component).

To conclude, completely miscible binary mixtures can be a very important ingredient for the study of several phenomena related to different scientific fields. The recent developments in degenerate binary mixtures have already opened up many new opportunities for both theory and experiment, and the possibility to reach highly magnetically controlled environments will permit to address novel interesting research directions in the field of spinor superfluid systems.

A | APPENDIX A

In this appendix some useful parameters of sodium are presented. In Tab.A.1 main physical properties of ^{23}Na are reported, while Tab.A.2 concerns optical properties of the D_2 line. In Tab.A.3 some magnetic and electric field interaction parameters of sodium D lines are reported.
In addition in Fig.A.1 and Fig.A.2 the hyperfine structure of sodium D_2 and D_2 line are shown, respectively.
All the data and pictures of the appendix are taken from [91].

Quantity	Symbol	Value
Atomic number	Z	11
Total nucleons	$Z + N$	23
Atomic mass	m	$3.81754035(19)e - 24\ kg$
Density at $25°C$	ρ_m	$0.97\ g/m^3$
Melting point	T_M	$97.8\ °C$
Vapor pressure at $25\ °C$	P_v	$2.38(12)e - 11\ Torr$
Nuclear spin	I	$3/2$

Table A.1: Sodium physical properties.

Quantity	Symbol	Value
Frequency	ω_A	$2\pi \cdot 508.8487162(13)\ THz$
Energy	$\hbar\omega_A$	$2.104029011(51)\ eV$
Wavelength in vacuum	λ_A	$589.1583264(15)\ nm$
Wave number in vacuum	$k_A/2\pi$	$16973.366160(43)\ cm^{-1}$
Lifetime	τ	$16.2492(77)\ ns$
Natural line width	Γ	$2\pi \cdot 9.7946(46)\ MHz$
Recoil velocity	v_{rec}	$2.9461\ cm/s$
Recoil temperature	T_{rec}	$2.3998\ \mu K$
Doppler temperature	T_D	$235.03\ \mu K$
Dipole matrix element	$\langle J = \frac{1}{2} \| er \| J' = \frac{3}{2} \rangle$	$2.98831(100)e - 29\ C$

Table A.2: Sodium D_2 ($3^2S_{1/2} \rightarrow 3^2P_{3/2}$) transition optical properties.

Quantity	Symbol	Value
Electron spin g-factor	g_S	2.0023193043622(15)
Electron orbital g-factor	g_L	0.99997613
	$g_J(3^2S_{1/2})$	2.00229600(70)
Fine structure Landé g-factor	$g_J(3^2P_{1/2})$	0.66581(12)
	$g_J(3^2P_{3/2})$	1.33420(20)
Nuclear g-factor	g_I	$-0.00080461080(80)$

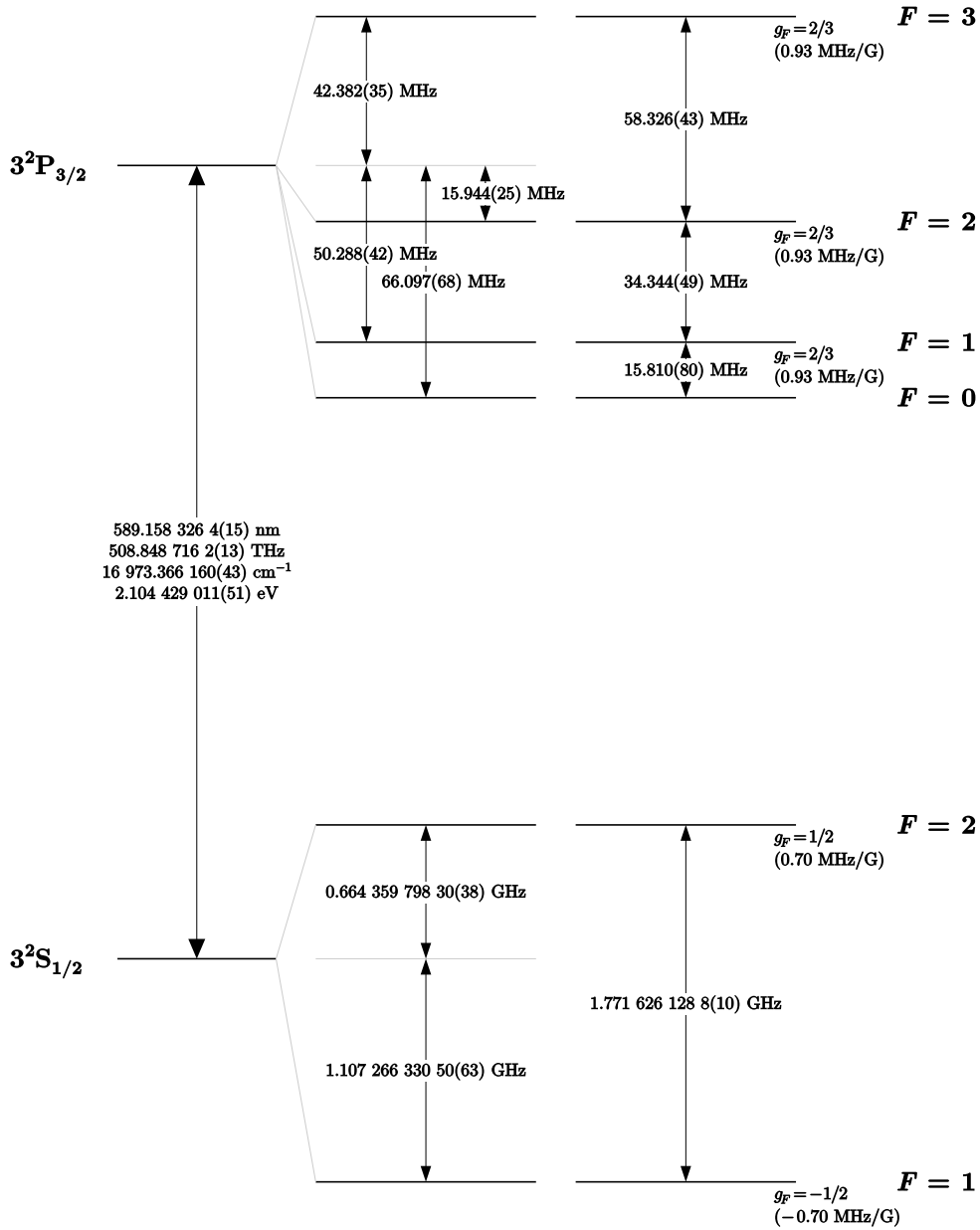**Table A.3:** Sodium D transition magnetic and electric field interaction parameters.

Figure A.1: Sodium D_2 transition hyperfine structure from [91]. In the figure the splitting between each state is reported in frequency units and the Landè g-factor is also given for each level. In parenthesis the Zeeman splitting per units of Gauss is reported for each adjacent sublevel.

$3^2\mathrm{P}_{1/2}$

70.830(98) MHz

118.05(16) MHz

$g_F = 1/6$
(0.23 MHz/G)

$F = 2$

188.88(26) MHz

$g_F = -1/6$
(-0.23 MHz/G)

$F = 1$

589.755 814 7(15) nm
508.333 195 8(13) THz
16 956.170 250(43) cm^{-1}
2.102 296 990(51) eV

$3^2\mathrm{S}_{1/2}$

0.664 359 798 30(38) GHz

1.107 266 330 50(63) GHz

$g_F = 1/2$
(0.70 MHz/G)

$F = 2$

1.771 626 128 8(10) GHz

$g_F = -1/2$
(-0.70 MHz/G)

$F = 1$
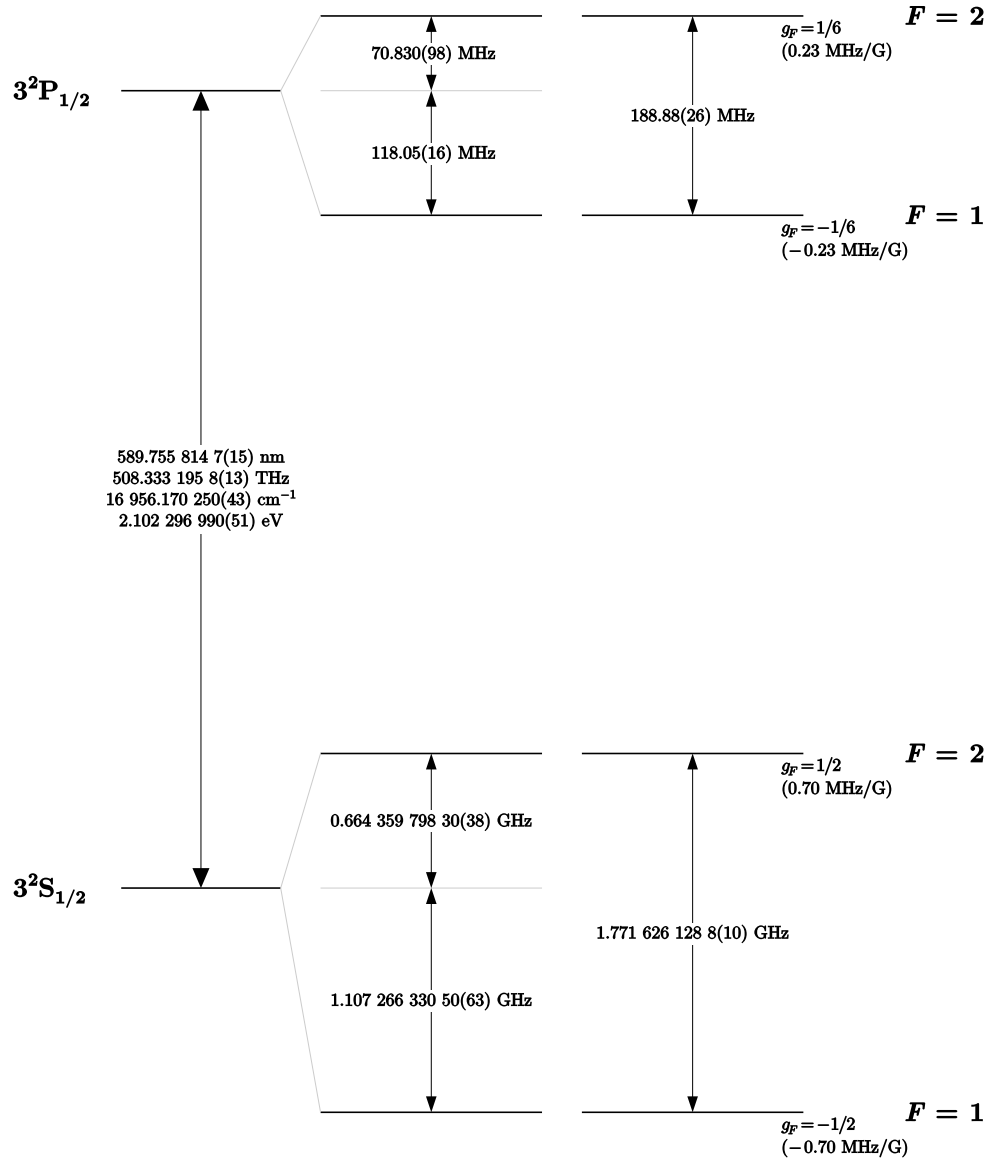
Figure A.2: Sodium D_1 transition hyperfine structure from [91]. In the figure the splitting between each state is reported in frequency units and the Landè g-factor is also given for each level. In parenthesis the Zeeman splitting per units of Gauss is reported for each adjacent sublevel.

BIBLIOGRAPHY

[1] M. H. Anderson et al. "Observation of Bose-Einstein condensation in a dilute atomic vapor". In: *Science* 269.5221 (1995), pp. 198–201 (cit. on pp. 1, 23).

[2] K. B. Davis et al. "Bose-Einstein Condensation in a Gas of Sodium Atoms". In: *Phys. Rev. Lett.* 75 (22 1995), pp. 3969–3973. DOI: `10.1103/PhysRevLett.75.3969` (cit. on pp. 1, 23).

[3] I. Bloch, J. Dalibard, and S. Nascimbène. "Quantum simulations with ultracold quantum gases". In: *Nature Physics* 8 (2012), 267–276. DOI: `10.1038/nphys2259` (cit. on p. 1).

[4] Jimenez-Garcia K. Spielman-I. B. Lin Y.-J. "Spin-orbit-coupled Bose-Einstein condensates". In: *Nature* 471 (2011), pp. 83–86. DOI: `10.1038/nature09887` (cit. on pp. 1, 48).

[5] Simone Serafini et al. "Vortex Reconnections and Rebounds in Trapped Atomic Bose-Einstein Condensates". In: *Phys. Rev. X* 7 (2 2017), p. 021031. DOI: `10.1103/PhysRevX.7.021031` (cit. on p. 1).

[6] J. Steinhauer. "Observation of quantum Hawking radiation and its entanglement in an analogue black hole". In: *Nature Physics* 12 (2016), 959–965. DOI: `10.1038/nphys3863` (cit. on p. 1).

[7] T. Jacobson I.B. Spielman G.K. Campbell S. Eckel A. Kumar. "A supersonically expanding Bose-Einstein condensate: an expanding universe in the lab". In: *ArXiv e-prints* (2017) (cit. on p. 1).

[8] Tilman Esslinger Theodor W. Hänsch Immanuel Bloch Markus Greiner Olaf Mandel. "Quantum phase transition from a superfluid to a Mott insulator in a gas of ultracold atoms". In: *Nature* 415 (2002), pp. 39–44. DOI: `10.1038/415039a` (cit. on p. 1).

[9] J.F. Annett. *Superconductivity, Superfluids and Condensates*. Oxford, 2004 (cit. on p. 1).

[10] G.A. Prinz. "Magnetoelectronics". In: *Science* 282 (5394 1998), pp. 1660–1663. DOI: `10.1126/science.282.5394.1660` (cit. on p. 1).

[11] R. A. Duine and H. T. C. Stoof. "Spin Drag in Noncondensed Bose Gases". In: *Phys. Rev. Lett.* 103 (17 2009), p. 170401. DOI: `10.1103/PhysRevLett.103.170401` (cit. on p. 1).

[12] E.B. Sonin. "Spin currents and spin superfluidity". In: *Advances in Physics* 59.3 (2010), pp. 181–255 (cit. on pp. 1, 63).

[13] D.J Thouless. "The flow of a dense superfluid". In: *Annals of Physics* 52.3 (1969), pp. 403 –427. DOI: `https://doi.org/10.1016/0003-4916(69)90286-3` (cit. on p. 1).

[14] A.F. Andreev and I.M. Lifshitz. "Quantum theory of defects in crystals". In: *Sov. Phys. JETP* 29.1107 (1969) (cit. on p. 1).

[15] Massimo Boninsegni and Nikolay V. Prokof'ev. "Colloquium". In: *Rev. Mod. Phys.* 84 (2 2012), pp. 759–776. DOI: `10.1103/RevModPhys.84.759` (cit. on p. 1).

[16] Yun Li et al. "Superstripes and the Excitation Spectrum of a Spin-Orbit-Coupled Bose-Einstein Condensate". In: *Phys. Rev. Lett.* 110 (23 2013), p. 235302. DOI: `10.1103/PhysRevLett.110.235302` (cit. on p. 2).

[17] A. Zupancic P. Esslinger T. Léonard J. Morales and T. Donner. "Supersolid formation in a quantum gas breaking a continuous translational symmetry". In: *Nature* 543 (2017), 87–90. DOI: `10.1038/nature21067` (cit. on p. 2).

[18] Wujie Huang Sean Burchesky Boris Shteynas Furkan Çağrı Top Alan O. Jamison Wolfgang Ketterle Jun-Ru Li Jeongwon Lee. "A stripe phase with supersolid properties in spin–orbit-coupled Bose–Einstein condensates". In: *Nature* 543 (2017), 91–94. DOI: `10.1038/nature21431` (cit. on p. 2).

[19] C. J. Myatt et al. "Production of Two Overlapping Bose-Einstein Condensates by Sympathetic Cooling". In: *Phys. Rev. Lett.* 78 (4 1997), pp. 586–589. DOI: `10.1103/PhysRevLett.78.586` (cit. on pp. 2, 7, 16).

[20] D. S. Hall et al. "Dynamics of Component Separation in a Binary Mixture of Bose-Einstein Condensates". In: *Phys. Rev. Lett.* 81 (8 1998), pp. 1539–1542. DOI: `10.1103/PhysRevLett.81.1539` (cit. on pp. 2, 7, 8, 16, 17, 48).

[21] P. Maddaloni et al. "Collective Oscillations of Two Colliding Bose-Einstein Condensates". In: *Phys. Rev. Lett.* 85 (12 2000), pp. 2413–2417. DOI: `10.1103/PhysRevLett.85.2413` (cit. on pp. 2, 7).

[22] M. Modugno et al. "Damping and frequency shift in the oscillations of two colliding Bose-Einstein condensates". In: *The European Physical Journal D - Atomic, Molecular, Optical and Plasma Physics* 17.3 (2001), pp. 345–349. DOI: `10.1007/s100530170009` (cit. on pp. 2, 7).

[23] G. Modugno et al. "Two Atomic Species Superfluid". In: *Phys. Rev. Lett.* 89 (19 2002), p. 190404. DOI: `10.1103/PhysRevLett.89.190404` (cit. on pp. 2, 7).

[24] F. Ferlaino et al. "Dipolar oscillations in a quantum degenerate Fermi–Bose atomic mixture". In: *Journal of Optics B: Quantum and Semiclassical Optics* 5.2 (2003), S3 (cit. on pp. 2, 7).

[25] K. M. Mertes et al. "Nonequilibrium Dynamics and Superfluid Ring Excitations in Binary Bose-Einstein Condensates". In: *Phys. Rev. Lett.* 99 (19 2007), p. 190402. DOI: `10.1103/PhysRevLett.99.190402` (cit. on pp. 2, 7, 8, 63).

[26] C. Hamner et al. "Generation of Dark-Bright Soliton Trains in Superfluid-Superfluid Counterflow". In: *Phys. Rev. Lett.* 106 (6 2011), p. 065302 (cit. on pp. 2, 7, 16, 63).

[27] E. Nicklas et al. "Rabi Flopping Induces Spatial Demixing Dynamics". In: *Phys. Rev. Lett.* 107 (19 2011), p. 193001. DOI: `10.1103/PhysRevLett.107.193001` (cit. on pp. 2, 7, 16).

[28] Cheng-Hsun Wu et al. "Ultracold Fermionic Feshbach Molecules of ^{23}Na^{40}K". In: *Phys. Rev. Lett.* 109 (8 2012), p. 085301. DOI: 10.1103/PhysRevLett.109.085301 (cit. on pp. 2, 7).

[29] I. Ferrier-Barbut et al. "A mixture of Bose and Fermi superfluids". In: *Science* 345.6200 (2014), pp. 1035–1038. DOI: 10.1126/science.1255380 (cit. on pp. 2, 7).

[30] Tetsu Takekoshi et al. "Ultracold Dense Samples of Dipolar RbCs Molecules in the Rovibrational and Hyperfine Ground State". In: *Phys. Rev. Lett.* 113 (20 2014), p. 205301. DOI: 10.1103/PhysRevLett.113.205301 (cit. on pp. 2, 7).

[31] Marion Delehaye et al. "Critical Velocity and Dissipation of an Ultracold Bose-Fermi Counterflow". In: *Phys. Rev. Lett.* 115 (26 2015), p. 265303. DOI: 10.1103/PhysRevLett.115.265303 (cit. on pp. 2, 7).

[32] K. Jiménez-García et al. "Tunable Spin-Orbit Coupling via Strong Driving in Ultracold-Atom Systems". In: *Phys. Rev. Lett.* 114 (12 2015), p. 125301. DOI: 10.1103/PhysRevLett.114.125301 (cit. on pp. 2, 7, 16).

[33] S. B. Koller et al. "Quantum enhancement of spin drag in a Bose gas". In: *New Journal of Physics* 17.11 (2015), p. 113026 (cit. on pp. 2, 7, 77).

[34] E. Nicklas et al. "Nonlinear dressed states at the miscibility-immiscibility threshold". In: *Phys. Rev. A* 92 (5 2015), p. 053614. DOI: 10.1103/PhysRevA.92.053614 (cit. on pp. 2, 7, 8).

[35] A. Guttridge et al. "Interspecies thermalization in an ultracold mixture of Cs and Yb in an optical trap". In: *Phys. Rev. A* 96 (1 2017), p. 012704. DOI: 10.1103/PhysRevA.96.012704 (cit. on pp. 2, 7).

[36] Richard Roy et al. "Two-Element Mixture of Bose and Fermi Superfluids". In: *Phys. Rev. Lett.* 118 (5 2017), p. 055301. DOI: 10.1103/PhysRevLett.118.055301 (cit. on pp. 2, 7).

[37] L.Masi C.Mazzinghi L.Wolswijk F.Minardi M.Modugno G.Modugno M.Inguscio M.Fattori G.Semeghini G.Ferioli. "Self-bound quantum droplets in atomic mixtures". In: *ArXiv e-prints* (2017) (cit. on pp. 2, 7, 9).

[38] A. Bohr and B.R. Mottelson. *Nuclear Structure*. v. 2. W.A. Benjamin (New York), 1975 (cit. on p. 2).

[39] D. Pines and P. Nozières. *The Theory of Quantum Liquids*. v. 1. W.A. Benjamin (New York), 1966 (cit. on p. 2).

[40] D. T. Son and M. A. Stephanov. "Domain walls of relative phase in two-component Bose-Einstein condensates". In: *Phys. Rev. A* 65 (6 2002), p. 063621. DOI: 10.1103/PhysRevA.65.063621 (cit. on p. 3).

[41] N. Bogoliubov. "On the theory of superfluidity". In: *J.Phys.(Mosocw)* 11.23 (1947) (cit. on p. 5).

[42] Lev Pitaevskii and Sandro Stringari. *Bose-Einstein Condensation and Superfluidity*. Oxford University Press (OUP), January 2016 (cit. on pp. 5, 6, 8, 12–14, 57, 76).

[43] D. M. Stamper-Kurn et al. "Optical Confinement of a Bose-Einstein Condensate". In: *Phys. Rev. Lett.* 80 (10 1998), pp. 2027–2030. DOI: 10.1103/PhysRevLett.80.2027 (cit. on pp. 7, 80).

[44] D. M. Stamper-Kurn H.-J. Miesner A. P. Chikkatur W. Ketterle J. Stenger S. Inouye. "Spin domains in ground-state Bose—Einstein condensates". In: *Nature* 396 (1998), pp. 345–348. DOI: 10.1038/24567 (cit. on p. 7).

[45] H. Schmaljohann et al. "Dynamics and thermodynamics in spinor quantum gases". In: *Applied Physics B* 79.8 (2004), pp. 1001–1007. DOI: 10.1007/s00340-004-1664-6 (cit. on p. 7).

[46] J. M. Higbie et al. "Direct Nondestructive Imaging of Magnetization in a Spin-1 Bose-Einstein Gas". In: *Phys. Rev. Lett.* 95 (5 2005), p. 050401. DOI: 10.1103/PhysRevLett.95.050401 (cit. on pp. 7, 59).

[47] Adilet Imambekov, Mikhail Lukin, and Eugene Demler. "Spin-exchange interactions of spin-one bosons in optical lattices: Singlet, nematic, and dimerized phases". In: *Phys. Rev. A* 68 (6 2003), p. 063602. DOI: 10.1103/PhysRevA.68.063602 (cit. on p. 7).

[48] E. M. Bookjans, A. Vinit, and C. Raman. "Quantum Phase Transition in an Antiferromagnetic Spinor Bose-Einstein Condensate". In: *Phys. Rev. Lett.* 107 (19 2011), p. 195306. DOI: 10.1103/PhysRevLett.107.195306 (cit. on p. 7).

[49] T. Zibold et al. "Spin-nematic order in antiferromagnetic spinor condensates". In: *Phys. Rev. A* 93 (2 2016), p. 023614 (cit. on p. 7).

[50] J. H. Kim, S. W. Seo, and Y.-i. Shin. "Critical spin superflow in a spinor Bose-Einstein condensate". In: *ArXiv e-prints* (July 2017) (cit. on pp. 7, 63).

[51] Tetsuo Ohmi and Kazushige Machida. "Bose-Einstein Condensation with Internal Degrees of Freedom in Alkali Atom Gases". In: *Journal of the Physical Society of Japan* 67.6 (1998), pp. 1822–1825. DOI: 10.1143/JPSJ.67.1822 (cit. on p. 7).

[52] Tin-Lun Ho. "Spinor Bose Condensates in Optical Traps". In: *Phys. Rev. Lett.* 81 (4 1998), pp. 742–745. DOI: 10.1103/PhysRevLett.81.742 (cit. on p. 7).

[53] Yong-Qing Liu. "Magnons interaction of spinor Bose-Einstein condensates in an optical lattice". In: *Pramana* 73.6 (2009), p. 1105. DOI: 10.1007/s12043-009-0170-0 (cit. on p. 7).

[54] Yuki Kawaguchi and Masahito Ueda. "Spinor Bose–Einstein condensates". In: *Physics Reports* 520.5 (2012), pp. 253 –381. DOI: https://doi.org/10.1016/j.physrep.2012.07.005 (cit. on p. 7).

[55] Dan M. Stamper-Kurn and Masahito Ueda. "Spinor Bose gases: Symmetries, magnetism, and quantum dynamics". In: *Rev. Mod. Phys.* 85 (3 2013), pp. 1191–1244. DOI: 10.1103/RevModPhys.85.1191 (cit. on p. 7).

[56] T. Kawakami, T. Mizushima, and K. Machida. "Textures of Spin-Orbit Coupled F = 2 Spinor Bose Einstein Condensates". In: *Journal of Physics: Conference Series* 400.1 (2012), p. 012028 (cit. on p. 7).

[57] Jeffrey Yepez. "Quantum lattice gas model of spin-2 Bose-Einstein condensates and closed-form analytical continuation of nonlinear interactions in spin-2 superfluids". In: *ArXiv e-prints* (2017) (cit. on p. 7).

[58] E. Timmermans. "Phase Separation of Bose-Einstein Condensates". In: *Phys. Rev. Lett.* 81 (26 1998), pp. 5718–5721. DOI: 10.1103/PhysRevLett.81.5718 (cit. on p. 7).

[59] A. Sinatra et al. "Dynamics of Two Interacting Bose-Einstein Condensates". In: *Phys. Rev. Lett.* 82 (2 1999), pp. 251–254. DOI: 10.1103/PhysRevLett.82.251 (cit. on p. 7).

[60] D. M. Jezek and P. Capuzzi. "Interaction-driven effects on two-component Bose-Einstein condensates". In: *Phys. Rev. A* 66 (1 2002), p. 015602. DOI: 10.1103/PhysRevA.66.015602 (cit. on pp. 7, 13).

[61] Marta Abad and Alessio Recati. "A study of coherently coupled two-component Bose-Einstein condensates". In: *The European Physical Journal D* 67.7 (2013), p. 148. DOI: 10.1140/epjd/e2013-40053-2 (cit. on pp. 7, 14).

[62] Alberto Sartori and Alessio Recati. "Dynamics of highly unbalanced Bose-Bose mixtures: miscible vs. immiscible gases". In: *The European Physical Journal D* 67.12 (2013), p. 260. DOI: 10.1140/epjd/e2013-40635-x (cit. on p. 7).

[63] Marta Abad et al. "Counter-flow instability of a quantum mixture of two superfluids". In: *The European Physical Journal D* 69.5 (2015), p. 126. DOI: 10.1140/epjd/e2015-50851-y (cit. on p. 7).

[64] R. N. Bisset, R. M. Wilson, and C. Ticknor. "Scaling of fluctuations in a trapped binary condensate". In: *Phys. Rev. A* 91 (5 2015), p. 053613. DOI: 10.1103/PhysRevA.91.053613 (cit. on pp. 7, 14).

[65] Kean Loon Lee et al. "Phase separation and dynamics of two-component Bose-Einstein condensates". In: *Phys. Rev. A* 94 (1 2016), p. 013602. DOI: 10.1103/PhysRevA.94.013602 (cit. on p. 7).

[66] Yujiro Eto et al. "Nonequilibrium dynamics induced by miscible–immiscible transition in binary Bose–Einstein condensates". In: *New Journal of Physics* 18.7 (2016), p. 073029 (cit. on p. 7).

[67] F. Schreck et al. "Quasipure Bose-Einstein Condensate Immersed in a Fermi Sea". In: *Phys. Rev. Lett.* 87 (8 2001), p. 080403. DOI: 10.1103/PhysRevLett.87.080403 (cit. on p. 7).

[68] W. B. Colson and Alexander L. Fetter. "Mixtures of Bose liquids at finite temperature". In: *Journal of Low Temperature Physics* 33.3 (1978), pp. 231–242. DOI: 10.1007/BF00114996 (cit. on p. 7).

[69] Tom Bienaimé et al. "Spin-dipole oscillation and polarizability of a binary Bose-Einstein condensate near the miscible-immiscible phase transition". In: *Phys. Rev. A* 94 (6 2016), p. 063652. DOI: 10.1103/PhysRevA.94.063652 (cit. on pp. 7, 73).

[70] A Sartori et al. "Spin-dipole oscillation and relaxation of coherently coupled Bose–Einstein condensates". In: *New Journal of Physics* 17.9 (2015), p. 093036 (cit. on pp. 8, 13, 14, 68).

[71]   Tin-Lun Ho and V. B. Shenoy. "Binary Mixtures of Bose Condensates of Alkali Atoms". In: *Phys. Rev. Lett.* 77 (16 1996), pp. 3276–3279. DOI: 10.1103/PhysRevLett.77.3276 (cit. on p. 8).

[72]   D. S. Petrov. "Quantum Mechanical Stabilization of a Collapsing Bose-Bose Mixture". In: *Phys. Rev. Lett.* 115 (15 2015), p. 155302. DOI: 10.1103/PhysRevLett.115.155302 (cit. on p. 9).

[73]   J. Sanz-B. Naylor-P. Thomas P. Cheiney L. Tarruell C. R. Cabrera L. Tanzi. "Quantum liquid droplets in a mixture of Bose-Einstein condensates". In: *ArXiv e-prints* (2017) (cit. on p. 9).

[74]   S. Stringari. "Collective Excitations of a Trapped Bose-Condensed Gas". In: *Phys. Rev. Lett.* 77 (12 1996), pp. 2360–2363. DOI: 10.1103/PhysRevLett.77.2360 (cit. on pp. 13, 57).

[75]   David M. Weld et al. "Thermometry and refrigeration in a two-component Mott insulator of ultracold atoms". In: *Phys. Rev. A* 82 (5 2010), p. 051603 (cit. on p. 16).

[76]   A. Marte et al. "Feshbach Resonances in Rubidium 87: Precision Measurement and Analysis". In: *Phys. Rev. Lett.* 89 (28 2002), p. 283202. DOI: 10.1103/PhysRevLett.89.283202 (cit. on p. 16).

[77]   E. Fava et.al. "Spin Superfluidity of a Bose Gas Mixture at Finite Temperature". In: *ArXiv e-prints* (2017) (cit. on pp. 16, 84).

[78]   S. Knoop et al. "Feshbach spectroscopy and analysis of the interaction potentials of ultracold sodium". In: *Phys. Rev. A* 83 (4 2011), p. 042704. DOI: 10.1103/PhysRevA.83.042704 (cit. on pp. 16, 68, 72).

[79]   P.G. Kevrekidis, D.J. Frantzeskakis, and R. Carretero-González. *Emergent Nonlinear Phenomena in Bose-Einstein Condensates: Theory and Experiment*. Springer Series on Atomic, Optical, and Plasma Physics. Springer Berlin Heidelberg, 2007 (cit. on p. 17).

[80]   Victor V. Goldman, Isaac F. Silvera, and Anthony J. Leggett. "Atomic hydrogen in an inhomogeneous magnetic field: Density profile and Bose-Einstein condensation". In: *Phys. Rev. B* 24 (5 1981), pp. 2870–2873. DOI: 10.1103/PhysRevB.24.2870 (cit. on p. 17).

[81]   David A. Huse and Eric D. Siggia. "The density distribution of a weakly interacting bose gas in an external potential". In: *Journal of Low Temperature Physics* 46.1 (1982), pp. 137–149. DOI: 10.1007/BF00655448 (cit. on p. 17).

[82]   L. P.and Stringari S. Giorgini S.and Pitaevskii. "Thermodynamics of a trapped Bose-condensed gas". In: *Journal of Low Temperature Physics* 109.1 (1997), pp. 309–355. DOI: 10.1007/BF02396737 (cit. on p. 18).

[83]   William D. Phillips and Harold Metcalf. "Laser Deceleration of an Atomic Beam". In: *Phys. Rev. Lett.* 48 (9 1982), pp. 596–599. DOI: 10.1103/PhysRevLett.48.596 (cit. on p. 23).

[84]   E. L. Raab et al. "Trapping of Neutral Sodium Atoms with Radiation Pressure". In: *Phys. Rev. Lett.* 59 (1987), p. 2631 (cit. on pp. 23, 44).

[85]   J. Catani et al. "Intense slow beams of bosonic potassium isotopes". In: *Phys. Rev. A* 73 (3 2006), p. 033415. DOI: 10.1103/PhysRevA.73. 033415 (cit. on p. 23).

[86]   K. Dieckmann et al. "Two-dimensional magneto-optical trap as a source of slow atoms". In: *Phys. Rev. A* 58 (5 1998), pp. 3891–3895. DOI: 10.1103/PhysRevA.58.3891 (cit. on p. 23).

[87]   J. Yu et al. "Funnel with orientated Cs atoms". In: *Optics Communications* 112.3ï¿œ4 (1994), pp. 136 –140. DOI: 10.1016/0030-4018(94) 00439-0 (cit. on p. 23).

[88]   K. M. R. van der Stam et al. "Large atom number Bose-Einstein condensate of sodium". In: *Review of Scientific Instruments* 78.1, 013102 (2007), p. 013102. DOI: 10.1063/1.2424439 (cit. on p. 24).

[89]   T. G. Tiecke et al. "High-flux two-dimensional magneto-optical-trap source for cold lithium atoms". In: *Physical Review A* 80.1 (2009), p. 013409 (cit. on p. 24).

[90]   G. Lamporesi et al. "Compact high-flux source of cold sodium atoms". In: *Rev. Sci. Instrum.* 84.6 (2013), p. 063102 (cit. on pp. 24, 29, 43).

[91]   D. A. Steck. "Sodium D Line Data". In: (2010). revision 2.1.4, 23 December 2010 (cit. on pp. 27, 49, 119, 121, 122).

[92]   L. Ricci et al. "A compact grating-stabilized diode laser system for atomic phisics". In: *Optics Communications* 117.541-549 (1995) (cit. on p. 27).

[93]   G. P. Agrawal. *Fiber Optic Communication Systems*. Wiley, 2002 (cit. on p. 27).

[94]   T. W. Hansch and B. Couillaud. "Laser frequency stabilization by polarization spectroscopy of a reflecting reference cavity". In: *Optics Communications* 35 (1980), pp. 441–444. DOI: 10.1016/0030-4018(80) 90069-3 (cit. on p. 27).

[95]   C. J. Foot. *Atomic Physics*. Oxford University Press, 2005 (cit. on pp. 27, 48, 53).

[96]   Daniel Adam Steck. "Classical and Moder Optics". In: (2011). revision 1.4.22, 17 April 2012 (cit. on p. 27).

[97]   B. E. A. Saleh and M. C. Teich. *Fundamentals of Photonics*. Wiley, 2007 (cit. on p. 27).

[98]   Y. B. Ovchinnikov Grimm R. M. Weidemüller. "Optical dipole traps for neutral atoms". In: *Adv.At.,Mol.Opt.Phys.* 42.95-170 (2000) (cit. on p. 28).

[99]   W. Ketterle, D. S. Durfee, and D. M. Stamper-Kurn. "Making, probing and understanding Bose-Einstein condensates". In: *Bose-Einstein Condensation in Atomic Gases*. Ed. by M. Inguscio, Stringari S., and C. E. Wieman. Proceedings of the International School of Physics "Enrico Fermi", Course CXL. 1999 (cit. on pp. 29, 38, 46, 81).

[100] W. Ketterle et al. "High densities of cold atoms in a dark spontaneous-force optical trap". In: *Physical review letters* 70.15 (1993), pp. 2253–2256 (cit. on pp. 29, 44).

[101] Paul D. Lett et al. "Observation of Atoms Laser Cooled below the Doppler Limit". In: *Phys. Rev. Lett.* 61 (2 1988), pp. 169–172. DOI: `10.1103/PhysRevLett.61.169` (cit. on p. 29).

[102] D. E. Pritchard. "Cooling Neutral Atoms in a Magnetic Trap for Precision Spectroscopy". In: *Phys. Rev. Lett.* 51 (15 1983), pp. 1336–1339. DOI: `10.1103/PhysRevLett.51.1336` (cit. on p. 29).

[103] E. Majorana. "Atomi orientati in campo magnetico variabile". In: *Nuovo Cimento* 9.43 (1932) (cit. on p. 30).

[104] S. Serafini. "Realization of a magnetic trap for sodium Bose–Einstein condensates". MA thesis. University of Trento, 2012 (cit. on p. 33).

[105] O. Svelto. *Principles of lasers*. Fifth edition. Springer, 2010 (cit. on p. 34).

[106] J. G. Ziegler and N. B. Nichols. "Optimum Settings for Automatic Controllers". In: *Transactions on ASME* 64 (1942), pp. 759–768 (cit. on p. 37).

[107] S. Donadello. "Observation of the Kibble–Zurek mechanism in a bosonic gas". PhD thesis. University of Trento, 2016 (cit. on p. 38).

[108] Daniel Adam Steck. "Quantum and Atom Optics". In: (2011). revision 0.8.2, 6 December 2011 (cit. on p. 38).

[109] J. Dalibard and C. Cohen-Tannoudji. "Laser cooling below the Doppler limit by polarization gradients: simple theoretical models". In: *J. Opt. Soc. Am. B* 6.11 (1989), pp. 2023–2045. DOI: `10.1364/JOSAB.6.002023` (cit. on p. 44).

[110] Giacomo Colzi et al. "Sub-Doppler cooling of sodium atoms in gray molasses". In: *Phys. Rev. A* 93 (2 2016), p. 023421. DOI: `10.1103/PhysRevA.93.023421` (cit. on p. 44).

[111] Wolfgang Ketterle and N.J. Van Druten. "Evaporative Cooling of Trapped Atoms". In: *Advances In Atomic, Molecular, and Optical Physics* 37 (1996), pp. 181 –236. DOI: `http://dx.doi.org/10.1016/S1049-250X(08)60101-9` (cit. on p. 45).

[112] C. Cohen-Tannoudji and D. Guéry-Odelin. *Advances in Atomic Physics, An Overview*. Singapore: World Scientific, 2011 (cit. on p. 45).

[113] P. Pillet et al. "Adiabatic population transfer in a multilevel system". In: *Phys. Rev. A* 48 (1 1993), pp. 845–848. DOI: `10.1103/PhysRevA.48.845` (cit. on p. 47).

[114] Jan R. Rubbmark et al. "Dynamical effects at avoided level crossings: A study of the Landau-Zener effect using Rydberg atoms". In: *Phys. Rev. A* 23 (6 1981), pp. 3107–3117. DOI: `10.1103/PhysRevA.23.3107` (cit. on pp. 48, 49).

[115] G. Breit and I. I. Rabi. "Measurement of Nuclear Spin". In: *Phys. Rev.* 38 (11 1931), pp. 2082–2083. DOI: `10.1103/PhysRev.38.2082.2` (cit. on p. 49).

[116] Sooshin Kim et al. "Optical pumping effect in absorption imaging of $F = 1$ atomic gases". In: *Phys. Rev. A* 94 (2 2016), p. 023625. DOI: `10.1103/PhysRevA.94.023625` (cit. on pp. 52, 60).

[117]   Simone Serafini. "Dynamics of Vortices and their Interactions in Bose-Einstein Condensates". PhD thesis. Università di Trento, 2017 (cit. on p. 53).

[118]   Vasiliy Makhalov et al. "Precision measurement of a trapping potential for an ultracold gas". In: *Physics Letters A* 379.4 (2015), pp. 327 –332. DOI: http://dx.doi.org/10.1016/j.physleta.2014.10.049 (cit. on p. 57).

[119]   S. Friebel et al. "CO_2". In: *Phys. Rev. A* 57 (1 1998), R20–R23. DOI: 10.1103/PhysRevA.57.R20 (cit. on p. 57).

[120]   Franco Dalfovo et al. "Theory of Bose-Einstein condensation in trapped gases". In: *Rev. Mod. Phys.* 71 (3 1999), pp. 463–512. DOI: 10.1103/RevModPhys.71.463 (cit. on p. 59).

[121]   W. Gerlach and O. Stern. "Concerning the Quantization of Direction in a Magnetic Field". In: *Annalen der Physik, IV folge 74,* (1924) (cit. on p. 59).

[122]   Vincent Corre. "Magnetism in spin-1 Bose-Einstein condensates with antiferromagnetic interactions". Theses. Ecole normale supérieure - ENS PARIS, Dec. 2014 (cit. on p. 60).

[123]   V. Schweikhard et al. "Vortex-Lattice Dynamics in Rotating Spinor Bose-Einstein Condensates". In: *Phys. Rev. Lett.* 93 (21 2004), p. 210403. DOI: 10.1103/PhysRevLett.93.210403 (cit. on p. 63).

[124]   S. B. Papp, J. M. Pino, and C. E. Wieman. "Tunable Miscibility in a Dual-Species Bose-Einstein Condensate". In: *Phys. Rev. Lett.* 101 (4 2008), p. 040402. DOI: 10.1103/PhysRevLett.101.040402 (cit. on p. 63).

[125]   Satoshi Tojo et al. "Controlling phase separation of binary Bose-Einstein condensates via mixed-spin-channel Feshbach resonance". In: *Phys. Rev. A* 82 (3 2010), p. 033609. DOI: 10.1103/PhysRevA.82.033609 (cit. on p. 63).

[126]   D. M. Stamper-Kurn et al. "Collisionless and Hydrodynamic Excitations of a Bose-Einstein Condensate". In: *Phys. Rev. Lett.* 81 (3 1998), pp. 500–503. DOI: 10.1103/PhysRevLett.81.500 (cit. on p. 77).

[127]   T. van Zoest et.al. "Bose-Einstein Condensation in Microgravity". In: *Science* 328.5985 (2010), pp. 1540–1543 (cit. on p. 94).

[128]   André Kubelka-Lange et al. "A three-layer magnetic shielding for the MAIUS-1 mission on a sounding rocket". In: *Review of Scientific Instruments* 87.6 (2016), p. 063101. DOI: 10.1063/1.4952586 (cit. on pp. 94, 97, 99).

[129]   Anton Öttl et al. "Hybrid apparatus for Bose-Einstein condensation and cavity quantum electrodynamics: Single atom detection in quantum degenerate gases". In: *Review of Scientific Instruments* 77.6 (2006), p. 063118. DOI: 10.1063/1.2216907 (cit. on p. 94).

[130]   C. J. Dedman et al. "Active cancellation of stray magnetic fields in a Bose-Einstein condensation experiment". In: *Review of Scientific Instruments* 78.2 (2007), p. 024703. DOI: 10.1063/1.2472600 (cit. on p. 94).

[131] Wenxian Zhang et al. "Coherent zero-field magnetization resonance in a dipolar spin-1 Bose-Einstein condensate". In: *Phys. Rev. A* 92 (2 2015), p. 023615. DOI: 10.1103/PhysRevA.92.023615 (cit. on p. 94).

[132] O.L. Krivanek et al. "An electron microscope for the aberration-corrected era". In: *Ultramicroscopy* 108 (2008), pp. 179 –195. DOI: https://doi.org/10.1016/j.ultramic.2007.07.010 (cit. on p. 94).

[133] P. Mansfield and B. Chapman. "Multishield active magnetic screening of coil structures in NMR". In: *Journal of Magnetic Resonance (1969)* 72.2 (1987), pp. 211 –223. DOI: https://doi.org/10.1016/0022-2364(87)90283-6 (cit. on p. 94).

[134] Araneo R. Celozzi S. and Lovat G. *Electromagnetic shielding*. Wiley-Interscience, 2008 (cit. on p. 95).

[135] Xingcun Colin Tong. *Advanced Materials and Design for Electromagnetic Interference Shielding*. CRC Press, 2009 (cit. on p. 95).

[136] J. M. Pendlebury T. J. Sumner and K. F. Smith. "Convectional magnetic shielding". In: *J.Phys.D:Appl.Phys.* 20 (1095 1987) (cit. on p. 97).

[137] "Magnetic shielding". In: (). Accessed: 2017-12-15 (cit. on p. 97).

[138] F. Thiel et al. "Demagnetization of magnetically shielded rooms". In: *Review of Scientific Instruments* 78.3 (2007), p. 035106. DOI: 10.1063/1.2713433 (cit. on p. 100).

[139] Silvestrini V. Mencuccini C. *Fisica II Elletromagnetismo-Ottica*. SLiguori Editore, 1998 (cit. on p. 100).

[140] E. A. Burt and C. R. Ekstrom. "Optimal three-layer cylindrical magnetic shield sets for scientific applications". In: *Review of Scientific Instruments* 73.7 (2002), pp. 2699–2704. DOI: 10.1063/1.1487892 (cit. on pp. 107, 110).